Probing defect and magnetic structures on the nanoscale

Kallis, Alexis

Award date:
2010

Awarding institution:
University of Bath

Probing Defect and Magnetic Structures on the Nanoscale

Alexis Kallis

A thesis submitted for the degree of Doctor of Philosophy

University of Bath

Department of Physics

September 2010

To my father

ACKNOWLEDGEMENTS

I would like to thank a number of people that have helped in the completion of this thesis.

Firstly I would like to express my gratitude to my supervisor, Professor Paul G. Coleman for his flawless guidance throughout my PhD. He has proven to be a beacon of inspiration and encouragement, without which, the completion of this project would undoubtedly not have been possible. His genuine concerns for all his colleagues and students' wellbeing, as well as his cheerful character are appreciated by everyone in the Positron Group. It has truly been an honour to have worked with him.

I would also like to take the chance show my appreciation to the staff at the University of Bath that have contributed to my PhD. I am grateful to the administration office staff, Eva Ashford, Alison Humphries and Santina Kennedy for their informative advice on the departmental rules and regulations. Many thanks for the technical support from Adrian Hooper, for his prompt and decisive response to any IT related problems and Harry Bone for his lively technical solutions in the positron lab. I am also grateful to Charlene Edwardson and Lowenna Smith for their moral support and friendship. This project would have not been possible without the funding from ESPRC that has covered my fees and my living expenses during my three years at the University of Bath.

Last but not least, I would like to thank my family for their support and encouragement as well as for their financial contribution to my PhD, and specifically my father, for inspiring me to aspire for the highest of educational achievements.

ABSTRACT

This thesis reports on experimental research on structural defects and magnetic species on the nanoscale. The latter project involved considerable development work on the production of a spin-polarised mono-energetic positron beam. The construction of the system is described through various trial steps with emphasis on the methods of maximum practical polarization of the positron beam and of electrons in the sample with the smallest possible loss of beam intensity. A new sodium-22 source capsule was purchased, having beryllium foil backing to minimise the depolarisation effects of backscattering, and the source-moderator spacing was increased. Different types of sample were tested, varying in atomic structure, purity, magnetic susceptibility, electronic structure, and electric conductivity - including iron of different purity and structure, mu metal and solid oxygen. After these tests measurements were taken on single crystal iron, and the results suggest that the positron response to magnetic structures is very small, and that prospects for depth profiling of dilute magnetic systems are not favourable at this time.

A large number of other investigations have been performed on non-magnetic defect structures in various materials. Variable Energy Positron Annihilation Spectroscopy – here involving beam-based Doppler broadening – was applied to novel materials of relevance to photonic or electronic structures on the nanoscale. These included thin films of technological interest such as AlGaN and Ar plasma-treated TiO_2: silicon and silicon-on-insulator samples implanted with He and Si ions to engineer vacancies: Si-rich SiO_2 and SiN to form nanocrystals for photonic applications in which new findings on the evolution of the nanocrystals, and the role of the nanocrystal-oxide interface in optical emission, could be very useful in the technological development of such systems: and a study of the structural phase and nano-pore properties of water ice films grown from vapour on a cold copper surface.

The variety of these experimental studies serves to underline the wide applicability of positron beam spectroscopy in research on defect and nanostructure structures. A list of papers published to date resulting from this work is given at the end of the thesis; a number of others are planned.

CHAPTER 1: INTRODUCTION

Indications of an unknown particle were first found experimentally in cosmic rays chamber photographs [1]. The particle was identified as the positron, and was the first antiparticle to be observed. Positron – electron annihilations were first studied in 1940 and it was realised that conservation laws allowed exploitation of this phenomenon for studying properties of solids. Early experimentation was focused on studying the electronic structure of metals and alloys [2]. After 1945 numerous experimental techniques were developed, based on the angular correlation of annihilation γ -quanta, Doppler broadening of the annihilation line, and positron lifetime spectroscopy. By 1970 it was realised that lattice imperfections were affecting annihilation parameters and that positrons may be trapped in crystal defects. Quantum mechanically, the positron wave function is localised at the defect site which acts like a quantum well [3]. The reason for this is the creation of attractive potential at vacancies (open volume point defects) which due to the lack of a positively charged nucleus that would normally repel the positron. A positron may diffuse through the lattice of a metal for about 100nm (or 250mm in Si) allowing a huge sensitivity to defects (one per 10^7 atoms). Vacancies affect the annihilation parameters characteristically. The lower electron density results in a longer annihilation lifetime and (generally) the lower mean electron momenta leads to a smaller Doppler shift of the annihilation gamma ray energy or a smaller angle between the almost collinear γ-quanta. Electron density and momentum distributions are thus both detectable in positron experiments [4].

The slow positron beam technique is a unique tool used for studying vacancy defects in semiconductors, metals and alloys, as well as free volume in insulators. It uses mono-energetic positrons, usually at energies up to the order of a few tens of keV. This controlled positron energy allows, with resolution of the same size as mean depth, the estimation of the depth in a specific material at which positrons are most likely to annihilate, leading to a semiquantitative capability for depth profiling of vacancy-type defects, as well as their characterisation. More details are given below.

1.1 Positrons

A positron is the antimatter or antiparticle counterpart of an electron and it was predicted by Dirac in 1930 ("On the quantum theory of an electron", most commonly cited as "On the annihilation of electrons and protons") [5]. It has a spin of ½, an electric charge of +e, and exactly the same mass as an electron. Positrons are not easily found in an everyday environment, existing only in cosmic rays. They are usually generated by pair production from a sufficiently energetic photon, or in radioactive decays (positive beta decays). In our case the latter method is used.

When a positron closely approaches an electron, they attract each other due to their opposite charges and collide, both of them being destroyed. This annihilation releases energy in the form of gamma ray photons, and a number of conservation laws must be satisfied:

i) Conservation of charge
ii) Conservation of total energy and linear momentum
iii) Conservation of angular momentum.
iv) Conservation of parity

In the case of annihilation of low energy positrons in matter, it is most likely that two gamma ray photons will be created. The ii) and iii) conservation laws stated above forbid the creation of a single photon. The two photons have total energy equal to the rest energy of the positron or electron, 1022keV (the particles' kinetic energy and the electron's binding energy are usually neglected). For convenience, in a frame of reference in which the system has no linear momentum before annihilation, the gamma rays are emitted in exactly opposite directions. It is also possible for three or more gamma rays to be created but the probability of this becomes lower with each additional photon.

The bound electron- positron pair is known as positronium and was predicted by Mohorovicic in 1934 [6] and discovered by Deutsch in 1951 [7]. It is considered an "exotic atom"; it has a mean natural (vacuum) lifetime of 125ps and 142ns in its para (singlet) and ortho (triplet) states and it has energy levels essentially half those of a hydrogen atom because the reduced mass of the electron is ~ m_e in hydrogen and ~m_e/2 in positronium. Positronium formation and decay are used as a probe of pore structures in insulators - as will described in Chapter 3 (page 68).

When energetic positrons are implanted into a condensed medium, they rapidly lose their energy. At highest positron energies, the main mechanism of energy

losses is ionisation, i.e., the positron ejects core electrons in collisions with the host atoms. At lower energies electron-hole excitations take over. When the positron energy has degraded to a fraction of eV, scattering off phonons dominates. Eventually, positrons reach thermal equilibrium with the medium, maintained due to phonon emission and absorption. During thermalisation, the initial kinetic energy of positrons drops below 0.1 eV, i.e., by several orders of magnitude. Despite such a colossal change in energy, positron thermalisation times are typically as short as a few picoseconds [8] i.e., much shorter compared to the above estimated positron lifetimes. Diffusing thermalized positrons then undergo various interactions which influence the state from which they are eventually annihilated by an environmental electron.

1.2 Positron Spectroscopy Techniques

Positron Annihilation Lifetime Spectroscopy

The principle of standard laboratory-based Positron Annihilation Lifetime Spectroscopy (PALS) measurements relies on positron emission radioactive decay as a source of positrons. In the case of Na-22 these decays will also emit a γ-ray of 1274 keV, so that a positron is implanted into the sample almost simultaneously with this γ-ray. Lifetimes of individual positrons, t, can be measured as time differences between emission of the 1274 keV γ-ray and the annihilation γ-ray (having ~511 keV in the case of a 2 γ annihilation). Thus the spectrum of positron lifetimes is obtained as the histogram of the number of decays as a function of t, $N(t)$. A positron inside a medium has an associated mean lifetime. This lifetime is strongly dependent on where the positrons end up, whether it is a region heavily populated by electrons or a region where electrons are scarce. This can be used to gain insight on the structural nature of the material. In case of lattice structures there are lower electron densities in open-volume point defects, and in case of amorphous structures in the free volume, e.g. between the chains of a polymer.

Angular Correlation

This technique is based on measuring the small variations in direction between the gamma rays emitted by a two gamma annihilation process. In theory, photons from an electron and positron at rest should be 180º, but due to the momentum electrons have at the time of annihilation, there are small variations in this. The two

annihilation photons are emitted simultaneously. Thus a function of the transverse electron momentum component can be measured in coincidence arrangement with position-sensitive detectors. A simple position sensitive detection can be realised in one dimension by mechanical movement of a long scintillation detector with lead slits [9]. The momentum distribution can also be recorded in two dimensions using a two dimensional detector arrays [10]. The sample-to-detector distance amounts typically to several metres so that quanta from only a small solid angle are detected. Hence much stronger positron sources compared with conventional lifetime and Doppler shift techniques are required. On the other hand, angular resolution ranges from 0.2 to 5 mrad [10]. This corresponds to the energy resolution of Doppler shift measurement in the range of 0.05 to 1.3 keV. Thus the angular correlation technique provides essentially the same kind of information as the Doppler shift, but the momentum resolution of the method is much better.

Doppler Broadening Spectroscopy

This technique measures the energy of the annihilation gamma rays. It utilises a standard spectrometer (usually using a pure Ge crystal) and provides a spectrum of photons with a peak at 511keV. The spread of energies is linked with the energy of the electrons annihilated (via Doppler broadening). It too, just as angular correlation, can provide information about the directional momentum of the electrons at the moment of annihilation. This method is useful when looking at vacancies and the atomic structure of materials. It has a higher count rate but lower resolution than angular correlation, and is typically used to make faster measurements of changes in defect structure with temperature or other external influences.

As stated before, momentum conservation laws state that the momentum of the positron-electron pair, p, is transferred to the photon pair. Due to the rapid (~ ps) thermalisation taking place for positrons, the positron momentum is negligible during the annihilation (and as only one positron is present in the solid at any given time, the Pauli theorem does not apply). Therefore the momentum of the electron dominates. The z component of the electron momentum (z being the direction towards the gamma detector) will then result in a Doppler shift of the gamma ray pair which approximates to:

$$\Delta E = p_z c/2 \qquad (1)$$

Since p_z can take any value in up to the maximum momentum of the electron towards or away from the detector, this results in the broadening of the spectrum peak of the 511keV gamma ray spectrum. This broadened peak is symmetrical on both sides of the 511keV value due to the symmetrical spread of momentum direction of the electrons, but the exact profiling of individual shell electrons is difficult as this is a relatively low resolution technique. However, some attempts for modelling this are made within the project and will be mentioned in detail later.

A sketch of a typical spectrum of the gamma rays is shown below. The Doppler shift broadening is ~1kev, similar to the energy resolution of the Ge detectors typically used for the measurement.

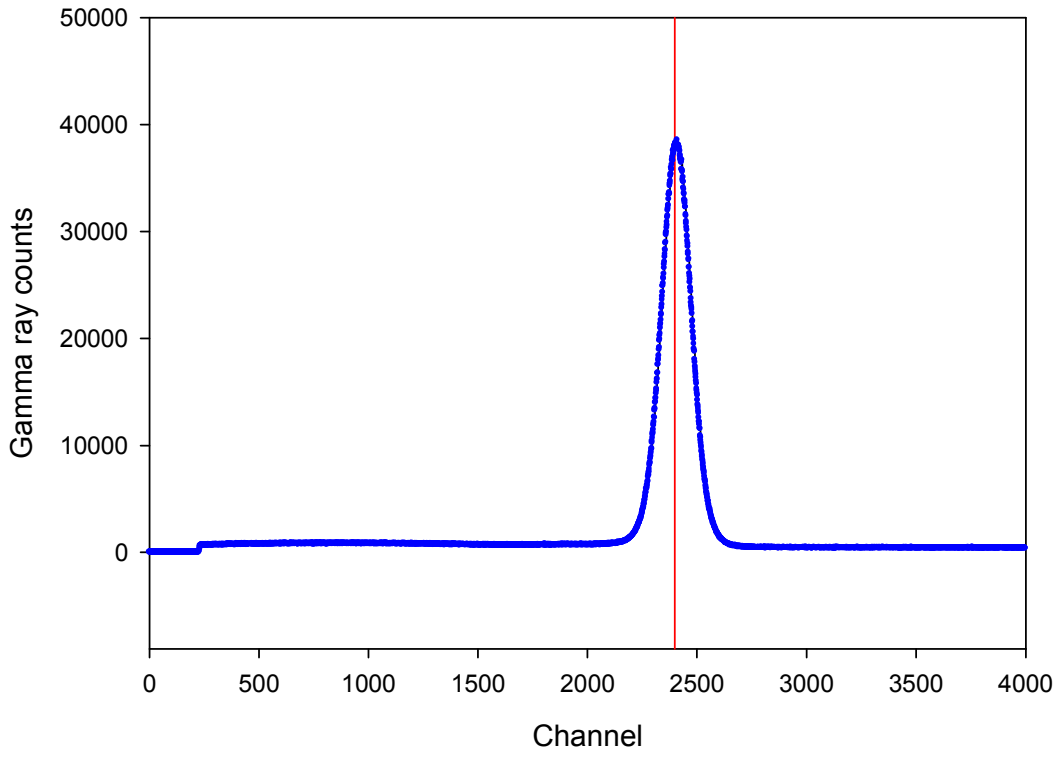

Figure 1: Sketch of a γ – ray spectrum around 511keV (shown in red at channel 2399). The width is typically ~ 2.5keV at half maximum. There are 18.8eV per channel and channel 2399 corresponds to the 511keV peak.

This spectrum arises from all the gamma rays produced from annihilations with all the differently energetic electrons which transfer all their energy to the Ge detector crystal in photoelectron interactions. For electrons with lower average momentum the curve would be narrower since the possible Doppler shifts would be smaller.

Since positrons are extremely sensitive to vacancies, we can expect to see their effect on this spectrum. We can assume that the electrons situated in (or around) a vacancy have a specific range of momentum values. By introducing more and more vacancies, if this momentum value is greater than the average value of all the electrons annihilating in the solid, we would expect a broadening of the peak, if it is less than the average we would expect a narrowing. By then keeping the total gamma ray count rate constant, the narrowing or broadening of the curve would also increase or decrease the peak value respectively. Thus, a semi-quantitative measurement of vacancies in solids is possible.

Parameters to represent the shape of the curve have been created. The *S* parameter represents the percentage of gamma rays counted in the middle section of the peak. The boundaries of this middle section are arbitrary and are defined differently around the world, but it is most common to define them such that for bulk crystalline silicon with no defects, the *S* parameter is 0.5. The boundaries remain constant as the photo peak changes for different materials, giving a different S parameter value every time. The *W* parameter is similar, but represents the percentage of counts in the wings of the curve. Again the boundaries of this are arbitrary, and most commonly set such as for bulk crystalline silicon with no defects, they add up to 0.15 (0.075 on each side).

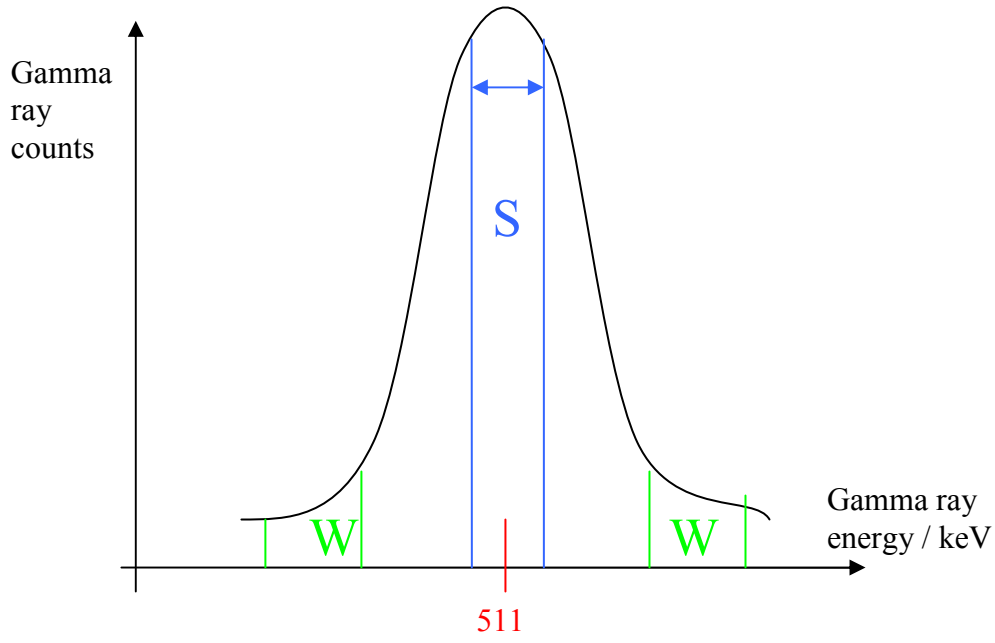

Figure 2: A graphical representation of the *S* and *W* parameters on the γ-ray spectrum.

It is also common to normalise these parameters to their respective bulk values, reducing the problem caused by the choice of different parameter limits in different laboratories.

The *S* parameter is sensitive to lower-momentum electrons (e.g., valence and conduction electrons) and is less susceptible to background and noise due to the large number of counts within its boundaries. The *W* parameter on the other hand is more sensitive to core electrons (higher energy electrons – broader Doppler shifts).

Age- Momentum Correlation

The Age-Momentum Correlation, or AMOC, technique combines lifetime measurements and Doppler broadening measurements using the same annihilation event [11]. One of the two annihilation photons provides the stop signal for the positron lifetime while the second photon is used for the measurements of the Doppler broadening of the annihilation line. The triple coincidences of both the annihilation photons with the decay photon at the source are registered. The spectra are stored with the positron age and Doppler shifts being represented along the co-ordinate axes, giving an electron momentum correlation with the lifetime or age of the positron. Thus dependence of the electron momentum distributions on the positron lifetime can be measured. For example, Doppler curves for ortho-positronium (o-Ps) events with very long lifetimes can be separated out of the annihilation events related to para-positronium (pPs) or positrons that did not form Ps.

1.3 Slow Positron Beams

Conventional positron techniques use a sample-source "sandwich" arrangement where the emitted positrons penetrate into the bulk of the sample, reaching thermal equilibrium in ~ps. This arrangement is possible in air but the sample is usually mounted in an evacuated chamber. The broad spectrum of high positron energies (of up to 540keV for ^{22}Na) gives a high maximum penetration depth. However, these conventional techniques are limited when it comes to applications in modern thin film physics. To achieve a small penetration depth, slow (mono-energetic) positron techniques known as variable energy positron annihilation spectroscopy (VEPAS), are used. It is relatively straightforward to semi-quantittively

depth profile defects in a material simply by adjusting the positron energy (few eV – tens of keV). The ways of creating this mono-energetic beam will be shown later.

Slow Positron Beam – Apparatus setup

Modification of small but crucial parts of the standard positron beam apparatus were required to perform the specific experiments described in this thesis. The general setup is shown in the figure below with all major components identified [21] shown in figure 3.

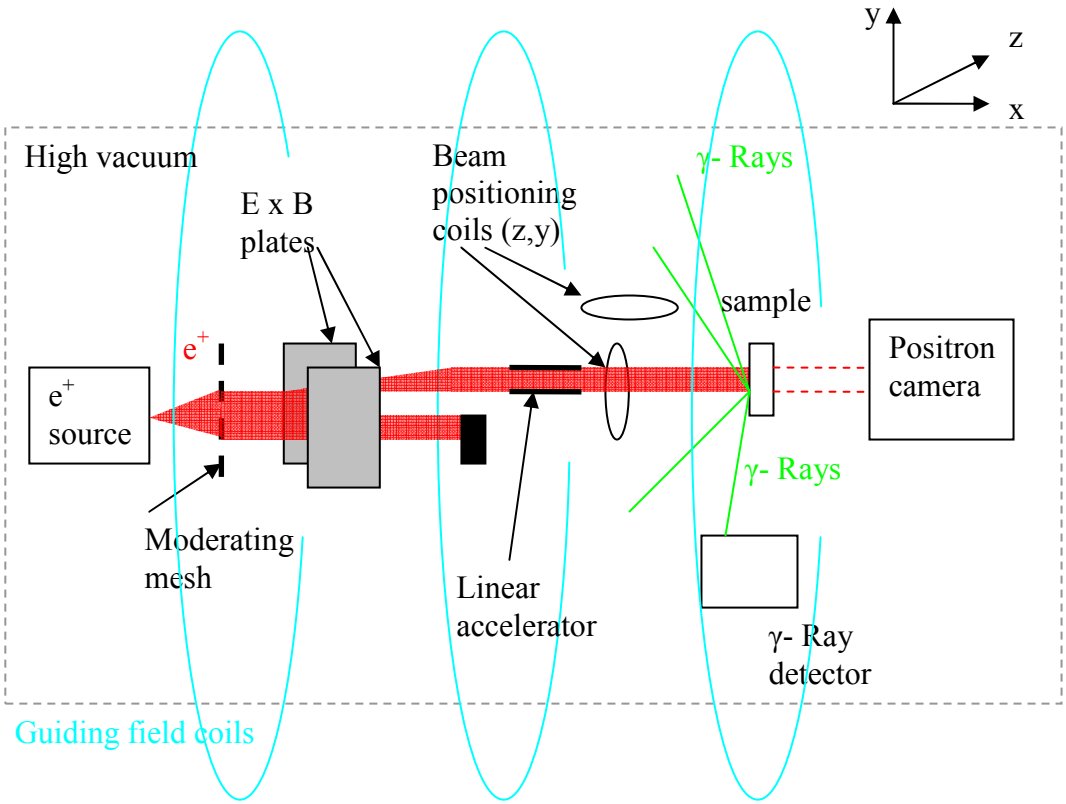

Figure 3: A simple representation of a slow positron beam configuration

High vacuum: A high vacuum of about 10^{-5} Pa (10^{-7} mBar) is required in order to have negligible scattering medium between the positron source and the sample, so that (a) all slow positrons reach the target, and (b) no unwanted (ie non-target) annihilation events can be detected. To achieve this high vacuum a turbo molecular pump and an ion pump – backed by rotary pumps - are used.

Positron source: This is an enclosed ^{22}Na with the backside of the casing being tantalum, which has a high back-scattering coefficient. This increases the number of positrons that are emitted in the forward direction (Figure 3) towards the sample. The ^{22}Na has a high positron yield of 90.4%, it is relatively easy to

manufacture (thus affordable) and, along with its high lifetime (2.6 years), makes it a good value-for-money source. Furthermore its biological lifetime is small (a few days) making any accidental personnel contamination less harmful. Its decay equation is as follows: $^{22}Na \rightarrow {}^{22}Ne + \gamma + e^{+} + \nu_e$.

Moderating mesh: The moderating mesh is a 50% transmission annealed tungsten mesh and it is at a lower potential than the source (typically 9V). Its purpose is to stop positrons, thermalize them, and then re-eject them with a low energy equal to the positron work function of the material [12] (~3eV for tungsten) as shown in figure 4. On the other side of the mesh, there emerges a mixture of positrons that went right through it having high energy, and moderated ('work-function') positrons. There is approximately one moderated positron per 2500 unmoderated ones. [13]

E x B plates: These plates serve as an energy filter for the positrons. They have a potential difference across them such as that the slow mono-energetic positrons are deflected enough (by about 30mm) to go through a slit and the fast un-moderated positrons are deflected only by a fraction of 1mm and are annihilated. The annihilation area of the fast positrons is surrounded by lead to ensure minimal detection by the gamma ray detector.

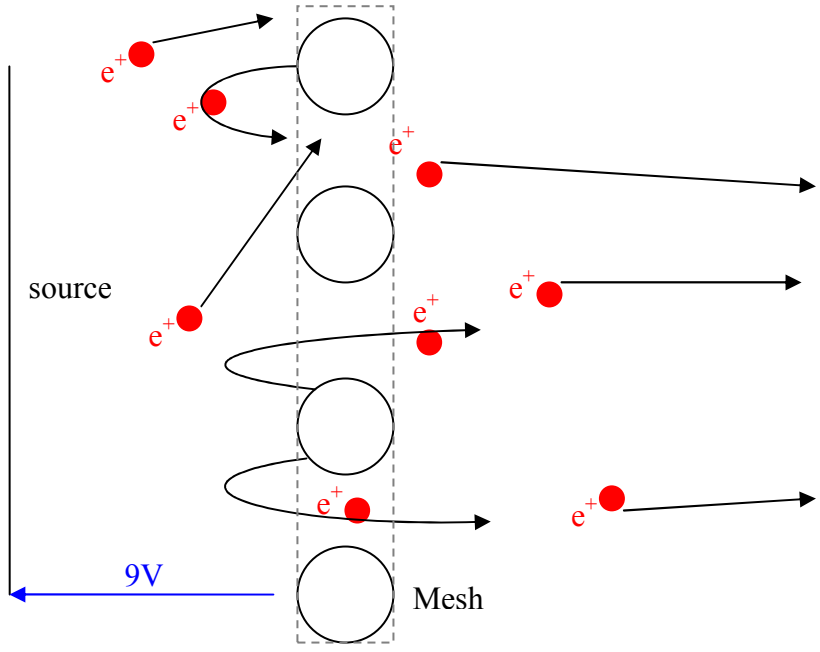

Figure 4: A representation of the moderating of positrons by an annealed tungsten mesh.

Linear accelerator: This is simply a step to accelerate the slow positrons to a desirable energy (in our case, 0 to 30keV). This is easily controlled by software from a pc. The entire first half of the apparatus (source, moderator and ExB plates) is raised to the accelerating voltage while the second half remains at ground potential.

Beam positioning coils (z,y): These coils are the last step the beam goes through before reaching the sample. They simply deflect the beam towards the sample in case of an offset between the beam centre and the sample position. They are also controlled by software from a pc.

Sample and Sample holder: The sample is mounted on a sample holder made of a stainless steel frame with a couple of very fine (0.1mm) tungsten wires running across it. The frame is at the end of a long stainless steel rod which is lowered inside the sample chamber through a long narrow opening. Once inside the chamber, sealed and evacuated, it is possible to move the holder in all 3 dimensions although the *x* and *z* directions (Figure 5) are quite limited. During this project, the sample holder was redesigned and altered to suit each individual measurement.

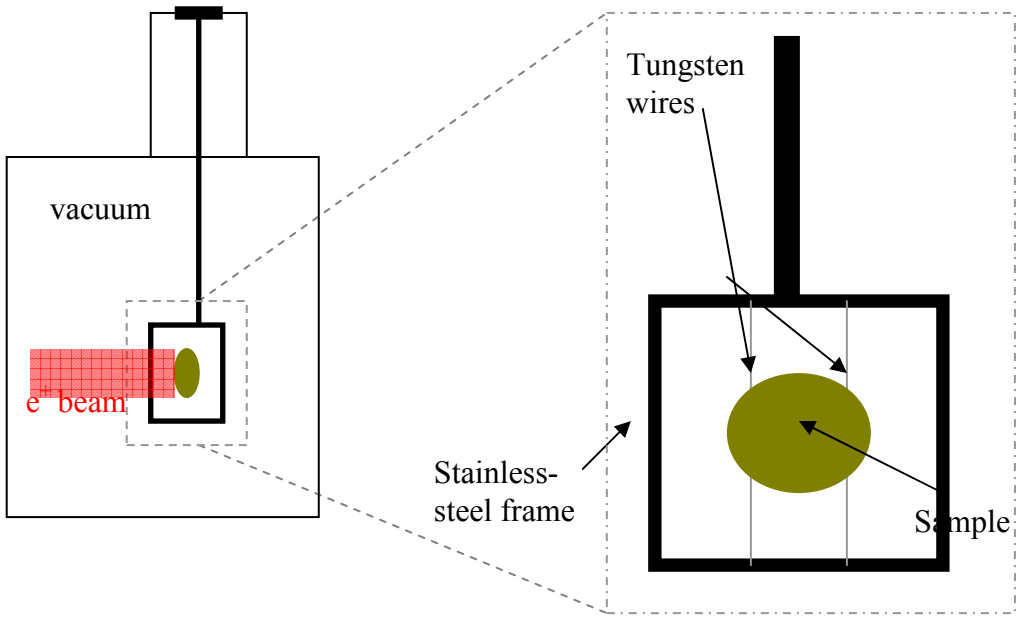

Figure 5: The sample chamber, sample holder and sample configuration during a typical VEPAS measurement.

γ- ray detector: At a close proximity to the sample but outside the vacuum chamber there is a γ- ray detector. This is a Ge crystal cooled by liquid N_2. It is mounted on a platform resting on insulating rubber balls to ensure minimal vibration transfer to it. The detector registers γ- rays from the positron annihilations inside the sample and records them via software on a pc. This can be done in real time.

Positron camera: The camera setup consists of two electron multiplier plates, a phosphor screen and an ordinary real time CCD camera. This allows a single positron that reaches the setup to be translated into many ($\sim 10^7$) electrons and then into photons by the phosphor which are easily seen by the camera. The camera is directly connected to a pc. There is also a coil between the sample and the positron camera setup giving control over focusing the positrons image on the phosphorous screen. The electron multiplier plates are highly sensitive to humidity, very fragile and expensive. They usually last a few years before requiring replacement.

Guiding field coils: Any charged particle moving at an angle to magnetic field lines experiences a force. This force is due to the lateral parts of the motion (*z, y*) – in case of only an *x* component, the particle would move in a straight line. By using the right hand rule, we can see that the particle will move in a spiralling motion along the field lines. The radius of the spiral depends on the magnetic field strength (*B*) and the transverse velocity (v_{zy}) of the particle.

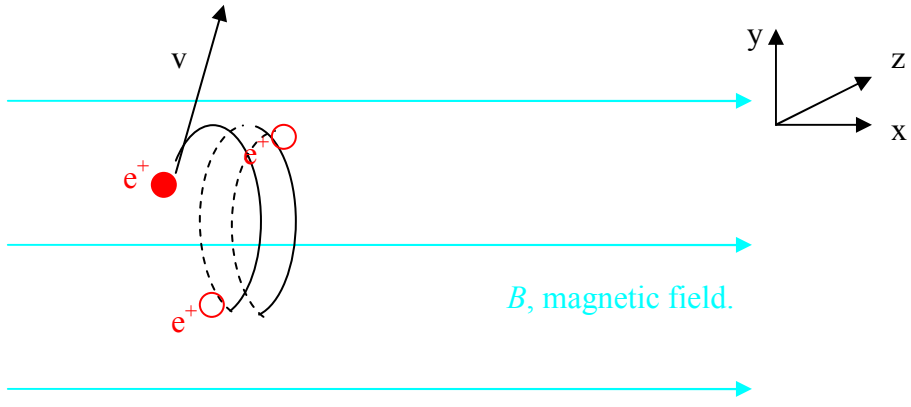

Figure 6: A positron moving in a spiral motion along a magnetic field *B*.

This spiralling motion results in the controlled guiding of the particles towards the desired target. The radius of the spiral is of a few mm depending on the lateral

speed components and the magnitude of the field. This magnetic field (guiding field) is easily maintained by a number of aligned coils outside the vacuum chamber.

Approximately 10^8 beta positrons per second are emitted by the Na-22 source with energies up to 540 keV. These positrons then enter the annealed tungsten moderating mesh, mounted 1mm in front of the source, where they thermalise within ~ 1ps. They then have a probability to be re-emitted, depending on their distance from the surface of the mesh compared to the positron diffusion length in well-annealed tungsten of ~ 100nm. Approximately 0.05% of all the beta positrons are re-emitted with the tungsten work function of 2.7 eV. A 9V potential between the source and moderator ensures that positrons re-emitted towards the source are turned around and proceed through the moderator mesh into the system. ***E x B*** plates then deflect the moderated positrons by 6cm into a region where they are accelerated towards the sample at a predetermined energy from 0.1 to 30 keV. Un-moderated positrons are deflected insignificantly by the ***E x B*** plates, do not enter the accelerator, and are therefore lost.

Positrons that enter the sample thermalise with an implantation profile described by the Makhov distribution $P(z)$ [23]:

$$P(z)= (m/z_0)\,(z/z_0)^{m-1} \exp\,[-(z/z_0)^m] \quad \text{nm}$$

where $z_0= 1.13\,(\alpha_p/\rho)E^n$; α_p and n are material-dependent parameters, ρ is the material density and E is the positron energy in keV [18]. The Makhov parameter m is usually found to be ~2 – i.e., the distribution is a Gaussian derivative. The mean implantation depth is approximated by:

$$\bar{z} = (40/\rho)\,E^{1.6}$$

Positrons then diffuse in the sample with a diffusion length characteristic of the nature of the sample, before annihilating with an electron. If the positron encounters a vacancy-type defect while diffusing it will be localised and trapped there. Positrons are highly sensitive to such defects, over a range from 10^{-7} to 10^{-4} per atom (the latter value representing saturation trapping). The specific trapping rate is very small for positively-charged defects, but positrons are trapped efficiently by neutral vacancies and the rate is increased significantly if the trap is negatively charged, as can be the case in semiconductors. Vacancy-type positron traps are deep (~few eV) and thermal de-trapping is very unlikely.

Slow Positron Beam –Doppler Broadening measurements

When Doppler broadening measurements are made using a mono-energetic positron beam they can be linked to a specific mean depth in the solid. The energy of the beam corresponds to different mean depths in different materials due to the different atomic density of the material (see below). Depth resolution is also affected by the different diffusion length of positrons before they annihilate (i.e. how far they travel on average before they meet an electron). An *S*-parameter against energy representation is quite common and for crystalline silicon it would look like Figure 6 below.

The surface *S* value is here lower because of annihilations with oxygen electrons in the native oxide layer on the surface following diffusion of thermalized positrons to it. The "zero energy" *S* value is affected by epithermal positron effects taking place [14]. Positron – electron pairs (positronium) may escape the material and annihilate in the vacuum above. *W*-parameter against positron beam energy plots are useful and even *S*-parameter against *W*-parameter, as will be demonstrated later.

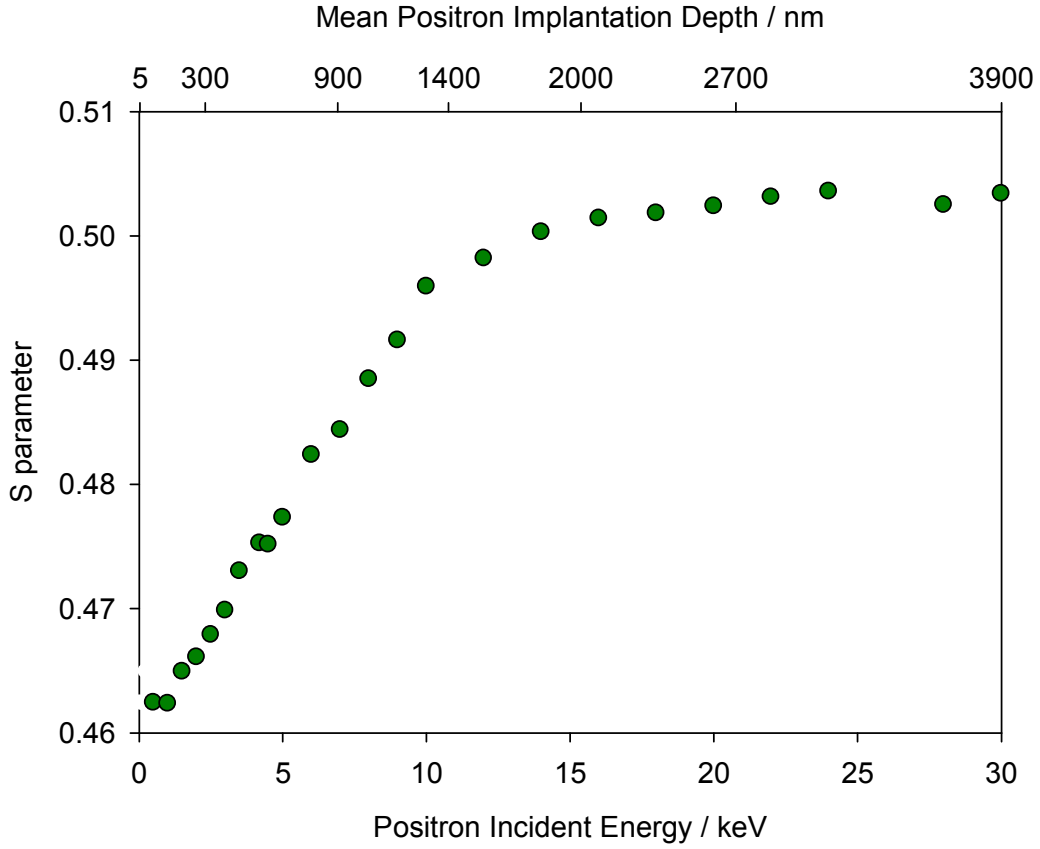

Figure 7: A typical *S* parameter result for a Cz Si sample showing both the positron incident energy and mean positron implantation depth axes.

1.4 VEPFIT

Measured data from the positron beam are very complicated to fit in terms of depth dependent material parameters. It is generally difficult to indicate what contribution the positrons give to *S* parameter and diffusion values when implanted at a certain depth because of the multiple processes involved. The biggest part of fitting is the retrieval of the position of positrons during annihilation.

VEPFIT is software that was created to provide a computational fitting method for extracting depth dependent information from the data like in figure 7. It is based on an iterative calculation method for solving the equation of the time-averaged positron density in any material, and is also able to account for internal fields [15].

Model and Calculation Method

Thermalized implanted positron transport can be approximated by diffusion theory. It refers to the situation where particles (in this case positrons) travel through a material to depths much greater than their mean free path, having their behaviour dominated by scattering, effectively having a random path. The mean distance travelled prior to annihilation is the diffusion length, L. The positron transport problem for mono-energetic positrons slowing down in a defect free solid has been solved before [16,17] and it was found that the implantation profiles could be described fairly well by the Makhov [23] distribution $P(z)$:

$$P(z) = (m/z_0)\,(z/z_0)^{m-1} \exp\left[-(z/z_0)^m\right]$$

where $z_0 = 1.13 \times \alpha_p/\rho E^n$, α_p, m and n are material-dependent parameters, ρ is the material density and E is the positron energy [18].

The above approximation fails when the material is non-uniform or it has defects. The arising problems have been addressed [19], and a final complex model has been formed and incorporated into VEPFIT. As long as one understands the capabilities and limitations of VEPFIT it can prove to be an invaluable tool in the understanding of data collected by VEPAS.

CHAPTER 1 REFERENCES

[1] C. D. Anderson, "The positive electron", Phys Rev **43**, 491 (1933).

[2] R. Behringer and C. G. Montgomery, Phys. Rev. **61**, 222 (1942).

[3] M.J. Puska, C. Corbel and R.M. Nieminen, "Positron Trapping in Semiconductors", Phys. Rev. B **41**, 9980 (1990).

[4] A. E. Hamielec; M. Eldrup; O. Mogensen, "Positron Annihilation Techniques (PAT) in Polymer Science and Engineering", Polymer Reviews **9**, 305 (1973).

[5] P. A. M. Dirac, "The Quantum Theory of the Electron", Proc. Cambridge Philos. Soc. **26**, 361 (1930).

[6] Mohorovičić, S. (1934). "Möglichkeit neuer Elemente und ihre Bedeutung für die Astrophysik". Astronomische Nachrichten **253**, 94 (1934).

[7] M. Deutsch, **"**Evidence for the Formation of Positronium in Gases", Phys. Rev. **82**, 455 (1951).

[8] W. Brandt and A. Dupasquier (editors), *"Positrons Solid-State Physics"*, Proc. Internat. School of Physics «Enrico Fermi», Course LXXXIII, Varenna 1981, North-Holland, Amsterdam (1983).

[9] A.T. Stewart, "Momentum distribution of metallic electrons by positron annihilation", Can. J. Phys. **35**, 168 (1957).

[10] R N West, J Mayers and P A Walters, "A high-efficiency two-dimensional angular correlation spectrometer for positron studies", Journal of Physics E: Scientific Instruments **14**, 478, (1981)

[11] H. Stoll, in "Positron Beams and their applications", ed. P.G. Coleman (World Scientific, 2000), p 243.

[12] C. Hugenschmidt B. Straßer and K. Schreckenbach, "Investigation of positron work function and moderation efficiency of Ni, Ta, Pt and W(1 0 0)", Applied Surface Science, **194**, 283 (2002).

[13] H. M. Weng, C. C. Ling, C. D. Beling, S. Fung, C. K. Cheung, P. Y. Kwan and I. P. Hui' "Tungsten mesh as positron transmission moderator in a monoenergetic positron beam", Nucl. Instrum. Methods B **225**, 397 (2004).

[14] D. T. Britton, P. C. Rice-Evans, J. H. Evans, "Epithermal effects in positron depth profiling measurements" , Phil. Mag. Lett. **57**, 165 (1988).

[15] A. van Veen, H. Schut, J.de Vries, R. A. Hakvort, M.R. Jipma, "Analysis of positron profiling data by means of VEPFIT", AIP Conf. Proc. **218** (New York: AIP) 171 (1990).
[16] SJ Pearton *et al*., J. Phys: Condens. Matter, **218**, 171 (2004).
[17] G Reiss and A Hütten, "Magnetic nanoparticles: Applications beyond data storage", Nature Materials **4**, 725 (2005).
[18] A. Vehanen, K. Saarinen, P. Hautojarvi and H. Huomo, "Profiling multilayer structures with monoenergetic positrons", Phys. Rev B**3**5, 4606 (1987).
[19] P.J. Schultz and K.G. Lynn, "Interaction of positron beams with surfaces, thin films, and interfaces", Rev Mod Phys. **60**, 701 (1988)
[20] P.G. Coleman, Editor, "Positron Beams and their applications", World Scientific (2000).
[21] P.G. Coleman, "Back to the future: Polarised positron beams", Applied Surface Science **225**, 101 (2008).
[22] A.F. Makhov, "The penetration of electrons into solids II. The distribution of electrons in depth", Proc. Roy. Soc. **445,** 57 (1960).

CHAPTER 2: DEVELOPMENT OF A SPIN-POLARISED POSITRON BEAM FOR PROBING MAGNETIC STRUCTURES ON THE NANOSCALE

2.1 Introduction to Spin-Polarised Positron Beams

Materials with magnetic properties are making an entrance to the world of electronics. The field studying this is called "Spin transport electronics", "Spintronics" or "Magnoelectronics"[1], involving the exploitation of the intrinsic spin of electrons or their associated magnetic moment for the operation of electronic devices rather than the electric charge of electrons currently used for information transfer. There is currently no non-invasive way of probing magnetic clusters (spin polarised clusters) or areas in the bulk of materials.

Only a few experiments have managed to demonstrate that slow positron beams retained a high axial polarisation [2]. It has also been shown that positrons could be sensitive to spin polarised electrons [3]. Since then, any applications of this have been overlooked. VEPAS can be sensitised to spin polarised electrons allowing their study and identification to a few micrometers depth. A spin polarised positron would preferentially kill or avoid killing a spin polarised electron depending on the direction of its polarisation. This preferential annihilation of electrons is dominated by the law of conservation of parity, thus forbidding a 2γ positron – electron interaction (annihilation) when their spins are the same. In practice it is seen that the statistical preference of annihilation is of three orders of magnitude larger for opposing spins compared to parallel spins [4]. Also, a positron electron pair has a mean lifetime of 125ps in its singlet state (opposing spins) and 145ns in its triplet state (same spins) [5]. The measurements taken utilize Doppler broadening of the annihilation gamma rays which is directly linked to the momentum of the participating electrons. Therefore if the spin states of electrons in a sample are changed, the statistical preference for their annihilation by positrons will alter, thus changing the overall Doppler broadening data (i.e. gamma ray energy spectrum). The diffusivity of positrons in the sample would enhance the sensitivity of the system for probing electron spin polarized clusters since the positrons get trapped in the damaged matrix surrounding such a cluster. This would put the technique in the lead when compared

to existing ones (i.e. high resolution X-ray diffraction, Optical measurements, SQUID measurements). [6]

Every electron in a solid acts as a small magnet. In most materials, the huge numbers of electrons have spins orientated in random directions resulting in no net magnetic field. Some materials with magnetic properties can align the spin of some of their electrons resulting in a net magnetic field of some sort. The overall magnetic behaviour can vary depending mainly on the electron configuration or even on the structure of the material.

The easiest way of spin polarising a sample is by applying an external magnetic field. In order to have a better understanding of this, the basics of magnetisation are briefly summarised below.

Magnetisation

The magnetisation (M) of a material [7] can be expressed in terms of the magnetic dipole moment density (μ): $M = \mu / V$ .The total magnetic field inside the material B, also known as magnetic flux density, is given by $B = B_0 + \mu_0 M$, where B_0 is the externally applied magnetic field and μ_0 is the magnetic permeability of space. Another term used is *relative permeability* which is the ratio of the material's permeability to that of space. Magnetic susceptibility χ_m defines the difference of relative permeability from one: $\chi_m = \mu / \mu_0 - 1$. A material with no magnetic properties which does not respond to external magnetic fields has a relative permeability equal to one. Diamagnetic and paramagnetic materials have a relative permeability close to one where ferromagnetic materials can have a very large χ_m.

When a field B passes through a magnetic material it is not clear what part of it is from the external field and what part of the total magnetic field is generated by the material. For this reason another quantity called magnetic field strength H is defined by $H = B / \mu$, which is designated as the external magnetic influence on a material independent of its response.

The most important types of magnetic materials are:

Diamagnetic: a net magnetic field opposes the external field which persists only while external field is applied. It is due to the non-cooperative behaviour of

orbiting electrons when exposed to an applied magnetic field. Diamagnetic substances are composed of atoms which have no net magnetic moments (i.e., all the orbital shells are filled and there are no unpaired electrons). However, when exposed to a field, a negative magnetization is produced and thus the susceptibility is negative.

Paramagnetic: a net magnetic field exists which is aligned to the external field. It relaxes when the external field is removed. In the presence of a field, there is now a partial alignment of the atomic magnetic moments in the direction of the field, resulting in a net positive magnetization and positive susceptibility.

Ferromagnetic: a net magnetic field exists which is aligned to the external field and remains when the field is removed. Unlike paramagnetic materials, the atomic moments in these materials exhibit very strong interactions. These interactions are produced by electronic exchange forces and result in a parallel or anti-parallel alignment of atomic moments. The exchange force is a quantum mechanical phenomenon due to the relative orientation of the spins of two electrons. Ferromagnetic materials exhibit parallel alignment of magnetic moments resulting in large net magnetization even in the absence of a magnetic field. They also can retain a memory of an applied field once it is removed. This behaviour is called hysteresis and a plot of the variation of magnetization with magnetic field is called a hysteresis loop, as shown below in Figure 1.

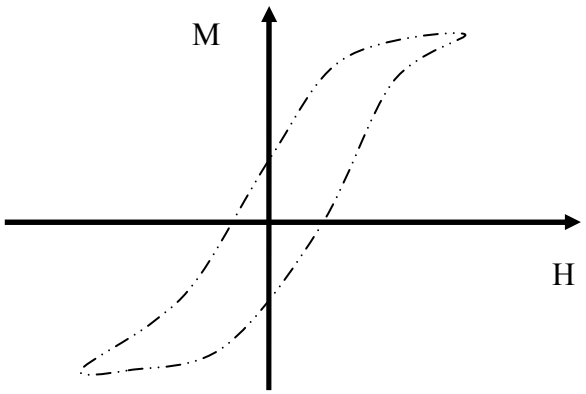

Figure 1: Magnetisation (*M*) versus magnetic field strength (*H*) for a ferromagnetic material.

Technically above magnetic saturation *B* continues to increase but at the paramagnetic rate which is 3 orders of magnitude smaller than the ferromagnetic rate.

Paramagnetic and diamagnetic saturations exist in theory but require immense magnetic fields to be reached in practice.

Antiferromagnetic: The magnetic moments of atoms or molecules, usually related to the spins of electrons, align in a regular pattern with neighbouring spins (on different sub lattices) pointing in opposite directions. Generally, antiferromagnetic order may exist at sufficiently low temperatures, vanishing at and above a certain temperature, the Néel temperature [8]. Above the Néel temperature, the material is typically paramagnetic. When no external field is applied, the antiferromagnetic structure corresponds to a vanishing total magnetization, by ordering electron spins in opposing fashion.

Capabilities of a Spin Polarised Positron Beam

The development of a spin polarised positron beam based on the Doppler broadening technique will be described below. Such a tool offers the capability to profile, in depth, dilute magnetic species or nano-magnetic structures in thin films via the "preferred" annihilation of electrons with opposite spin than positrons.

Polarisable electrons in a sample are the electrons that contribute to its magnetisation and determine its magnetic properties. Materials have specific electrons which can be polarised and in the case of iron are the four unpaired electrons in the 3d shell (out of a total of 6 in the 3d shell). By polarising these electrons and probing them with a spin polarised positron beam, one can change their "annihilation affinity" (likelihood of being annihilated), therefore changing the shape of the annihilation spectrum by annihilating electrons of a different shell thus a different energy.

2.2 Calculated contributions of electron shells to the annihilation spectrum and expected results for Fe

Calculations done by Dr Stephen Dugdale [9], using software called MIKA [10,11], show the contribution of individual shell electrons to the total spectrum for iron. This assumes a zero net magnetisation or polarisation. The calculations are shown below in figure 2. By increasing or decreasing the ratio of annihilations with 3d electrons, we can see the effect it has to the total spectrum. A comparison of a hypothetical spectrum with 0.1% increase in 3d annihilations with a zero net

magnetisation spectrum is shown below in figure 3, and the ratio of the two spectra is shown in figure 4.

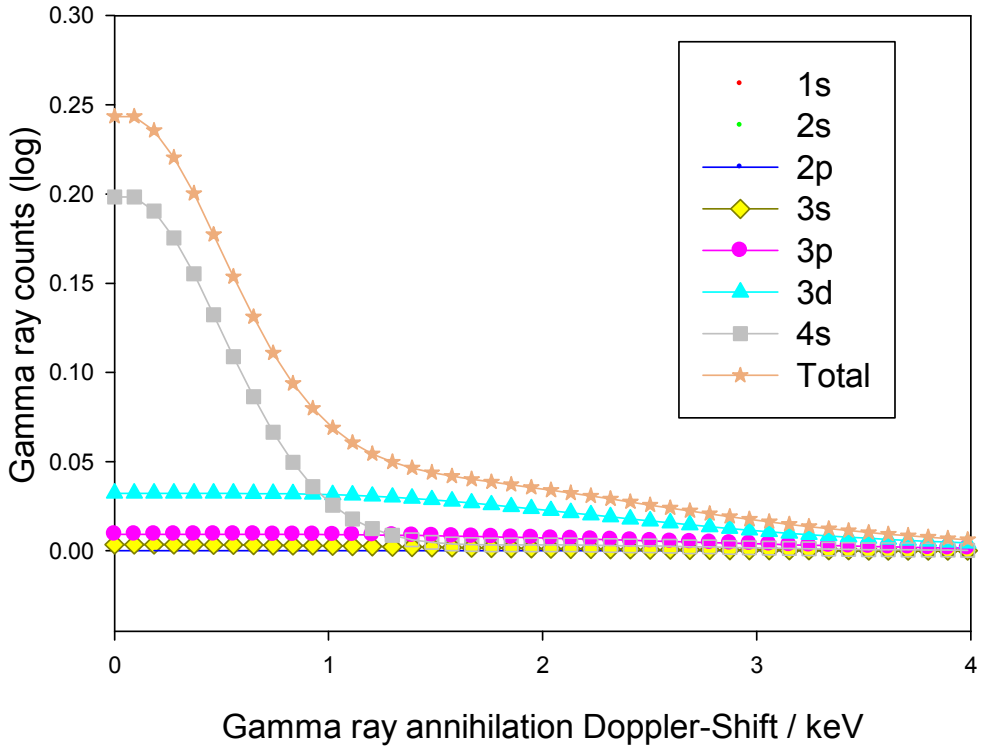

Figure 2: MIKA calculations of the individual contribution of electrons from different shells to the total annihilation spectrum (S.B. Dugdale [9]).

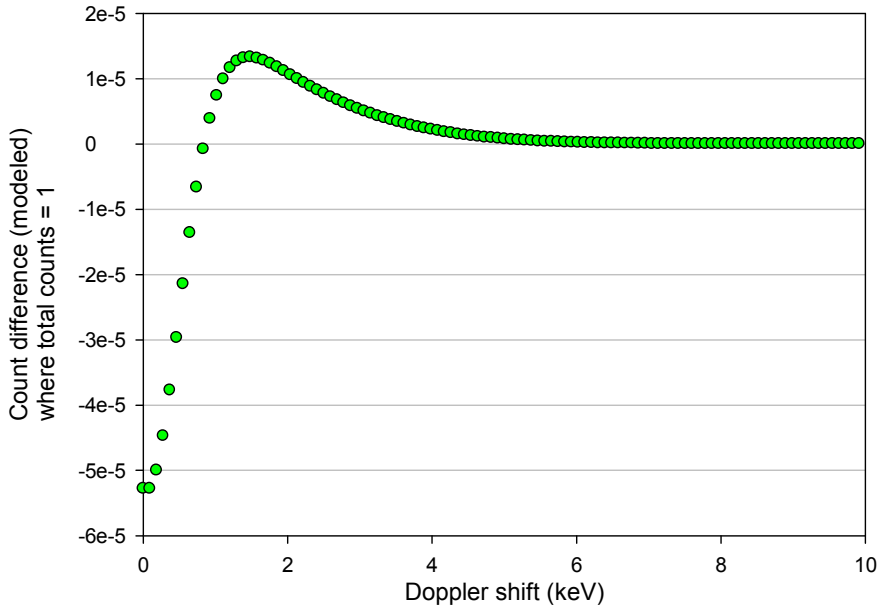

Figure 3: Difference between annihilation spectra as modelled (normalised to total counts =1) and 0.1% 3d annihilation increase(normalised to total counts = 1).

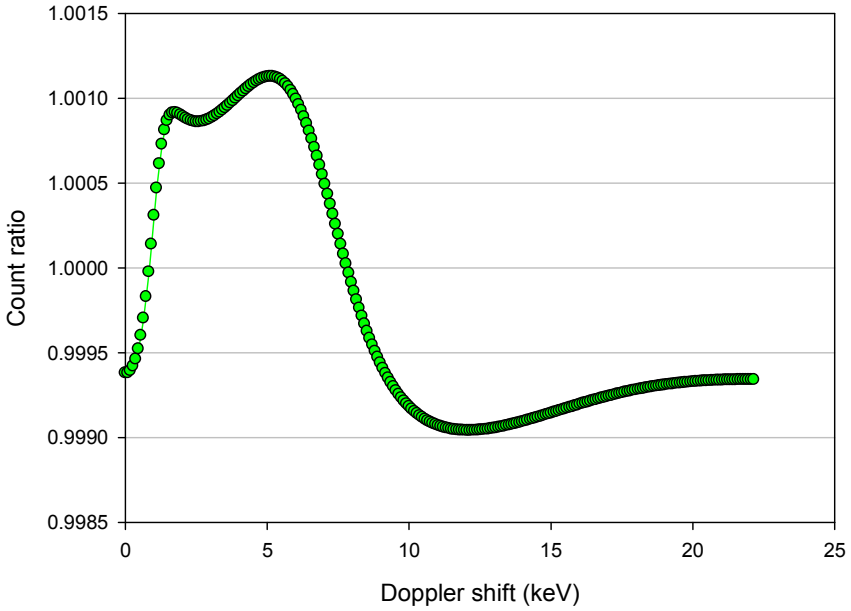

Figure 4: Ratio of spectra with and without a 0.1% 3d annihilation increase

These modelled changes in the spectra agree with previous work done using non-beam positron techniques [12]. The expected results from fig 8 have been convoluted with the detector resolution function (Gaussian of width 1.4keV). If the difference at E = 0 is set to 0 the expected change would look like fig 10.

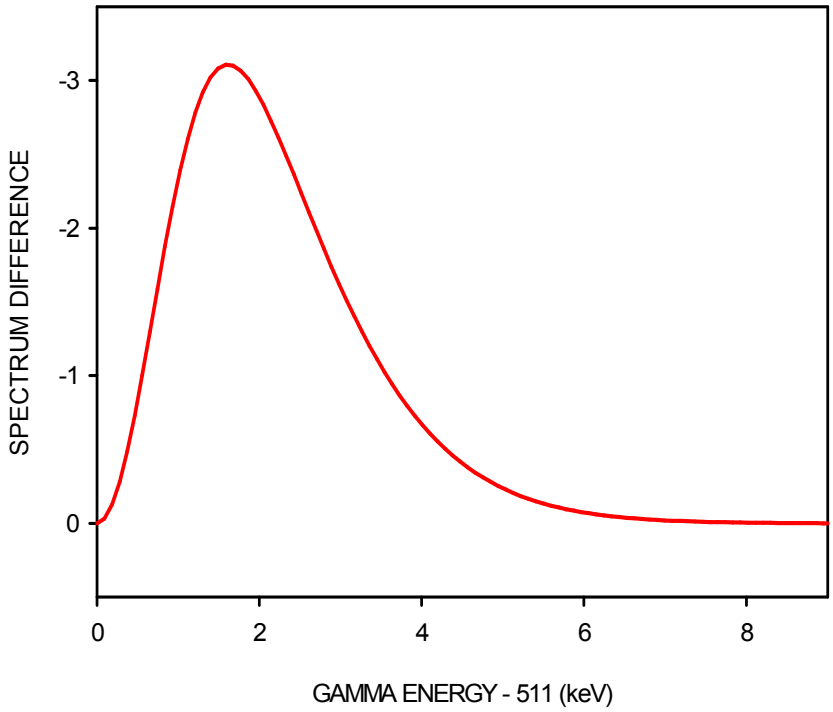

Figure 5: Simulated VEPAS spectrum difference

2.3 Development of a Spin Polarised Positron Beam

Preliminary Measurements

The first pilot measurements were made after a period of background research and familiarization with the equipment. Iron was chosen as the first sample because it is a ferromagnetic material with very high magnetic susceptibility. It has four out of six electrons unpaired in the 3d shell, meaning a relatively high population of the shell is polarizable. The most direct way of magnetizing the sample was to place a magnet behind it. A few neodymium magnets of various sizes and shapes were purchased, as shown in Figure 6 below.

Figure 6:. Left: Circular disc magnets of 10mm and 20mm diameter, and (right): Square magnets 5mm x 5mm. Both types are graded N42. [13]

N42 is a measurement of the quality of the magnet material, i.e. the energy stored within the magnet and the temperature range over which it can be used. It is also an indication of the strength of the magnet, in this case 1.42 Tesla under optimal conditions. In practice it was found that the actual strength of the magnetic field extending through the samples was much less - of the order of 0.14 Tesla. This was nevertheless deemed adequate.

It was then assumed that this field was enough to saturate the magnetization in a thin foil of annealed iron, as implied by other publications [14]. Two magnets were then mounted on the sample holder, one with its field direction parallel to, and one opposing, the direction of the guiding field of the positron beam (~ 50G). Then they were lowered into the vacuum chamber in order to observe the behaviour of the positron beam in such strong, rapidly changing magnetic field along the beam axis. What was observed (Figure 7 below) was not unexpected:

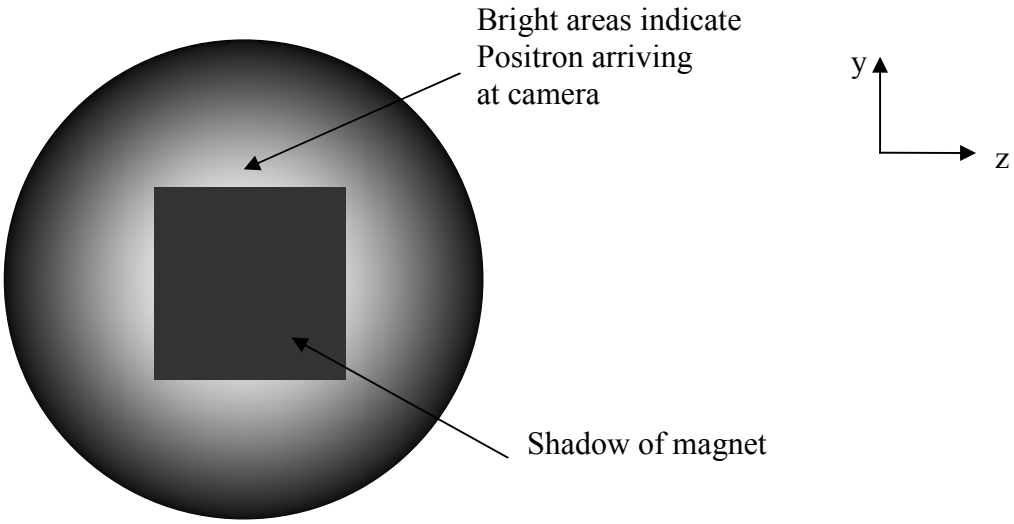

Figure 7: Representation of image seen by the CCD camera when a magnet is present in aligned position.

The difference between the aligned magnet and the reversed one was the size of the bright area surrounding it, this being smaller in the aligned position (or arguably the magnet seemed bigger).

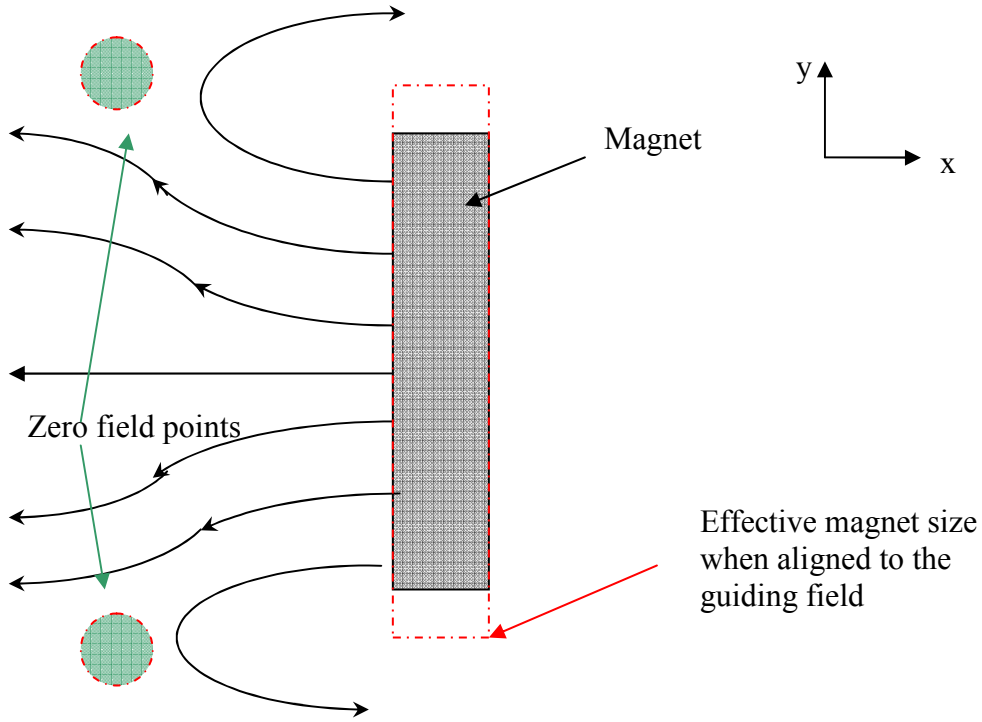

Figure 8: Magnetic field lines when the magnet is aligned to the guiding field
(guiding field in the +x direction / positrons traveling in the +x direction)

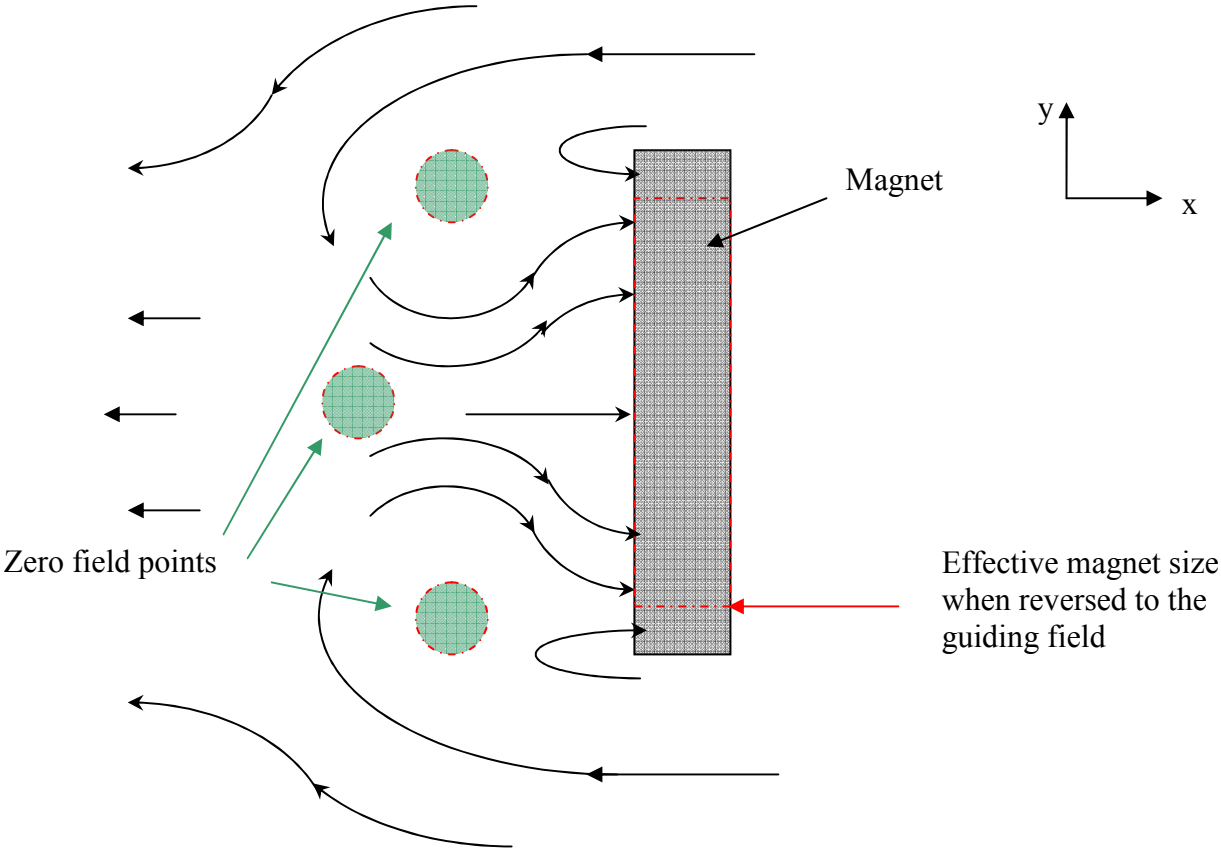

Figure 9: Magnetic field lines when the magnet is reversed to the guiding field
(Guiding field in the –x direction / positrons traveling in the +x direction)

Positrons are guided to the target area irrespective of field direction; we can see how the effective shadow of the magnet changes from figures 8 and 9. It was assumed that positrons could 'jump' across the zero field points from a field line in one direction to one in the opposite direction.

The next logical step was to place a sample in front of the magnet and measure the *S* parameter and line shapes using an aligned magnet and with no magnet at all. Preliminary results were quite promising. First the annihilation line spectra – taken with a positron beam energy of 30 keV, corresponding to a mean depth of $\sim 1.2\mu m$ and so essentially in the bulk of the sample - were normalised (Figure 10) and differences were seen in the plots of spectrum difference and ratio, examples of which are shown in figures 11 and 12.

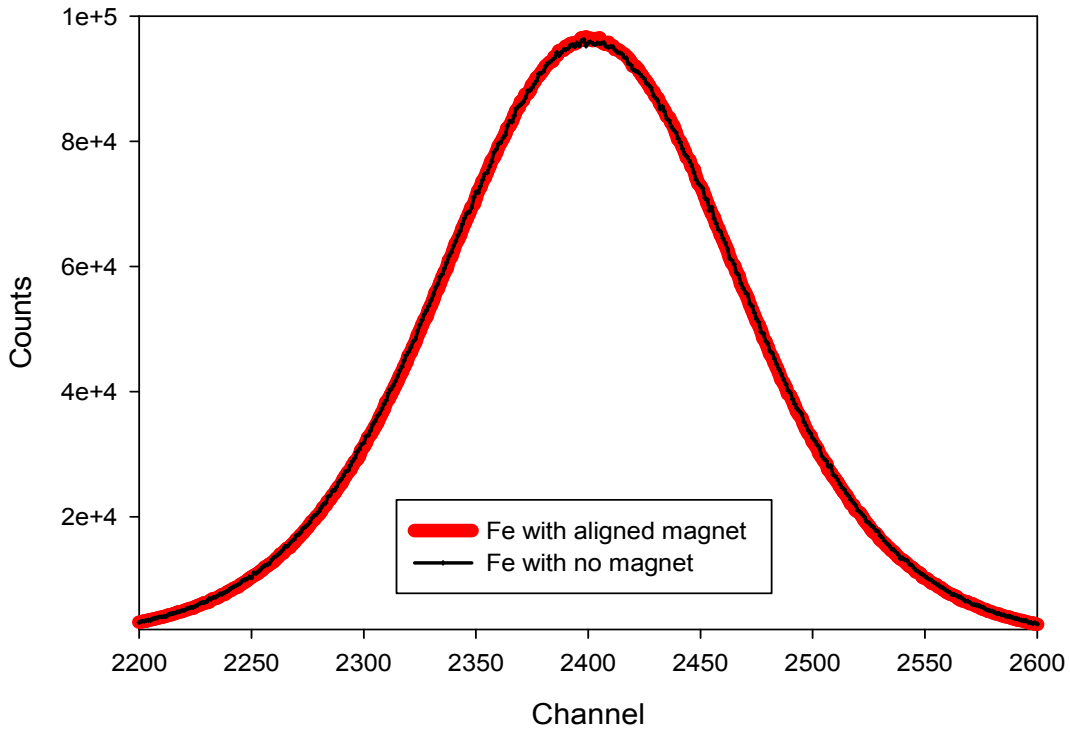

Figure 10: Normalised annihilation line spectra for Fe in front of an aligned magnet and Fe with no magnet behind it, taken at a positron energy of 30keV. There are 18.8eV per channel and channel 2399 corresponds to the 511keV peak.

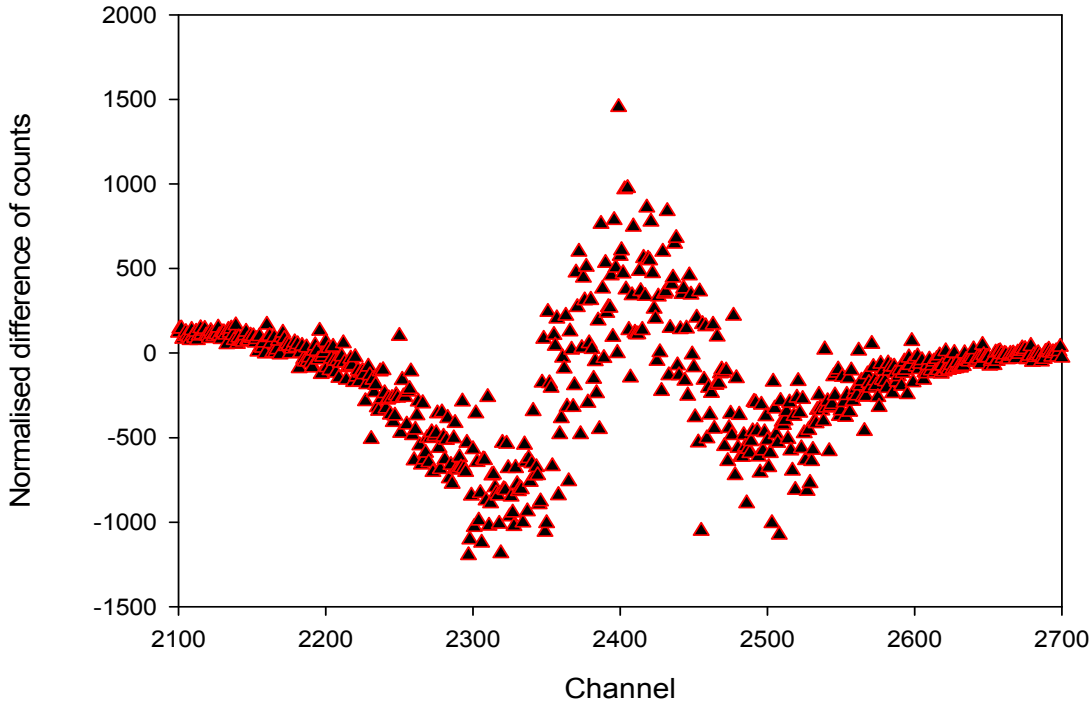

Figure 11: Difference between normalised spectra of figure 15. (Spectrum with no magnet present subtracted from spectrum with magnet present) There are 18.8eV per channel and channel 2399 corresponds to the 511keV peak.

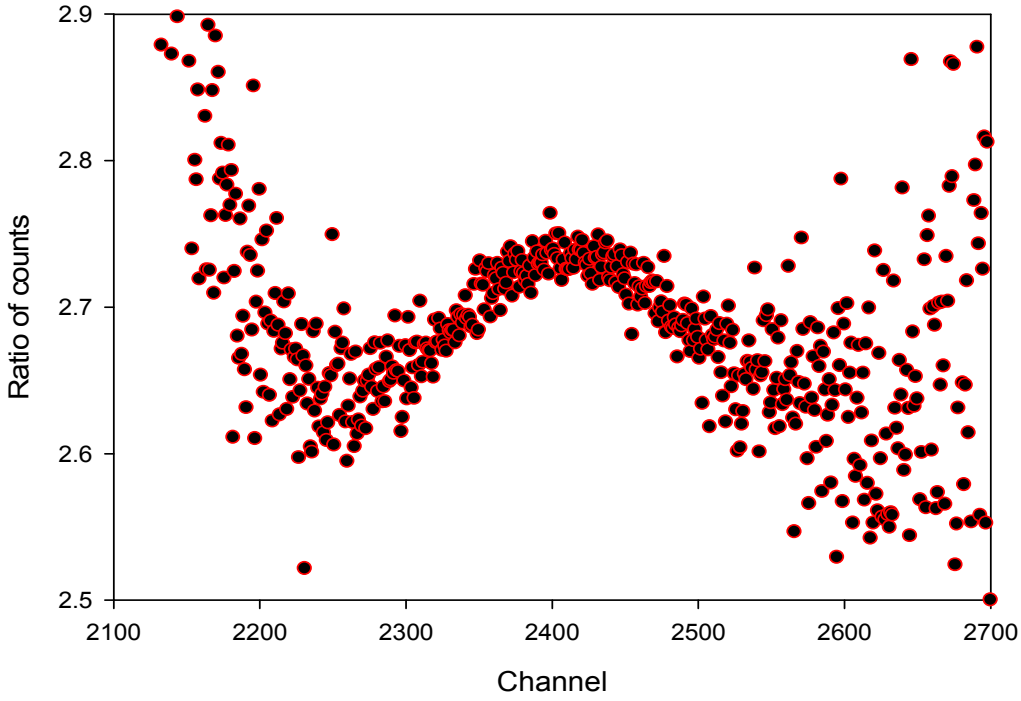

Figure 12: Ratio of normalised spectra of figure 15. (Spectrum with magnet present divided by spectrum with magnet present.) There are 18.8eV per channel and channel 2399 corresponds to the 511keV peak.

In Figure 15 we can see the peak at channel 2399 which corresponds to 511keV. Although difficult to see any difference between the two spectra directly in figure 15, it is clearly evident in figures 16 and 17 that the spectrum taken with the magnet present was narrower than that taken without the magnet. This narrowing of the line shape, if real, would imply the annihilation by positrons by lower momentum electrons, leading to less Doppler broadening. The electrons able to polarize in iron are the four unpaired electrons situated in the 3d shell, having energies of approximately 9.5eV; the mean momentum of these electrons in a direction parallel to the detector axis corresponds to a Doppler shift reasonably consistent with the minima in the difference spectrum, thus providing an explanation for the narrowing of the line shape.

The exact polarization of the positron beam was unknown. It is accepted that positrons are spin polarized in the original direction of emission from the radioactive source and the direction of their polarization will remain the same throughout their

lifetime in our system [15]. The source-moderator distance was ~1mm, allowing maximum positron collection by the moderating mesh. However, some of the positrons are not wanted. The spin polarization component of the positrons in the direction of the beam axis (i.e., the *x* direction) is what affects the measurements. Positrons with polarization *opposite* to the one required - i.e., those emitted from the source directed away from the sample, are highly scattered in all directions, including towards the sample (back-scattered positrons). Conversely, positrons ejected with small angles to the forward direction would have maximum positive effect, and it was therefore necessary to attempt to limit the positron used to those in this latter category [16]. The source available for these preliminary measurements had a tantalum backing that has a high back-scattering coefficient, and so the only option available was to position the Na-22 source further away from the moderator mesh, thereby decreasing the acceptance angle of positrons at the mesh, and selecting positrons with spin polarization close to the beam axis (Figure 18). Major [17] calculated that the optimum acceptance angle – i.e., one which shows the best compromise between axial polarization and beam intensity (which decreases as the acceptance angle decreases) – is about 46º.

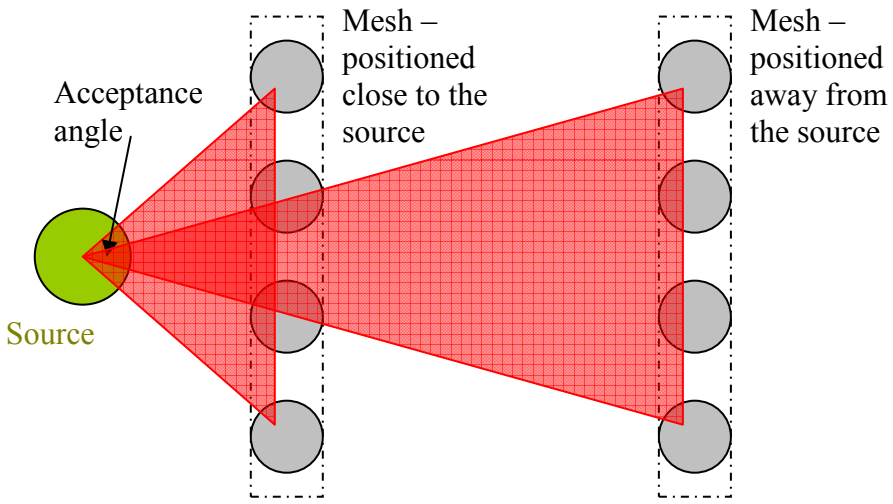

Figure 13: Demonstration of the dependence of acceptance angle on source-moderator separation

The source was therefore positioned at distances of 12 and 24 mm from the moderating mesh and similar measurements as before were taken, the results of which are shown in figures 14 and 15.

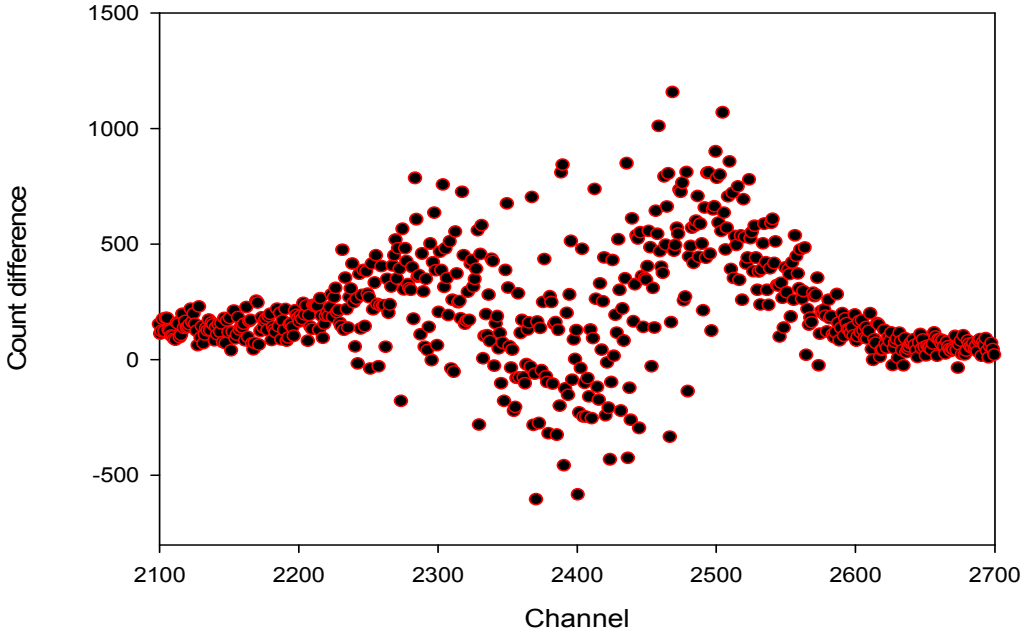

Figure 14: Normalized difference between spectra for Fe in front of an aligned magnet and Fe without a magnet, with the source pulled back to 12mm, taken at 30keV. There are 18.8eV per channel and channel 2399 corresponds to the 511keV peak.

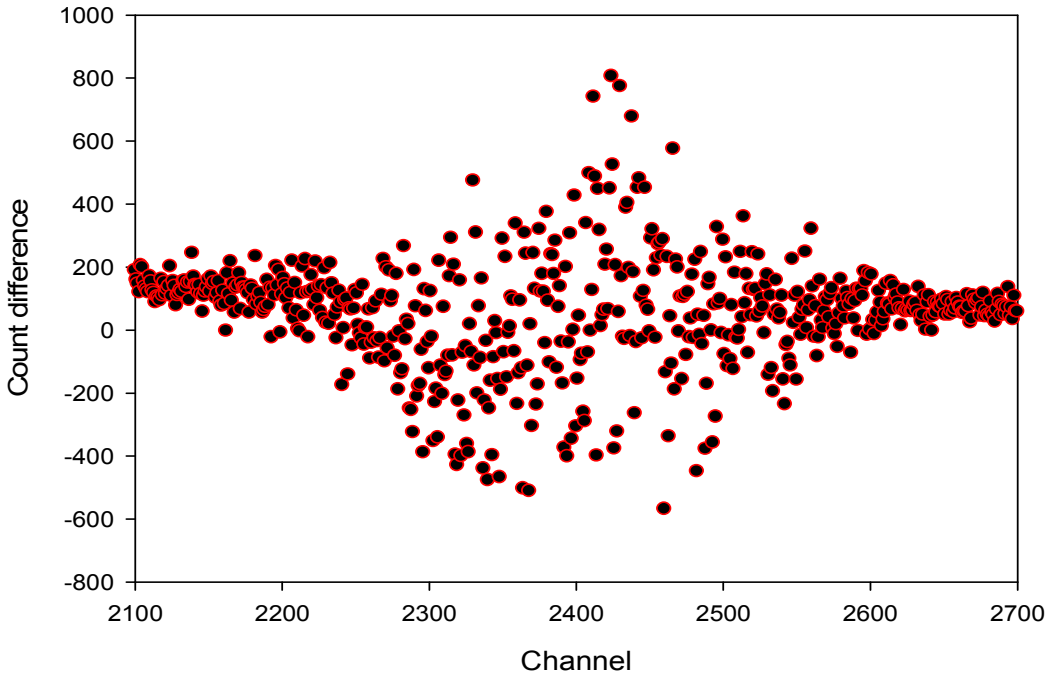

Figure 15: Normalized difference between spectra for Fe in front of an aligned magnet and Fe without a magnet, with the source pulled back to 24mm, taken at 30keV. There are 18.8eV per channel and channel 2399 corresponds to the 511keV peak.

The results were the complete opposite to what was expected. For the source at 12mm (figure 14) not only did the absolute difference between spectra decrease, but the signal-to-noise ratio deteriorated and the became broader not narrower. For the source at 24mm (figure 15) the spectra became so noisy (low count rate and bad signal-to-noise ratio), that it is debatable if one can deduce any useful information from them. It was found that the annihilation count rate was dramatically decreased due to the smaller acceptance angle from the mesh but also due to the source-moderator potential different not being as effective. Increasing this potential difference did not have a significant effect, so a second mesh was placed 1mm away from the original one as shown below in figure 16.

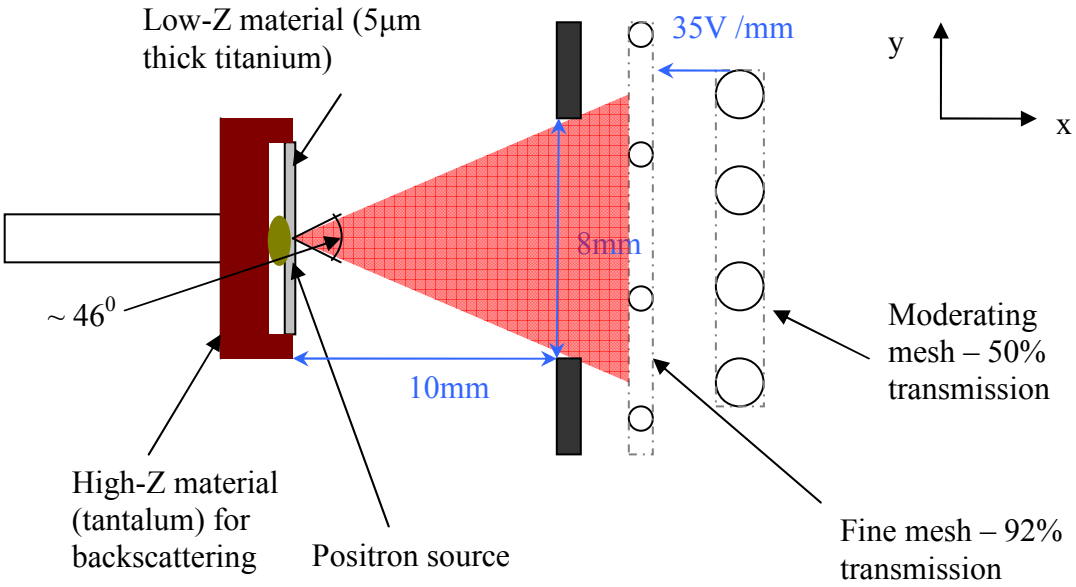

Figure 16: Updated setup of the source and its immediate surroundings.

With this new setup we have a constant potential difference over a constant distance on the left side of the moderating mesh but at a cost of 8% of the positrons. For different potentials on the extra mesh the count rates of positrons were noted so that its effect could be seen. The source was pulled far back (at 24mm).

Table 1: The effect of the coarse mesh potential on the positron count rate

Coarse mesh voltage / V	**Moderating mesh voltage / V**	**Potential difference/ V**	**Effective count rate/ positrons s^{-1}**
135	100	35	73
100	100	0	62
No mesh present	100	-100	37

The positron count rate at a voltage of 135V is doubled, therefore having a gain bigger than the 8% penalty of the mesh's transmission in a 19^0 situation (i.e. the source pulled back to 24mm).

Measurements were repeated for three different source-mesh distances, at 76^0 (original position) at 36^0 and at 19^0. The results seen are show below in Figure 17.

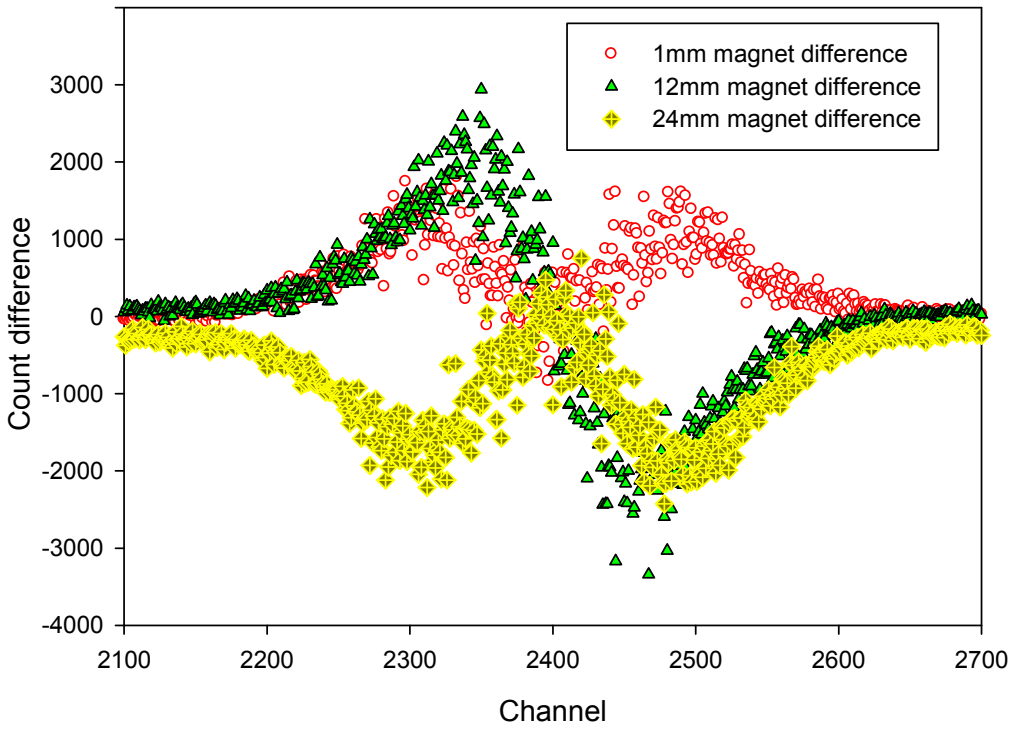

Figure 17: Gamma spectrum difference for source-mesh distances of 1mm, 12mm and 24mm. There are 18.8eV per channel and channel 2399 corresponds to the 511keV peak.

For the 12mm measurements it was clearly seen that there has been a shift in the peak between the two runs. This would suggest a general instability in the system that could explain the change in direction in the difference seen between 1mm and 24mm settings. Measurements were consequently made for a non magnetic sample to check the stability of the system. The same setup was used but the iron sample was replaced with a silicon sample of the same shape and size. The results are shown below in Figure 18.

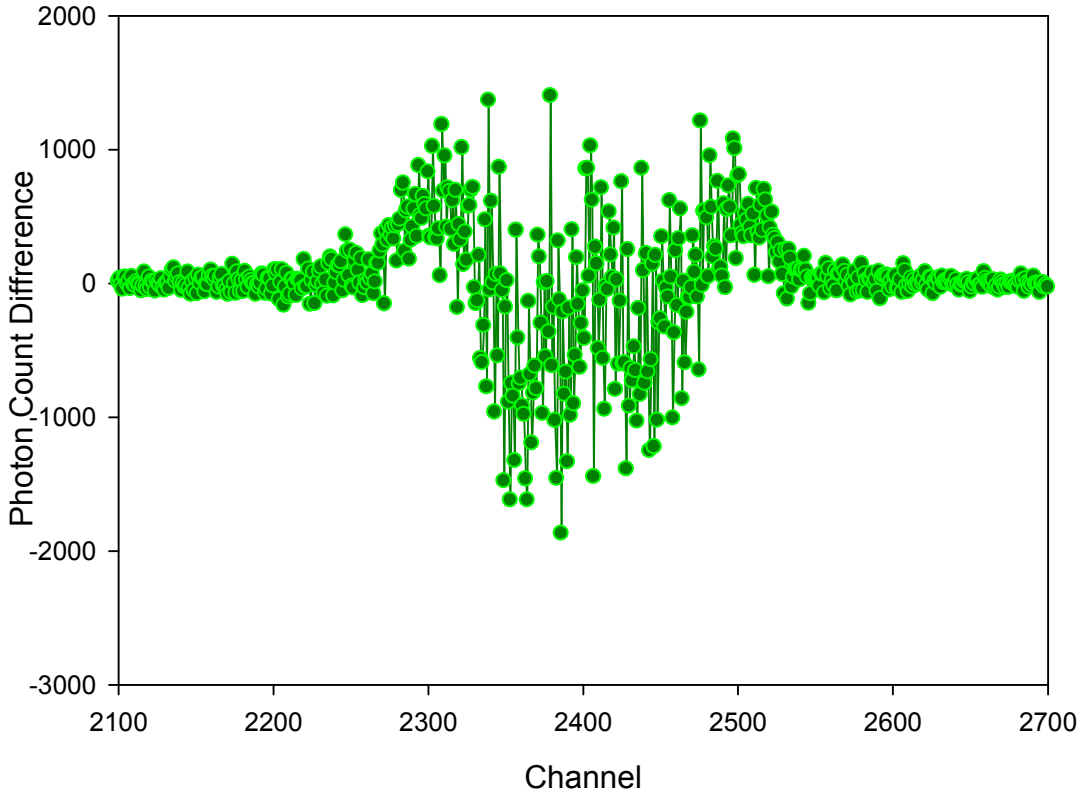

Figure 18: Spectrum difference for Cz silicon. There are 18.8eV per channel and channel 2399 corresponds to the 511keV peak.

The results from the silicon measurements meant that all previous results were invalid, probably because the magnet positioned behind the sample deflected some positrons into material other than the intended target. The larger distance between the source and moderator mesh, even with an aperture present, increased the mesh area irradiated by positrons and, consequently, the magnetic field uniformity became crucial in the sample chamber. The system had to be re-configured to be more stable and to produce null results for non-magnetic samples.

Magnetic Lensing

A magnetic holder was designed to focus the beam on to the centre of the sample. This new arrangement decreased the effective size of the beam from ~8mm to ~ 5mm, as shown schematically in Fig. 23, and became rounder and brighter (with no sample present).

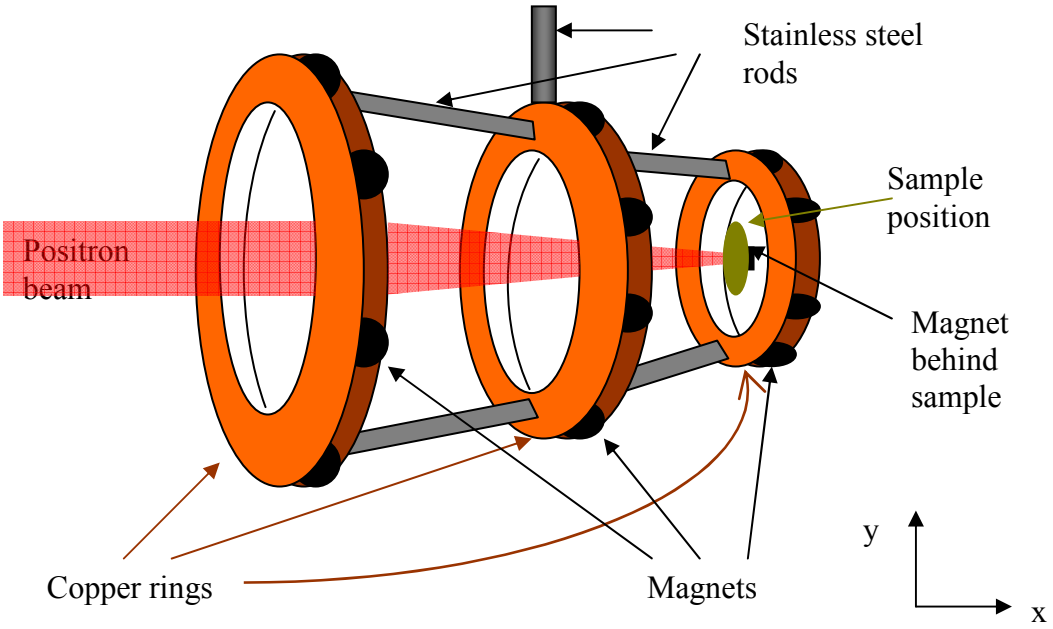

Figure 19: A magnetic lens system with 3 rings each supporting nine 10mm-diameter magnets, twelve 5mm and nine 5mm side square magnets, respectively. The magnet behind the sample has 10mm diameter. All the magnets are in reversed direction to the guiding field except the one behind the sample which is aligned to it.

A sketch of the field lines is shown below for one ring (Figure 25).

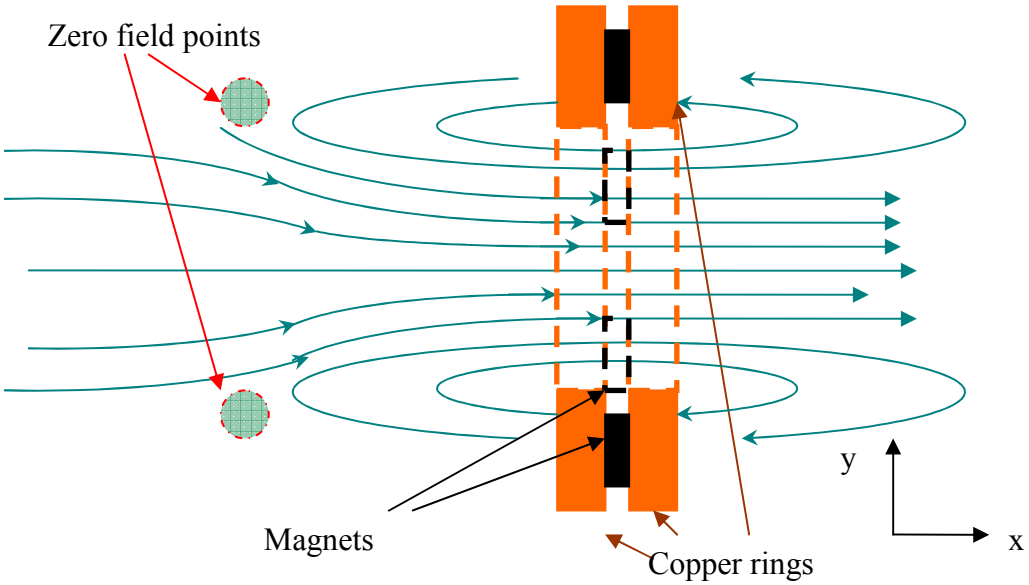

Figure 20: The magnetic field lines passing through one of the rings of the magnetic lens. For all three lenses the "squashing" of the lines is repeated, reducing the beam to a smaller cross-section.

The lens was then tested on a Si sample and compared to a typical Si measurement with the conventional sample holder, shown below (Figure 21). After repeated checks it was concluded that the positrons were thrown from their path whilst traveling through the last ring of the lens. This was due to the presence of the magnet in the middle of the ring creating a complex localized field. The smallest ring of the lens was then removed and the measurements repeated (Figure 22). The magnetic lens itself was effective, but the presence of the middle magnet with or without the lens was the same; expelling positrons from their path to annihilate in another material, most probably stainless steel. This effect was not seen in earlier *S* parameter measurements, as stainless steel has a similar *S* parameter value to iron but very different to silicon.

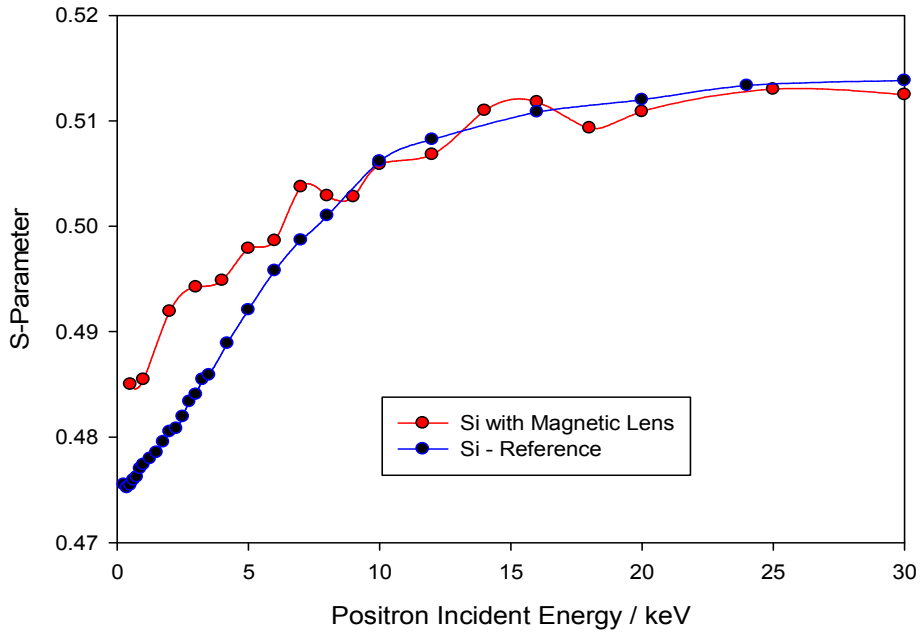

Figure 21: Silicon *S*-parameter measurements using the magnetic lens (3 rings) with a sample magnet compared with a measurement using the conventional sample holder.

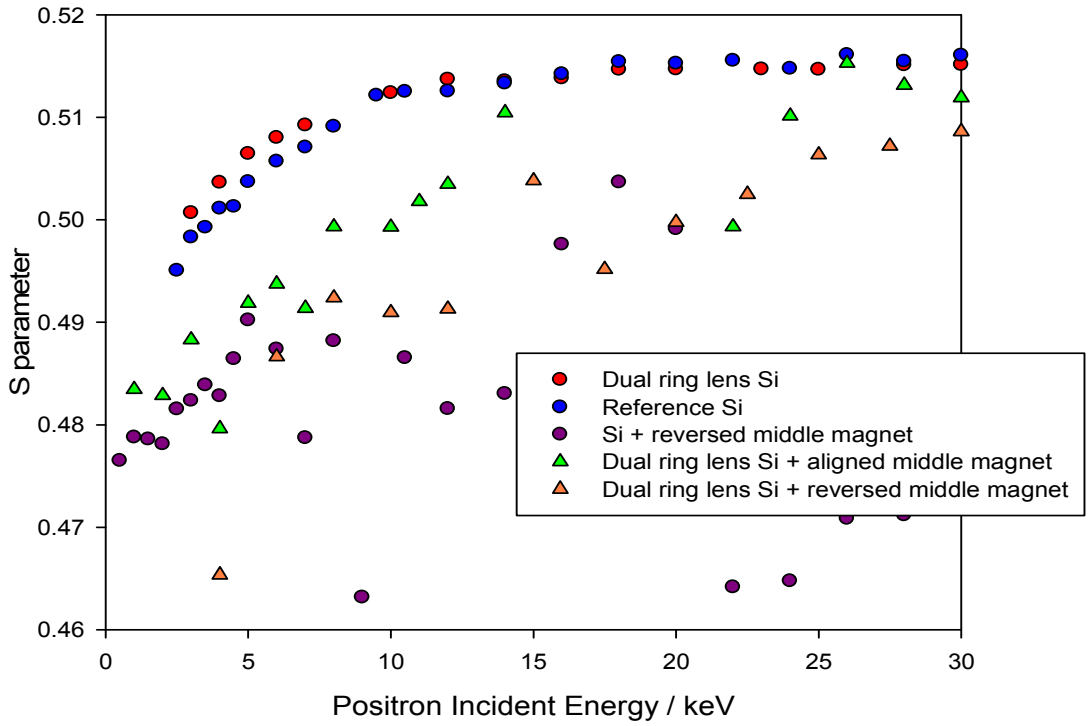

Figure 22: Silicon *S*-parameter measurements using the magnetic lens (2 rings) and using the classical sample holder (reference) with and without a middle (sample) magnet.

Using a single ring lens consisting of six 20mm magnets equally spaced was also tested but had a similar outcome (i.e. a stronger focal magnetic field would make the field lines at the sample more uniform). It was concluded that the magnetic focusing scheme was impractical.

Electromagnet

The need for a larger, more uniform field led to the design of an electromagnet to be held in the vacuum around the sample. This was designed to fit through the sample chamber opening and was made of an alluminium tube, 50mm long with an internal diameter of 50mm, copper rings and teflon-coated wire,. A copper ring was engineered to fit inside the electromagnet to hold the sample (Figure 23). The electromagnet was capable of producing a sustained magnetic field of ~120G when operating at 1.56A. Although this field was hardly enough to magnetize most magnetic samples, it was enough to partially magnetize iron.

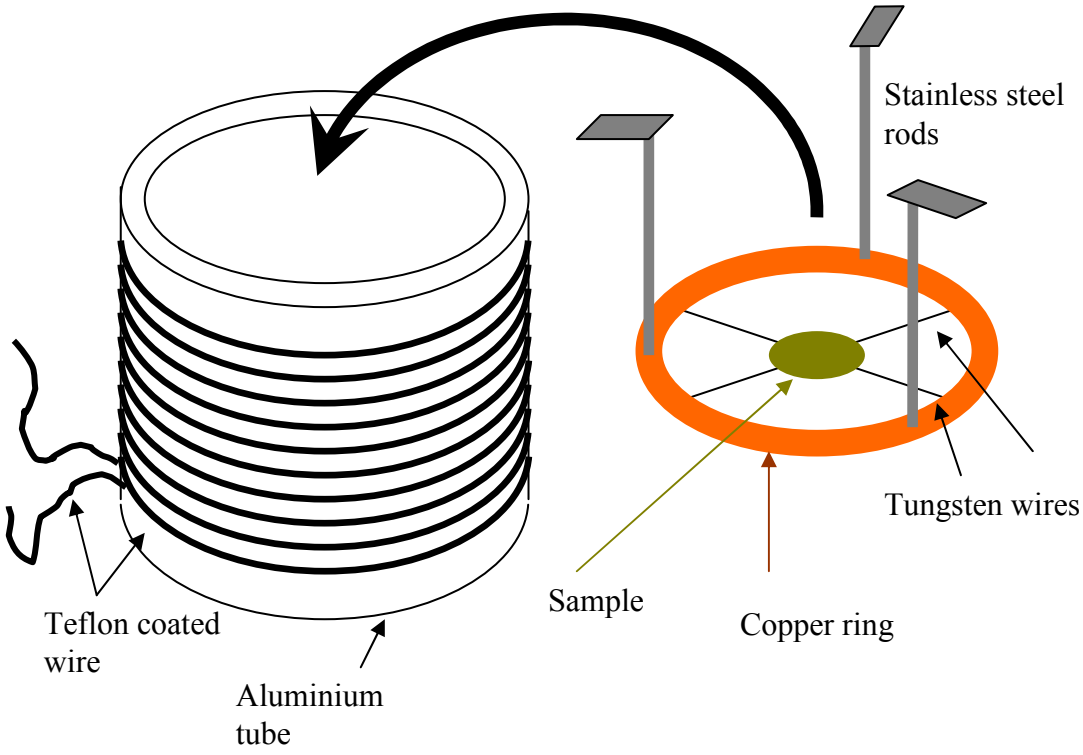

Figure 23: Electromagnet and its sample holder fitting

S parameter measurements for a silicon sample with near surface silica layer (Figure 24) and for iron (Figure 25) were made using the electromagnet.

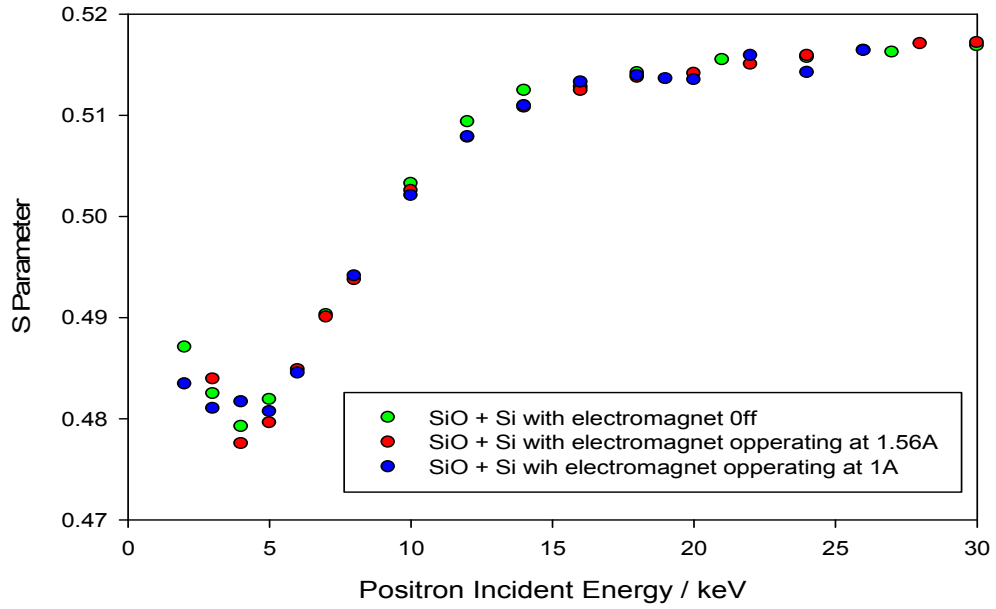

Figure 24: SiO_2 on Si measurements using the electromagnet with currents of 1 and 1.56 amps

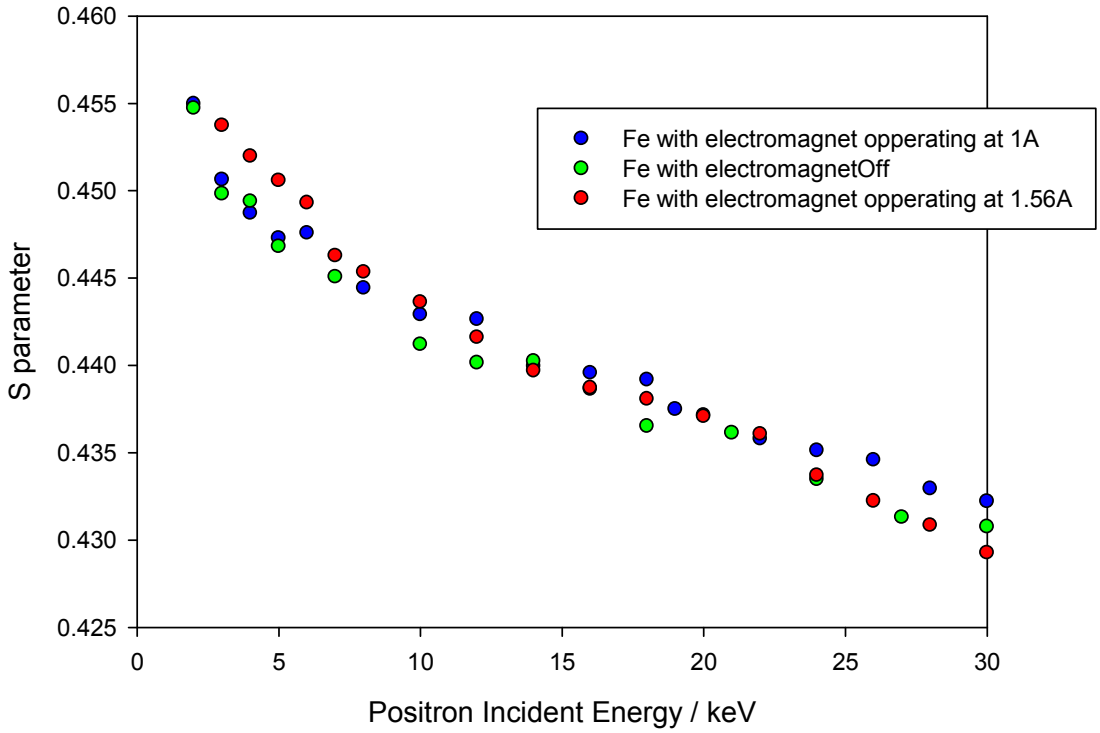

Figure 25: Fe measurements using an electromagnet at 1 amp and 1.56 amps

The silicon sample data were encouraging in giving an overall null difference in *S* parameters with and without the electromagnet in operation, with values confirmed by using the second positron beam in the laboratory. Unfortunately the differences seen between iron measurements were inconsistent, showing fluctuations in *S* parameter that had no clear explanation. When the electromagnet was removed from the sample chamber it was found that the copper ring had oxidised and the electromagnet was too hot to touch. This implied that the temperature of the electromagnet inside the vacuum was at least 100 ºC, increased by the poor heat conductivity of the system. The heating and cooling of iron was then thought to be blamed for these fluctuations in the *S* parameter value, so a time-dependent measurement of *S* parameter was made (Figure 26).

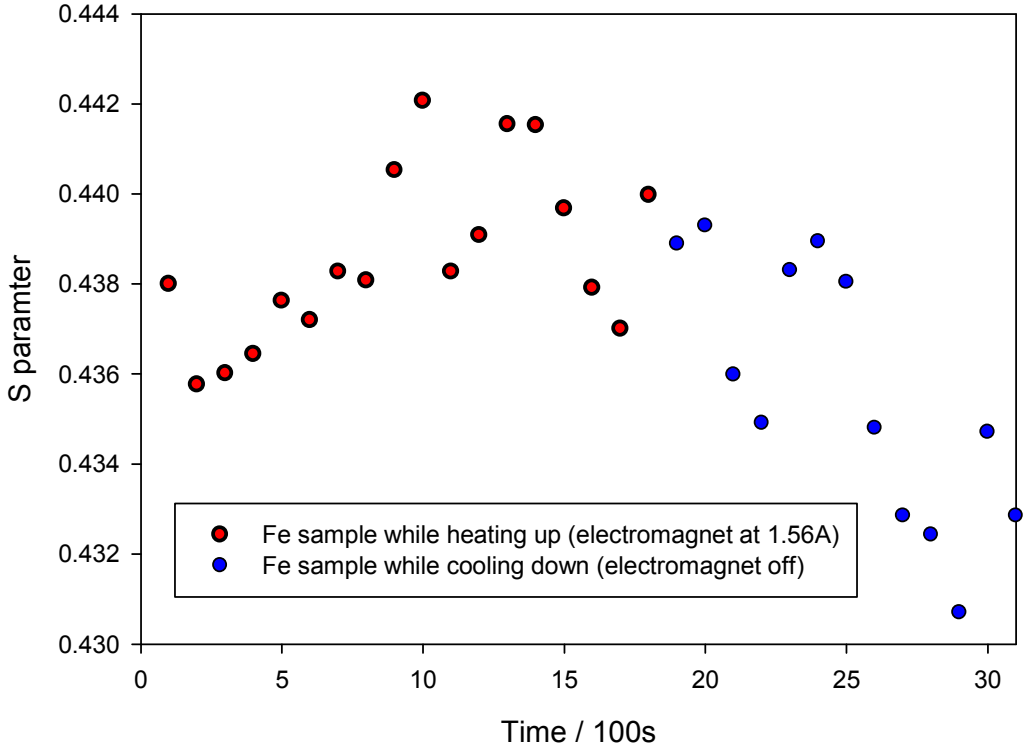

Figure 26: *S* parameter for iron at a beam energy of 14.5 keV while it is heating up with the electromagnet on, and while cooling down with the electromagnet off.

As seen from figure 31, the *S* parameter of iron is changing. It seems to increase while the sample is being heated up and decrease when it is cooled down.

It became clear that a simple electromagnet would not be powerful enough to magnetize any sample without significant heating effects. Having a larger magnet outside the vacuum system was not an option for practical reasons. It was thus decided to exploit the six guiding coils already positioned around the beam.

Field reversing measurements

The beam's guiding field is here used to magnetise the sample. This scheme had been considered before, but (a) the effect of the guiding field when reversed on the second, neighbouring beam in the laboratory was thought to be significant enough to render the procedure impractical, and (b) the **ExB** filter in the system works properly only with the guiding field in one direction.. However, problem (a) was addressed by synchronising measurements in the two beams, and the effects of reversing the guiding field direction of one beam on the other could be allowed for. Problem (b) was returned to later.

Iron reaches a highly magnetised state (>95%) in external fields of the order of ~500G, meaning that the existing strength of the guiding field (~60G) would only partially magnetize the sample [18] but this depends on the type of iron. Measurements of the normalised annihilation γ ray spectra for iron taken with the magnetic field in two directions always showed a clear and large difference which was consistently similar in shape; an example is shown in Figure 27.

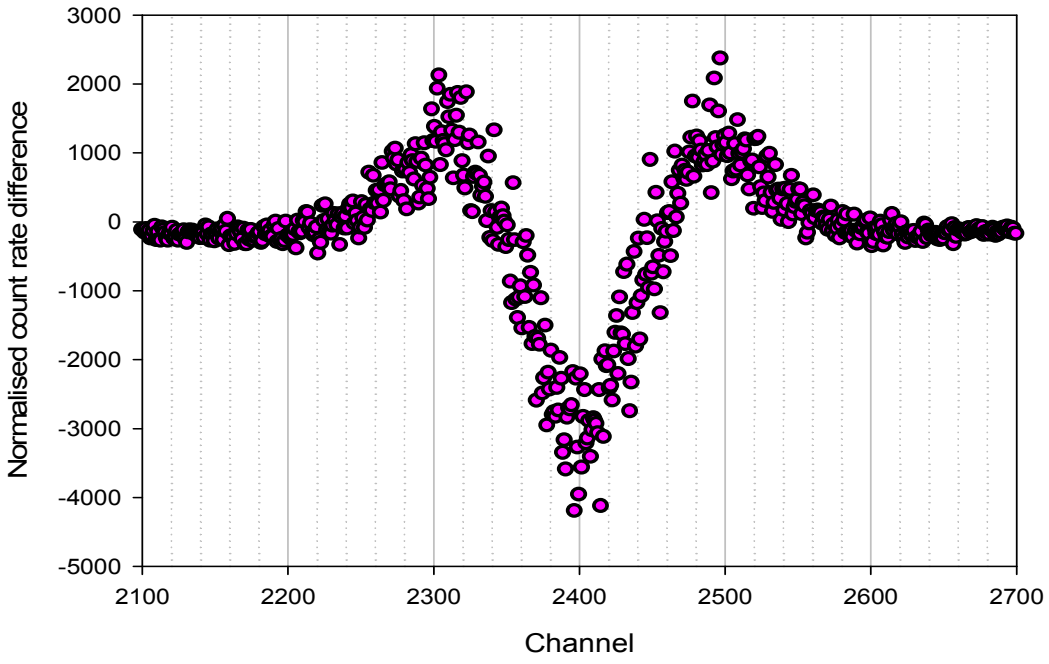

Figure 27: Spectrum difference for iron, between guiding field in original direction and guiding field in reversed direction, taken at 30keV. There are 18.8eV per channel and channel 2399 corresponds to the 511keV peak.

The initial measurement for silicon (figure 28) showed no such difference. However, attempts to repeat the null result for silicon were unsuccessful, showing a difference in line shape between the two field orientations similar to the one seen in iron but approximately half in magnitude and of width (figure 29). It was noted that the beam in the reversed field condition was elongated and cigar-shaped.

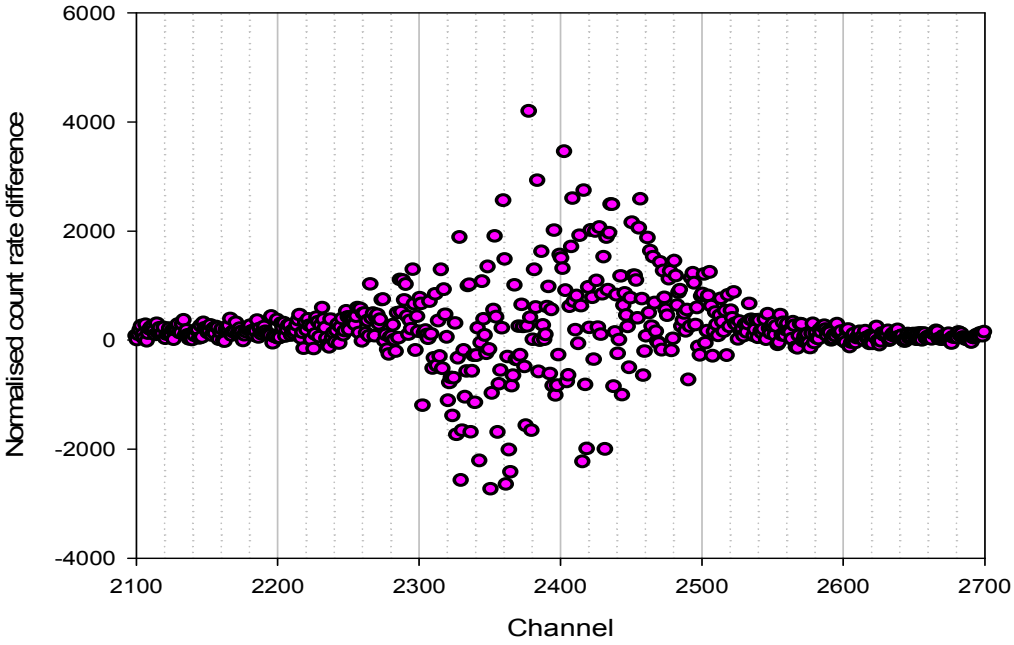

Figure 28: Count difference for silicon, between guiding field in original direction and guiding field in reversed direction, taken at 30keV. There are 18.8eV per channel and channel 2399 corresponds to the 511keV peak.

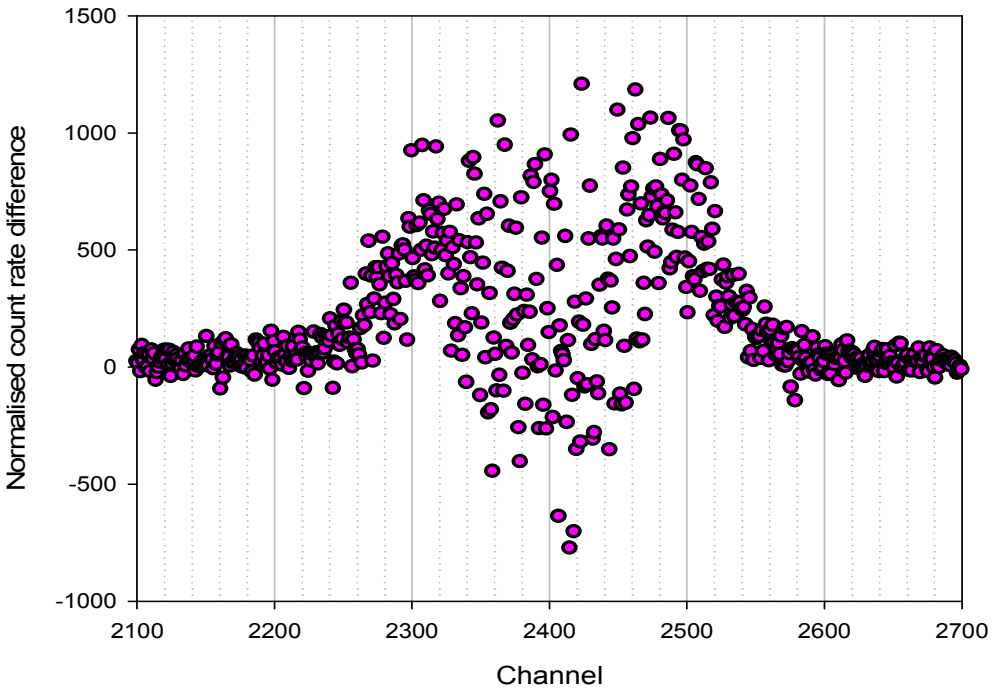

Figure 29: Count difference for silicon, between guiding field in original direction and guiding field in reversed direction after repeated measurements, taken at 30keV. There are 18.8eV per channel and channel 2399 corresponds to the 511keV peak.

To investigate whether the inconsistent silicon difference and the consistent iron difference were due to the same cause, measurements with the same field direction taken at different times were made and compared (Figure 30). A big shift in the spectrum peak position between the two measurements was apparent. Shifts in peaks result in the broadening or narrowing of the spectrum, as the electronic equipment of the system tries to compensate for any potential drifts of the peak via a digital stabiliser. In figure 31, the drift has been compensated for in the data analysis (by positioning the two peaks together) but the effect of the drift is still apparent.

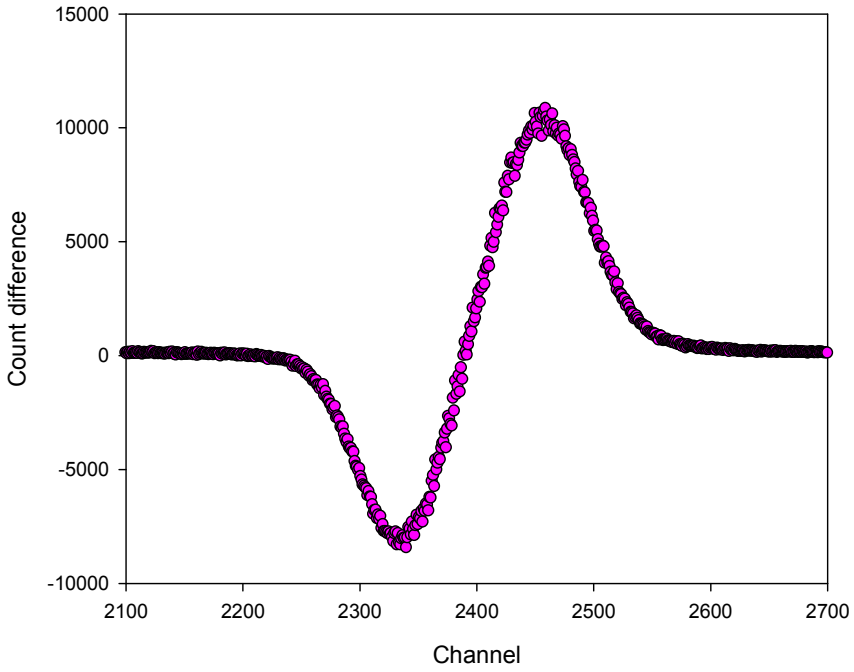

Figure 30: Peak drift between spectra for a silicon sample taken at 30keV at different times. There are 18.8eV per channel and channel 2399 corresponds to the 511keV peak.

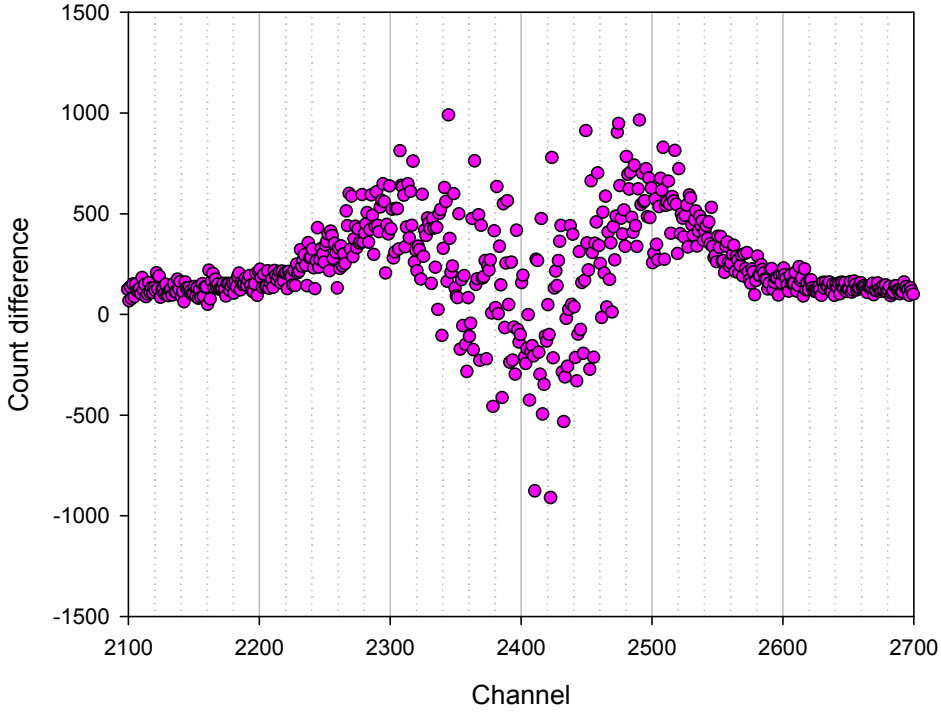

Figure 31: Si difference caused by the drift of the spectrum peak, at 30keV. (Data are those of Figure 30 with the peaks shifted to make their centres coincide.) There are 18.8eV per channel and channel 2399 corresponds to the 511keV peak.

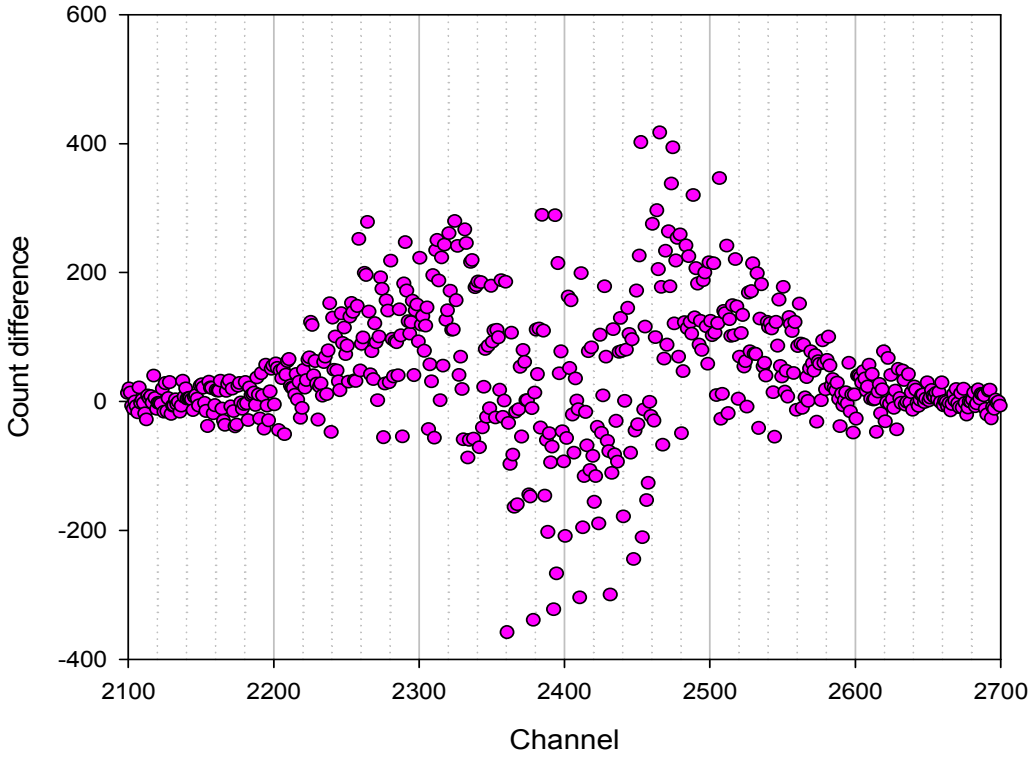

Figure 32: Fe spectrum difference caused by the drift of the spectrum peak, at 30keV. There are 18.8eV per channel and channel 2399 corresponds to the 511keV peak.

The change of shape and quality of the beam from an original guiding field setup (G) and a reversed guiding field setup (R) was a possible cause of 'false' results, as was possible electronic noise.. The latter was investigated thoroughly and a high frequency noise was found in the earth of the system when the laboratory lights were switched on. The problem was dealt with by replacing the lights with newer ones.

The reason the quality of the beam changing when the field was reversed was investigated. The ***ExB*** plates of the system are curved, such that the deflection of slow moderated positrons do not substantially distort the beam [19]. This only operates when the guiding field is in one direction (Figure 33(a)). In order to rectify this, one could replace the deflection system with cylindrical ***ExB*** plates, as in Figure 33 (b), or use two pairs of ***ExB*** plates, one for each direction of field (Figure 33(c)), or deflect the positrons by using magnets, Figure 33 (d). Option (d) was tried first since it was simple to execute, if rather crude.

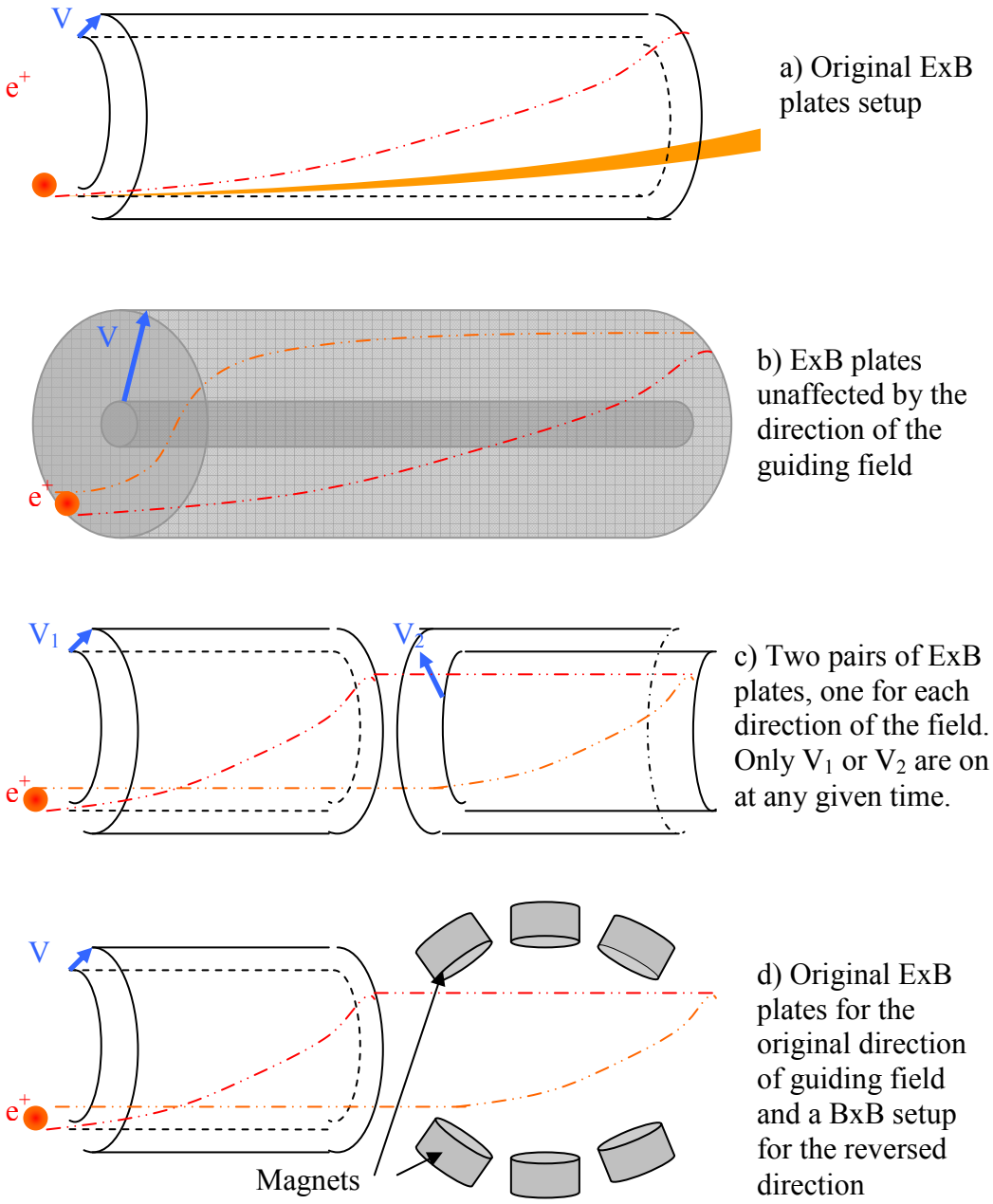

Figure 33: The original setup of the ExB plates (a) showing the fanning of the beam in Reversed field mode and three proposed alternatives (b), (c) and (d), as discussed in the text. The path of the positrons is shown in red for the original direction of the field (G) and in orange for the reversed direction (R).

The new setup was tested on an iron sample. Option (d) led to a deflected beam with reversed field (R) of similar shape and intensity as for the standard guiding field (G). Stability was demonstrated by measurements made under the same conditions (Figure 34) and for Fe with a magnet in both field directions (Figure 34).

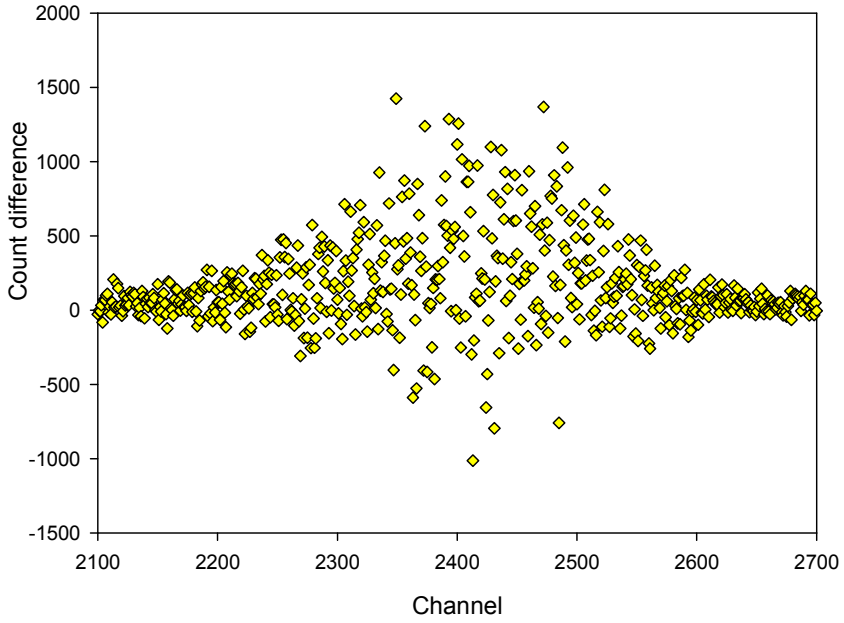

Figure 34: Comparison of measurements taken under identical conditions, showing no change and confirming the stability of the system. There are 18.8eV per channel and channel 2399 corresponds to the 511keV peak.

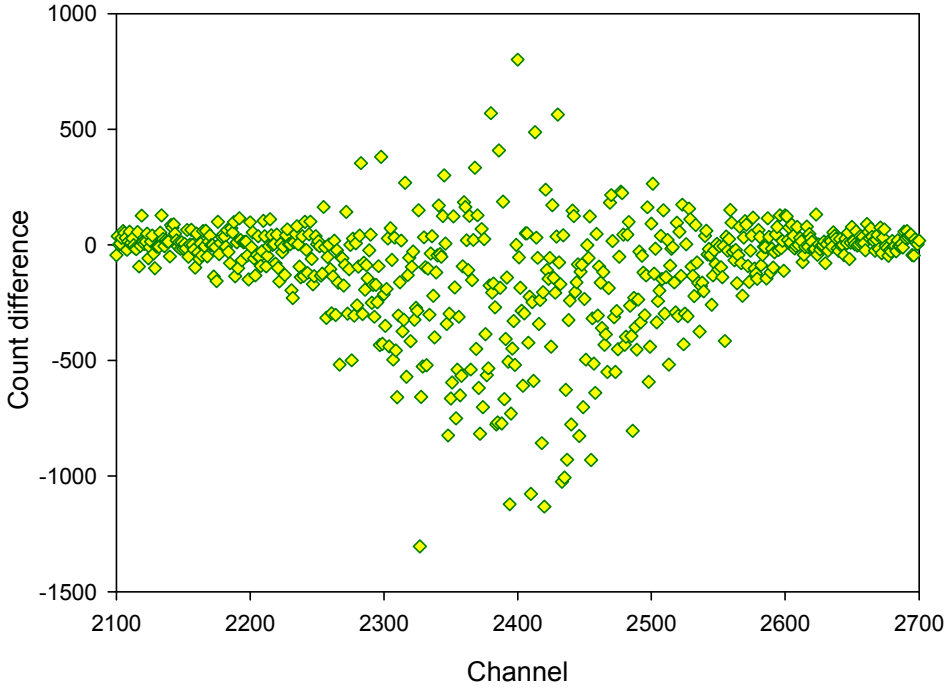

Figure 35: Spectrum difference for Fe with G and R field directions. There are 18.8eV per channel and channel 2399 corresponds to the 511keV peak.

Large sample with large magnet

No positive result having been obtained to this point, it was decided to increase the magnetizing field at the sample. A large piece of Fe (20mm x 20mm x 1mm, 99.999% purity) [18] was positioned in front of a neodymium N42 magnet of the same size. In principle the size of the sample and magnet would be large enough to ensure field uniformity over the cross section of the beam, thus avoiding the deflection of positrons. Data collection runs were discarded if they were inconsistent (i.e. difference in the spectrum for the same direction of magnetization), Figure 36, and consistent runs have been collectively compared (Figure 37).

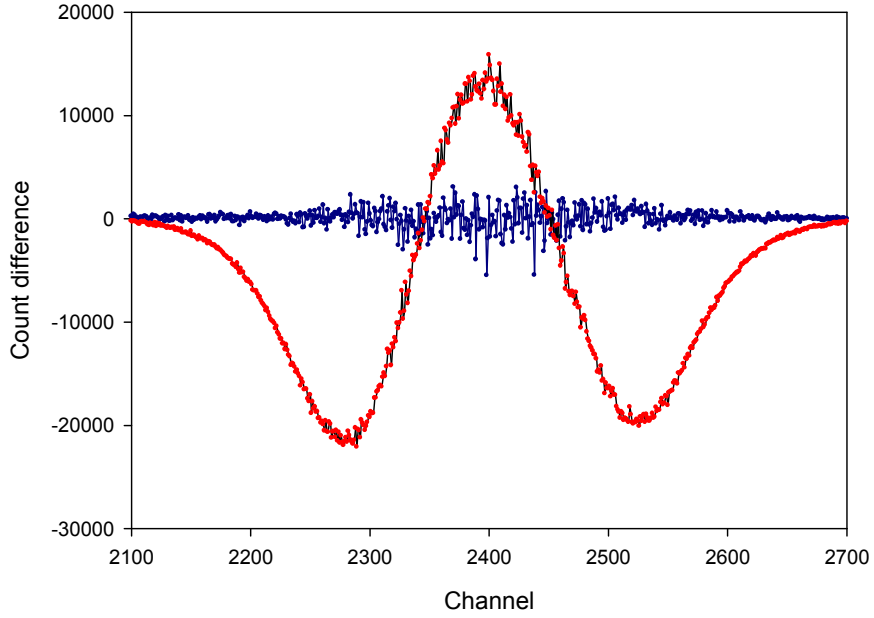

Figure 36: Two consistent runs (blue) and two inconsistent runs (red) for the same direction of magnetization (G). There are 18.8eV per channel and channel 2399 corresponds to the 511keV peak.

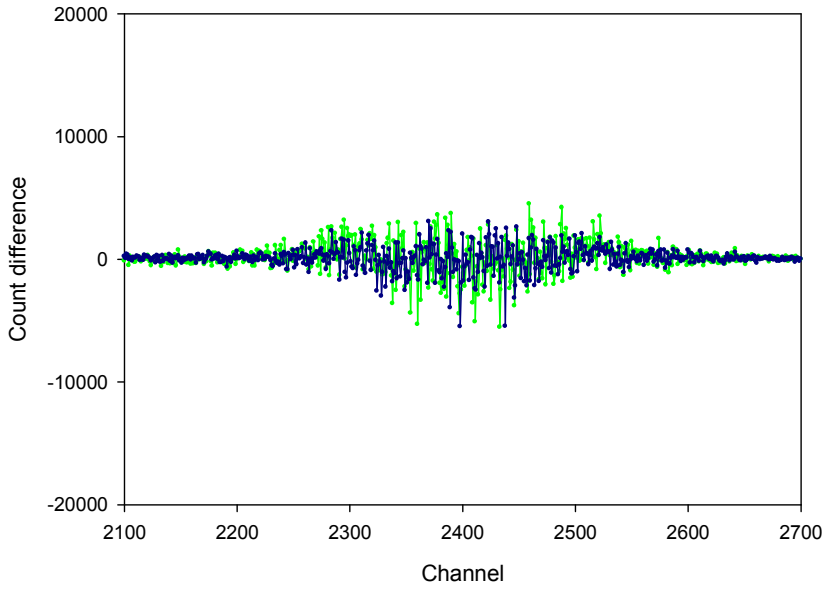

Figure 37: Consistent runs for G and R directions (blue) and G only (green). There are 18.8eV per channel and channel 2399 corresponds to the 511keV peak.

The same measurements were carried out for mu-metal, an alloy with a magnetic susceptibility much greater than Fe (Figure 38). For stability measurements, the mu-metal was simply covered by a thin aluminium foil (Figure 39).

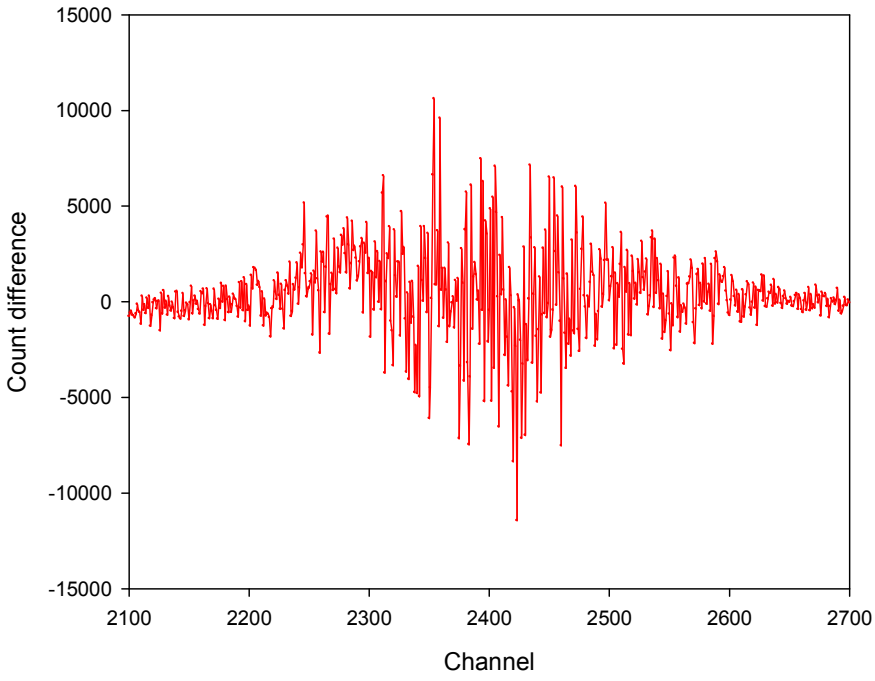

Figure 38: Difference in gamma ray counts between the G and R field directions for mu-metal in front of a N42 magnet. There are 18.8eV per channel and channel 2399 corresponds to the 511keV peak.

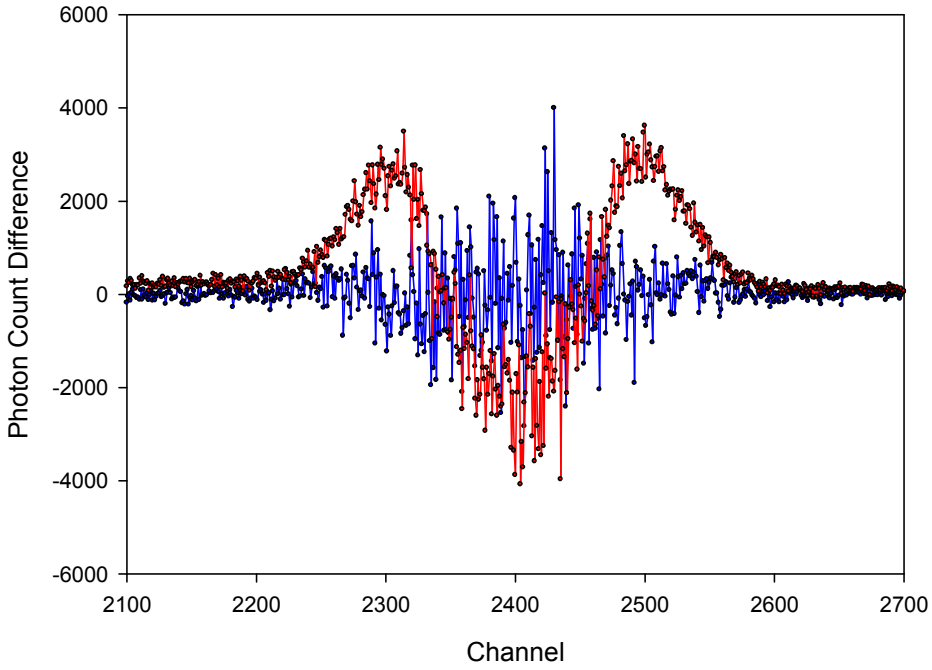

Figure 39: Difference in gamma ray spectra for Al foil on a mu-metal film and a N42 magnet. The difference should be zero (blue) as Al is non magnetic, but a shifted/false result is also shown (red). There are 18.8eV per channel and channel 2399 corresponds to the 511keV peak.

The results showed that the system continued to produce inconsistent results, most likely due to the electronic components rather than the experimental setup itself, which may be overcome by taking a larger number of shorter measurements, removing the ones that are conflicting and adding the rest together. Following this procedure, no significant response was recorded for Fe and mu-metal when the direction of the magnetization was reversed, implying that the effect was too small to be observed with the current setup. In order to maximize the possibility of recording a measurable response, the beam and sample polarization should be maximized. Metals and alloys like iron and mu-metal have copious numbers of free carrier electrons at room temperature. These electrons, along with lattice imperfections in the samples, dominate the positron annihilation response. However, we next consider the steps taken to maximize the beam polarization.

New Na-22 Source

A Na-22 source capsule with a beryllium backing plate was installed (after an 18-month delay) from the suppliers, iThemba Labs, South Africa [20]. This is shown in Figure 40. Positrons emitted in the direction away from the sample are thus almost all absorbed in the beryllium, rather than being efficiently backscattered as they are in a standard capsule (by a tantalum backing plate) [21]. Therefore mostly forward emitted positrons with a forward polarization (positrons have a polarization in their

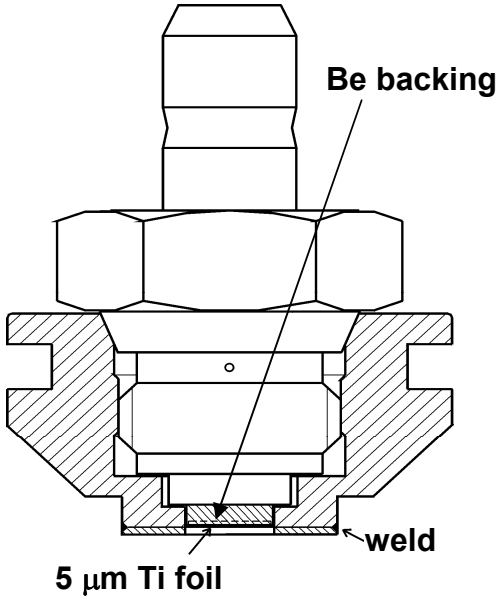

Figure 40: Na-22 source capsule showing replacement Be (low-Z) backing plate. Scale: 1:4.

direction of emission) stroke the moderator and form the beam.

Also, positrons emitted with a higher energy suffer less depolarization on interacting with moderating materials. Consequently, a 25μm thick beryllium film was placed in front of the source capsule (figure 41) to slow down faster positrons before the moderator. The disadvantage of this is that the annihilation count rate is dramatically decreased, but the foil thickness was chosen as a compromise between polarization and beam intensity, following the observations of Van House and Zitzewitz [1].

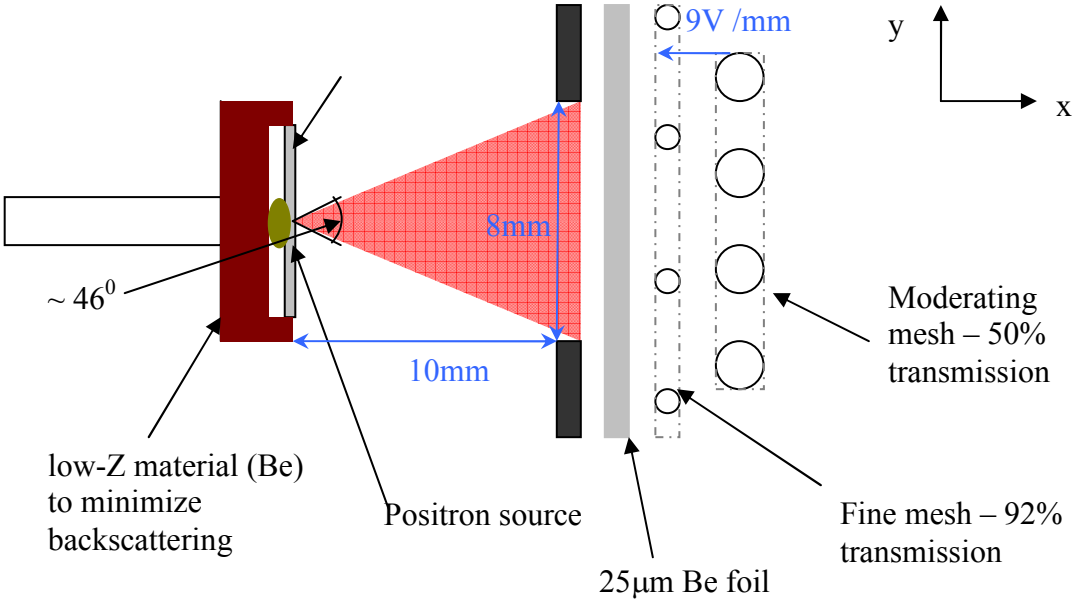

Figure 41: Be-backed source with a thin Be absorber in place.

The annihilation count rate of the new source in a typical arrangement (i.e., positioned close to the moderator mesh and with Ta backing) is of the order of 3000/s and in the new setup, shown in Figure 41 above, it is of the order of 70-80/s. This greatly affects the signal to noise ratio of the measurements, requiring much longer data collection times.

Measurements were again taken on the large iron sample with the new source arrangement, with no significant result, as shown on figure 42. In these measurements the total positron count rate was similar for both directions of guiding magnetic field.

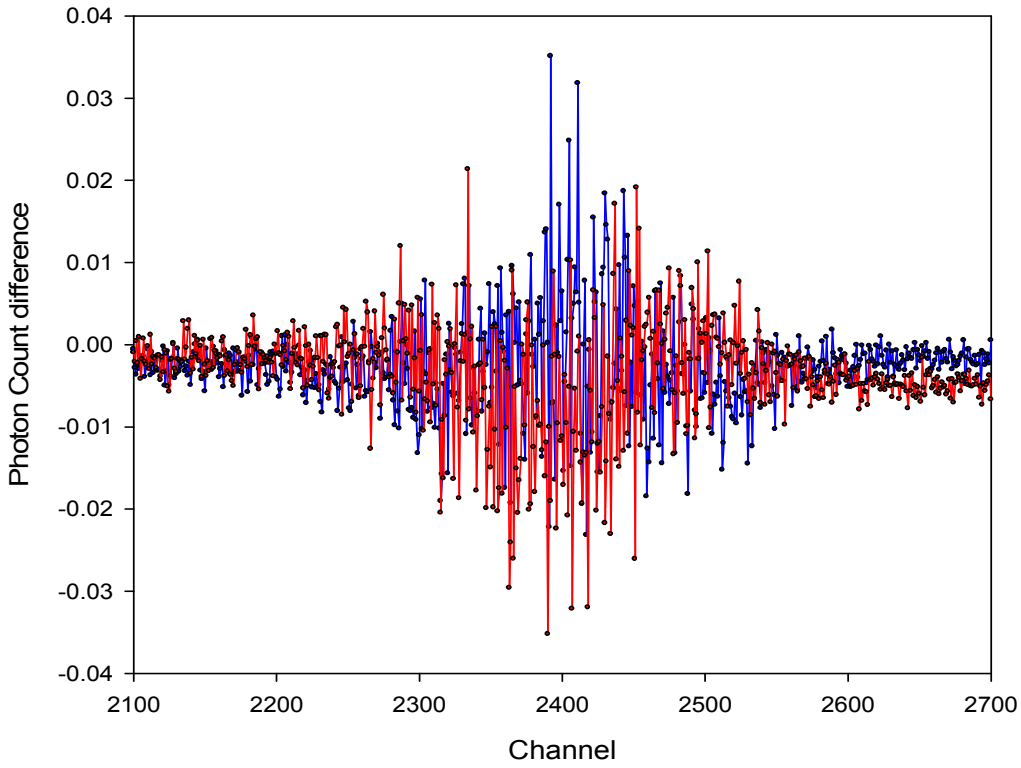

Figure 42: Large Fe sample spectrum difference with a N42 magnet using the Be-backed source with the thin Be absorber foil, showing no change between the same direction of magnetization (red) as expected, and different direction of magnetization (blue). There are 18.8eV per channel and channel 2399 corresponds to the 511keV peak.

Measurements on solid oxygen films

The most likely reason for measuring this null result would be that vacancies in the sample might not be trapping positrons, thus not allowing them to 'see' the spin- polarizable 3d electrons.

Oxygen's magnetic properties are well- established [22]. In its solid form (α phase) it is a crystalline, anti-ferromagnetic material with no conducting electrons, making it an appealing material for a polarized positron measurement despite its low magnetic susceptibility [22].

The samples were grown on situ, on a copper cold finger, by introducing pure oxygen into the vacuum chamber. The oxygen pressure in the chamber was relatively high (10^{-5} Torr) to ensure a high purity of the grown solid (vacuum pressure 10^{-8} Torr). The sample was grown thick enough so that positrons at 30keV are deposited purely in oxygen. This was to ensure that any air growing on top of the sample during

the measurement has no effect. The rate of growth of air has been investigated and is shown below (figure 43).

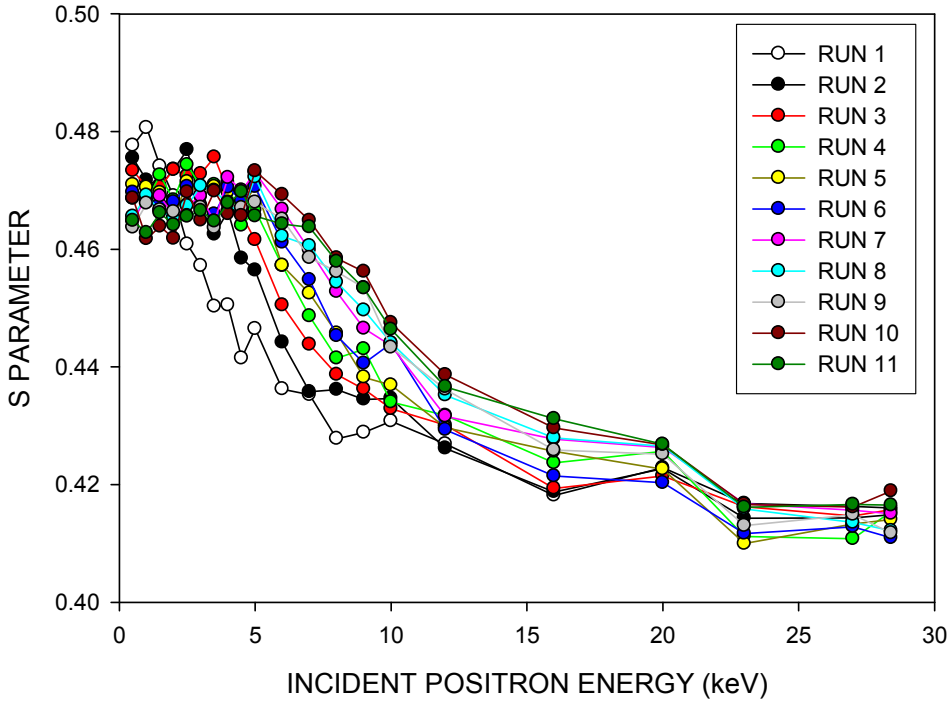

Figure 43: The growth of solid oxygen on a cold finger by the ambient pressure in the vacuum chamber at 17K.

From this we can see that the oxygen samples can not be grown thick enough to measure at 30keV. Therefore measurements should be made in a thin film and quick enough so that grown air on top does not affect our results. The samples were grown for each field direction and the difference in the spectra is shown below (Figure 44). The guiding field was used to magnetize the sample in G and R directions. The stability of the system was tested by checking for differences between two different G measurements and also between two R measurements.

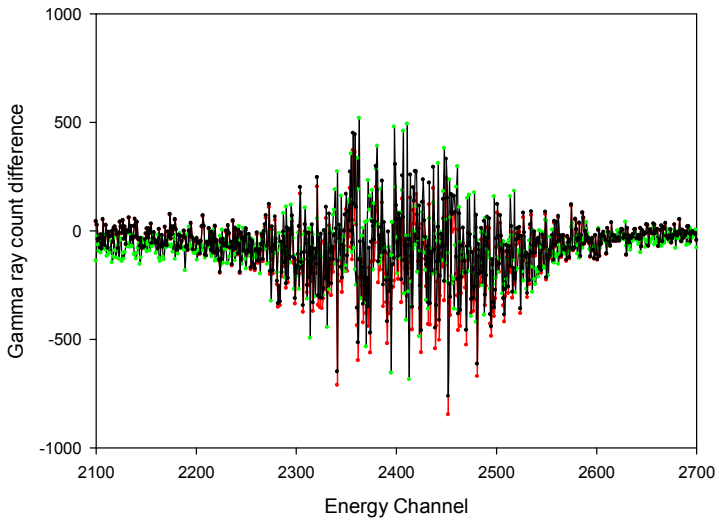

Figure 44: Difference in spectra between measurements of the same magnetization (G-G and R-R) and of different (G-R) for a solid oxygen film. There are 18.8eV per channel and channel 2399 corresponds to the 511keV peak.

The results again showed no observable effect, and it was concluded that the magnetization of the film was probably too low. Increasing the magnetization by growing the oxygen on a magnet meant that a different sample would be used for the two field directions since it would be required to pressurize the vacuum chamber and flip the magnet. Nevertheless, this was attempted to see if two different samples would produce the same response given the same magnetization (Figure 45).

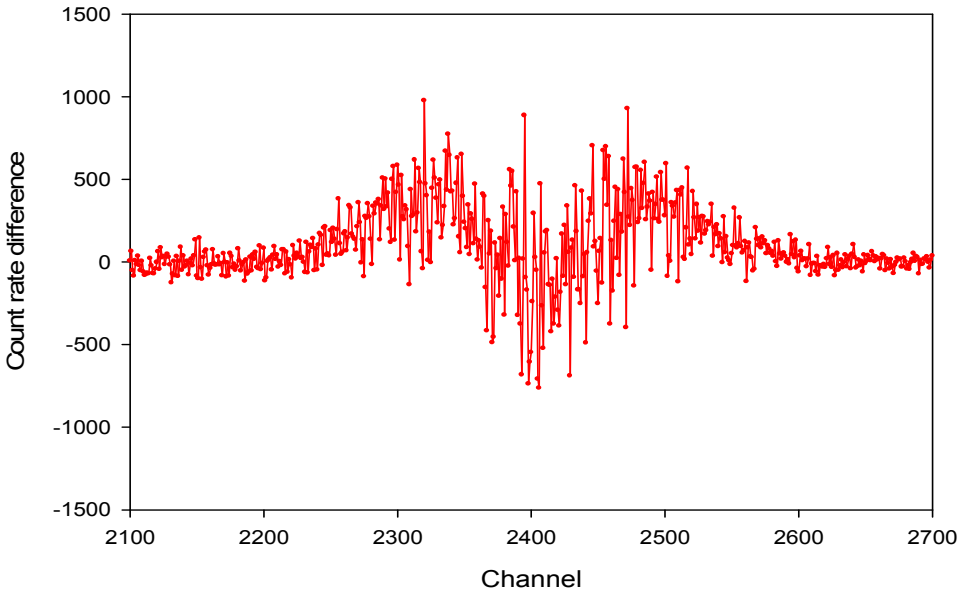

Figure 45: Difference between spectra for two different oxygen samples both in G field, grown under the same conditions. There are 18.8eV per channel and channel 2399 corresponds to the 511keV peak.

This meant unfortunately that oxygen measurements under the influence of a stronger magnetic field were not possible with the current equipment.

Measurements on single-crystal iron

A 10mm-diameter single crystal Fe sample was then installed, and the results for the peak-to-valley ratio are shown below in Figure 46.

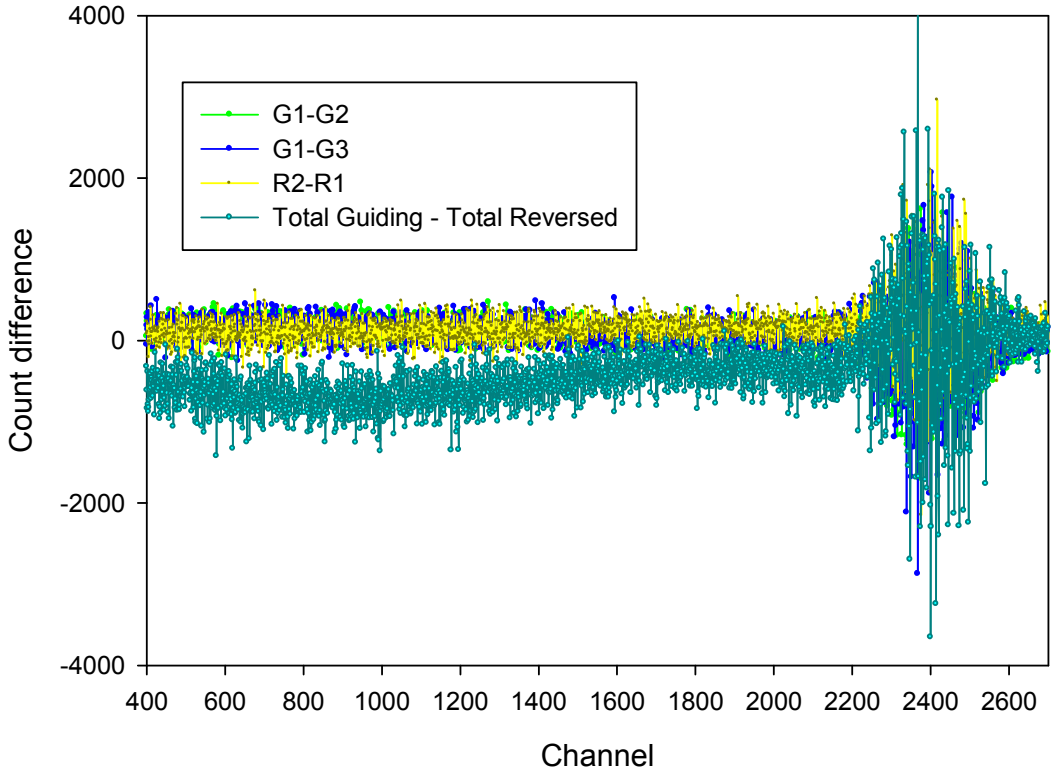

Figure 46: Peak and Valley difference in counts for single crystal Fe between G and R fields. There are 18.8eV per channel and channel 2399 corresponds to the 511keV peak.

There was no apparent difference in gamma ray counts around the photo peak between the two directions of magnetization but, interestingly enough, there was an obvious difference in the valley region to the left of the peak (Figure 46). The valley mainly consists of true background (from cosmic rays, laboratory background radiation, etc), peak-related 'noise' (from incomplete charge collection in the germanium crystal), and real three gamma annihilations of positrons and of the positron-electron bound state, positronium. These three gamma annihilations correspond to the spin triplet state of a positron-electron pair. In order to investigate

whether this background difference reflected a real change in the number of three-gamma positron annihilation events, the true background has to be measured, normalised and subtracted from the individual measurements, as shown in figure 47.

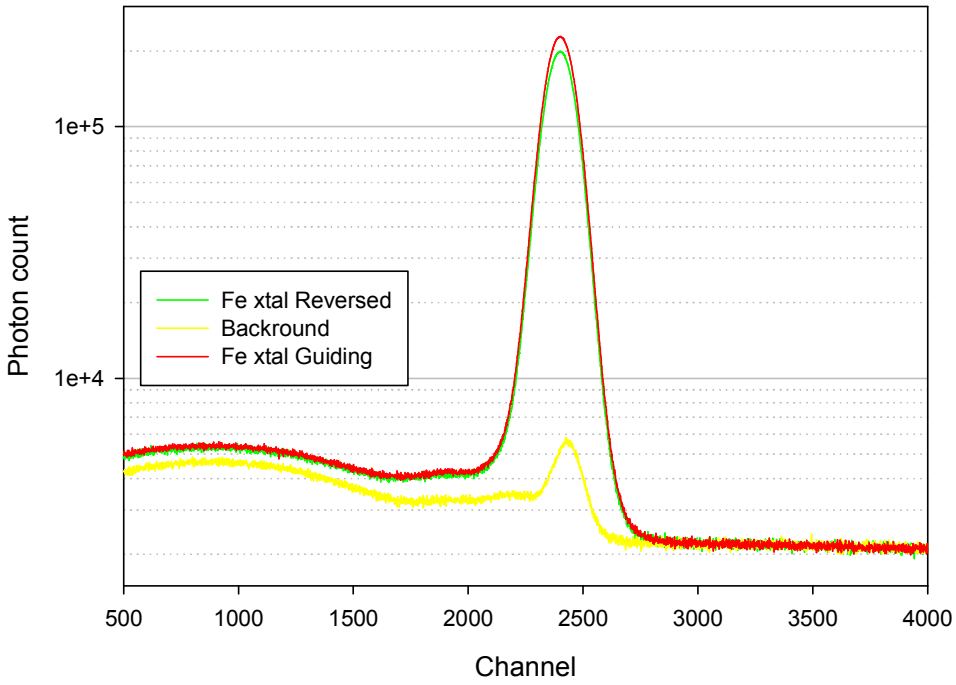

Figure 47: G and R measurements for a single crystal Fe sample, with background normalized. There are 18.8eV per channel and channel 2399 corresponds to the 511keV peak.

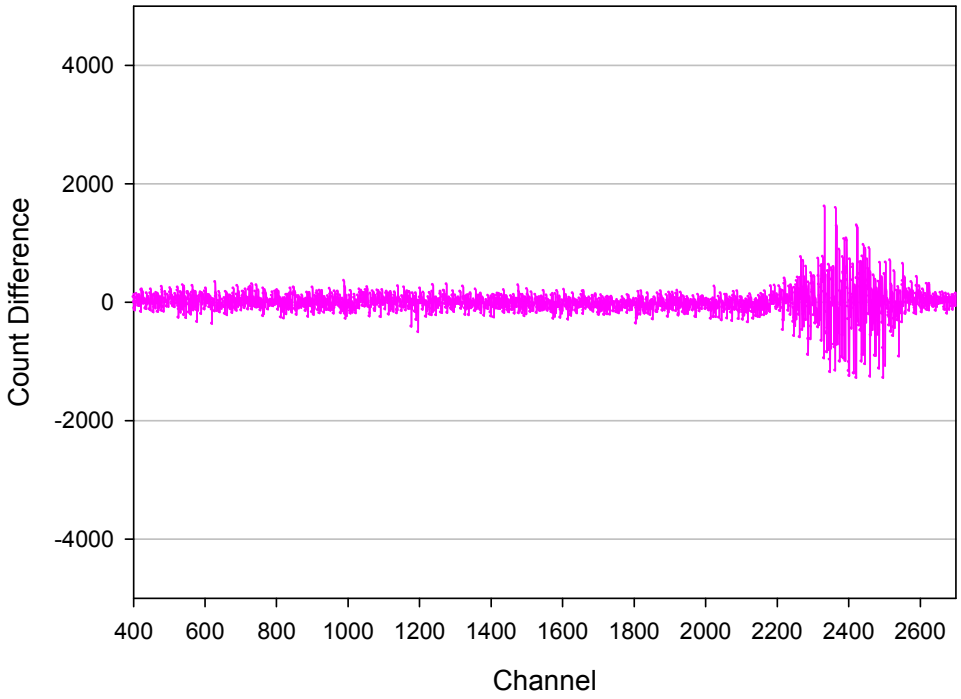

Figure 48: G-R spectrum difference for peak and valley areas of single crystal Fe after background reduction. There are 18.8eV per channel and channel 2399 corresponds to the 511keV peak.

This demonstrates the effect the unwanted background has on measurements with low count rates.

A magnet was then positioned behind the single crystal iron sample. Sample positioning was difficult due to its small size. Shorter and more frequent measurements were made with fields in the G and R directions, the magnet being aligned to each field direction, and checked for consistency. Any contradictory measurements were discarded and the ones in agreement added up for better statistics. An initial comparison of a sum of measurements is shown below Figure 49.

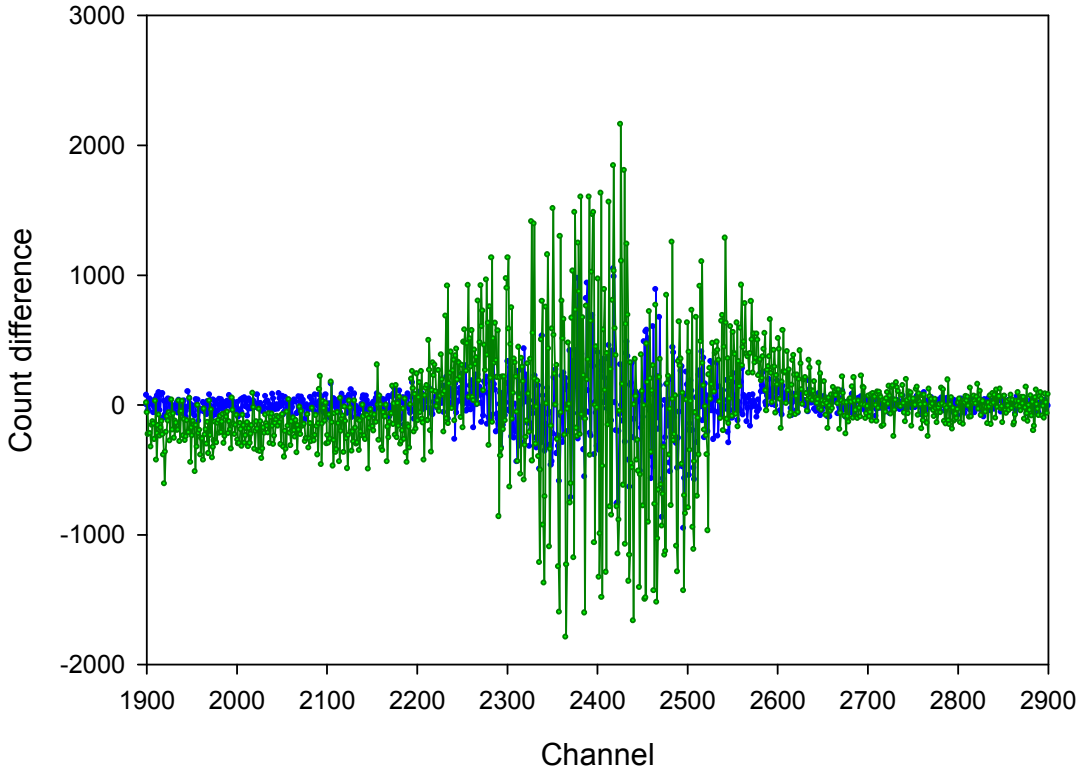

Figure 49: Single crystal iron magnetization effect with the presence of a magnet. There are 18.8eV per channel and channel 2399 corresponds to the 511keV peak.

The same measurements were taken for a non-magnetic sample to ensure the system was giving a true result. The single crystal sample was wrapped in thin alluminium foil and positioned exactly as it was before. This would ensure the magnetic field lines near the sample were exactly the same in both cases, keeping the beam optics the same. This is shown below in figure 50.

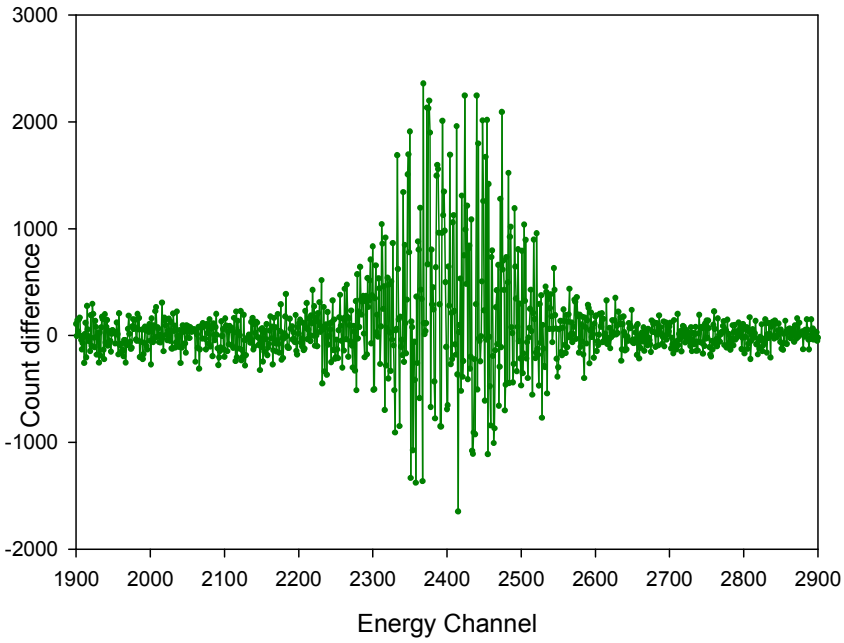

Figure 50: Single crystal iron covered with a thin Al film magnetization effect with the presence of a magnet. There are 18.8eV per channel and channel 2399 corresponds to the 511keV peak.

These results were encouraging and lead us to believe the difference seen on the single crystal iron was real. However the observed results had to be compared with the expected, modelled results. The results provided by Dr Stephen Dugdale [9] have been added in 10's, convoluted with the resolution of the detector and compared with the results observed in figure 49. This comparison is shown in figure 51.

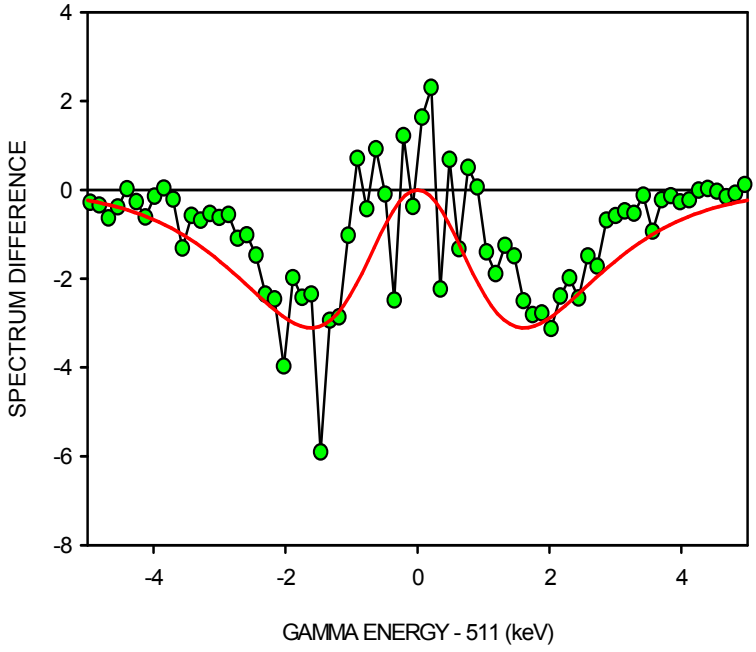

Figure 51: Magnetisation effect observed for single crystal iron – green circles (smoothed), compared to the modelled data by Dugdale [9] – red line (convoluted).

2.4 Conclusions

As seen from figure 51, the observed results fit the expected results very well. It is therefore reasonable to comment that the observed magnetic effect is real and that the polarised positron beam has been successful in responding to spin-polarised electrons in the sample. However, it is worth emphasising the difficulties and limitations of this process. There were major problems associated with competing trapping sites within the sample, and technical difficulties in sufficiently magnetising the sample without disrupting the beam. The low beam intensity meant that he time required for measurements in order to see an effect was very long - a few weeks- meant that measures had to be taken to combat systematic drifts and shifts. Stronger radioactive sources with higher positron count rates (without compromising the polarisation of the beam) would be beneficial, although somewhat dangerous. Strong electromagnets to magnetise the samples (most of which will have a considerably smaller magnetic susceptibility than iron) would also be desirable. However, the indications from the measurements described in this chapter are that measurements of thin magnetic samples using a positron beam will be a considerable challenge for future researchers.

CHAPTER 2 REFERENCES

[1] Igor Žutić and Jaroslav Fabian, "Spintronics: Silicon twists", Nature **447**, 268 (2007).

[2] P.W. Zitzewitz, J.C. Van House, A. Rich, D. W. Gidley, "Spin Polarization of Low-Energy Positron Beams", Physical Review Letters **43**, 1281 (1979)

[3] D.W. *Gidley*, A. Kaymen, T.W. Capehart, "Spin Polarised Positron Beams and their applications", Phys. Rev. Lett. **4**, 1779 (1982).

[4] S. C. Pevovar, M. H. Weber, and K. G. Lynn, "Ratio of positron annihilation into three photons versus two", Phys. Stat. Solidi **4**, 3447 (2007).

[5] R.W. Siegel, "Positron Annihilation Spectroscopy", Ann. Rev. Mat. Sci. **10**, 393-425 (1980).

[6] W. Wernsdorfer, K. Hasselbach, D. Mailly, B. Barbara, A. Benoit, L. Thomas, G. Suran, "DC-SQUID magnetization measurements of single magnetic particles", J. Mag. Magnet. Materials **145**, 33 (1995).

[7] D.J. Griffiths, "Introduction to Electrodynamics" 3rd edition, (Cummings,1999).

[8] G. J. Johanson, M. B. McGirr, D. A. Wheeler, "Determination of the Néel temperature of face-centered-cubic iron", Phys. Rev. B **1**, 3208 (1970).

[9] S.B. Dugdale, University of Bristol (private communication, 2008).

[10] T. Torsti, M. Heiskanen, M. J. Puska, R. M. Nieminen, *et al*, "MIKA – a multigrid-based program package for electronic structure calculations", Int. J. Quantum Chemistry, **91**, 171 (2003).

[11] http://www.csc.fi/physics/mika/

[12] W. D. McGlinn, "Annihilation of Polarised Positrons in Magnetised Iron", Il Nuovo Cimento, **22**, 225 (1961).

[13] http://e-magnetsuk.com/

[14] H. Danan, A. Herr, A. J. P. Meyer, "New Determinations of the Saturation Magnetization of Nickel and Iron", J. Appl. Phys. **39**, 669 (1968).

[15] Lorne A. Page, Milton Heinberg, "Measurement of the Longitudinal Polarization of Positrons Emitted by Sodium-22", Phys. Rev **106**, 1220 (1959).

[16] Z. Chaoui, N. Bouarissa, "Positron and electron backscattering from elemental solids in the 1-10keV energy range", J.Phys C: Condens. Matter **16**, 799 (2004).

[17] J Major, in Positron Beams and their Applications, PG Coleman (editor), (World Scientific, 2000), p. 259.

[18] J.B. Calvert, in http://mysite.du.edu/~jcalvert/phys/iron.htm (2003).
[19] S.M. Hutchins, P.G. Coleman and R.N. West, "A Low-Distortion Slow Positron Filter", J. Phys. E **19**, 282 (1986).
[20] iThemba labs - website: http://www.tlabs.ac.za/
[21] P.G. Coleman, L. Albrecht, A.B. Walker and K.O. Jensen, "Positron Backscattering from Elemental Solids" J. Phys. Condens. Matter **4**, 10311 (1992).
[22] Peter W. Stephens, C. F. Majkrzak, “Magnetic structure and dynamics in the alpha and beta phases of solid oxygen”, Phys. Rev. B **33**, 1 (1986).

CHAPTER 3: POSITRON ANNIHILATION SPECTROSCOPY OF STATE TRANSITIONS IN SOLID WATER

3.1 Introduction to Amorphous Solid Water and Crystalline Water Ice

Water is a substance that has attracted much interest by a range of research fields. It is considered to be the base for life and has some very intriguing and unusual properties. Its solid phase alone has fifteen different phases, ranging from amorphous to crystalline (cubic – I_c – and hexagonal – I_h) and of many different atomic arrangements and densities. This chapter aims to study near surface solid water in its most abundant states in the universe; Amorphous Solid Water (ASW) and I_c and I_h. These states are described further on in detail. VEPAS seems to be a suitable technique for these experiments as it is done in high vacuum (like space) and the samples can be grown on situ under a controlled environment.

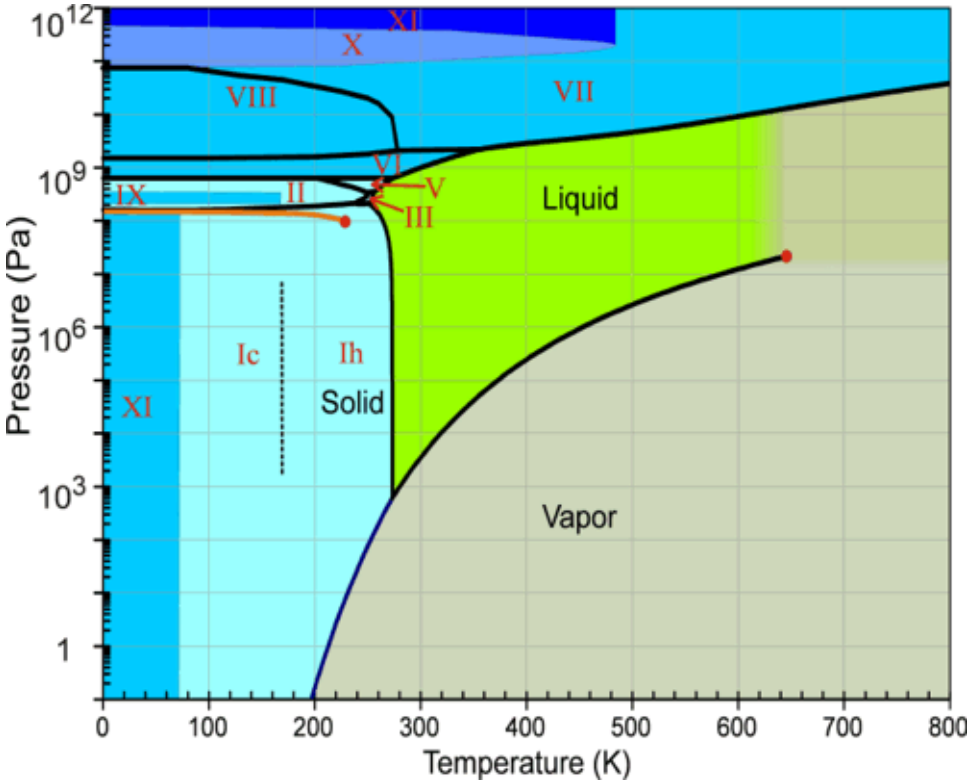

Figure 1: Phase Diagram of Water, showing its Liquid, Vapour and numerous solid states. Amorphous states of Ice are not shown, but can exist under the same conditions as crystalline phases of ice (i.e. Ice XI, I_c and I_h). [1]

Ice I_h is a crystalline form of solid water. It is the form of ice mostly found on the planet, (with the exception only of a small amount of ice I_c). It is characterised by its atomic arrangement; in a hexagonal pattern. As seen on figure 1, it can exist down to 73K but other forms of ice can exist at those temperatures as well. I_h is very stable and can not be easily transformed once it has formed

Ice I_c is another crystalline form of solid water. It too is described by its atomic arrangement; in a cubic pattern. It can exist in similar conditions as I_h but it is metastable. This means that once transformed to I_h it can not transform back to I_c. The transformation can be triggered by a rise in temperature usually at ~170K.

Amorphous ice is as stated by the name, an amorphous solid form of water, defined by its lack of any long range order in its atomic arrangement. There are many different states of amorphous ice, described below.

Low-density amorphous ice is a form of amorphous ice. It has a density lower than other forms of amorphous solid water (i.e. 0.94g/cm^3). It is thought to be the form of ice that exists on celestial bodies and dust particles in space. It can be produced by rapidly cooling liquid or gas water on smooth metallic surfaces. The rate of cooling is crucial to the growth of this form of ice. If water molecules are not cooled fast enough, crystalline structure will be allowed to form.

High-density amorphous ice is another form of amorphous ice that can exist at high pressures and low temperatures. It can be formed by a number of ways, compressing low density amorphous ice, compressing I_h or compressing I_c. As denoted by its name, this is a higher density form of amorphous ice of 1.17 g/cm^3 [2,3].

Very-high-density amorphous ice, was discovered in 1996 by Mishima [4]. He warmed high density amorphous ice while keeping the pressure high and observed that the density increased to 1.26 g/cm^3.

Positronium fraction measurements

Positronium [5,6], the bound state of an electron and a positron, is a stable state which can exist in vacuum for a mean time of 142ns in its triplet state (ortho-Ps, decaying naturally into three gamma rays) and 125ps in its singlet state (para-Ps, decaying naturally into two gamma rays). Positronium forms in open spaces like pores or vacancies, and the larger the open space, the more likely the positronium will annihilate as such rather than with another nearby electron. The two to three gamma annihilation ratio of isolated positronium atoms is 1:3 [7] but differs if in open spaces inside a material. The two to three gamma *positron* annihilation ratio is very different than that of positronium, e.g. for Si 347:1 [7]. There is therefore a noticeable increase in three gamma annihilation events when significant amounts of positronium are formed. Three-gamma ortho-Ps annihilations are therefore very useful when studying porous or damaged materials and can provide further information about their structure.

A parameter to denote the positronium decay fraction is usually used - the P:V ratio, or Peak to Valley ratio. It is defined as the ratio of annihilations of the peak, i.e. the 511keV and their Doppler shifted related annihilations, to all the annihilations with much lower energy to the left side of the peak. The peak of the spectrum is defined as the counts registered between the channels 2028 to 2771 which correspond to energies of 504keV to 518keV respectively. The valley is defined by the channels 250 to 2028 which correspond to energies of 471keV to 504keV respectively. The energy per channel is 18.8 eV. Gamma photons detected with significantly lower energy than the 511keV photo peak are associated with three gamma annihilations. P:V is a relative parameter and can only be meaningful in comparison with a reference value, i.e. in the bulk of a material, or a reference material that will always have the same value. It is also useful to note that metals are considered to have a P:V value in their bulk related to zero positronium formation.

3.2. Positron and Positronium Annihilation Spectroscopy study of Structural and Phase Transitions in Solid Water – Experiments

The evolution and annealing of pores in, and the crystallization of, vapour-deposited films of Amorphous Solid Water (ASW) have been studied using variable

energy positron annihilation spectroscopy for temperatures in the range 50-180K. The range of temperatures is defined by the growth of films of air and/or hydrocarbon impurities in vacuum at temperatures <50K, and very fast sublimation at temperatures >150K. Both positron and positronium annihilation provide an insight to the nature of the grown-in pores and their evolution with temperature.

ASW films were grown from a diffuse water vapour background flux on to a copper cylinder block, cooled by a closed-cycle He cryostat to 50K-180K, following the recipe described in ref.[8](Fig. 2). The water vapour was leaked into the sample chamber via a needle valve from a side chamber containing de-ionized water initially subjected to several freeze–pump–thaw cycles [9]. The sample temperature was controlled by a calibrated silicon-diode sensor and measured by a *K*-type thermocouple clamped on the sample holder to an accuracy of ±1 K. The ASW samples were grown at rates between 5 and 200nm min^{-1} and their thicknesses were thereby controllable. [10] The growth rates were determined by measuring the film thickness from the VEPAS *S* vs *E* plots, knowing the growth time.

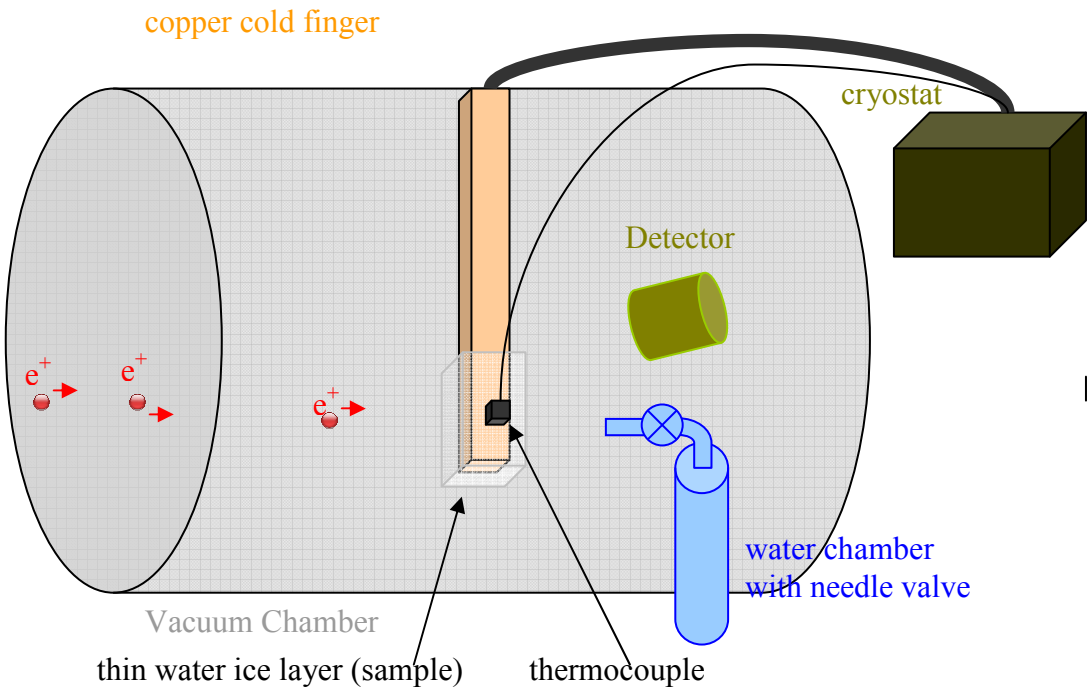

Figure 2: A simple representation of the system setup showing any major differences from the conventional VEPAS set-up.

A number of samples were grown under different initial conditions. The controlled variables for sample growth were the base pressure of water vapour, the growth temperature, and the growth time. All three variables affected the thickness of the sample:

Sample A: grown at 50K 10^{-6} Torr for 120 minutes ~500nm

Sample B: grown at 50K 10^{-5} Torr for 10 minutes >9um

Sample C: grown at 50K 10^{-7} Torr for 635 minutes on a crystal ice substrate >9um (including substrate)

Sample D: grown at 120K 10^{-7} Torr (measure while growing)

Sample E: grown at 170K 10^{-5} Torr for 960 minutes >9um

Sample F: grown at 170K 10^{-4} Torr for 960 minutes >9um

Sample G: Grown at 170K 10^{-4} Torr for 960 minutes >9um

3.3.1 Pre Crystallization - Amorphous Solid Water (ASW): Results for samples A,B C and D

Sample A

The evolution of the sample has been studied when heated up from 50K to 150K and then cooled down back to 50K. The *S* parameter, *W* parameter and *P:V* ratio have been recorded. *S(E)* for sample A is shown below (Figure 3).

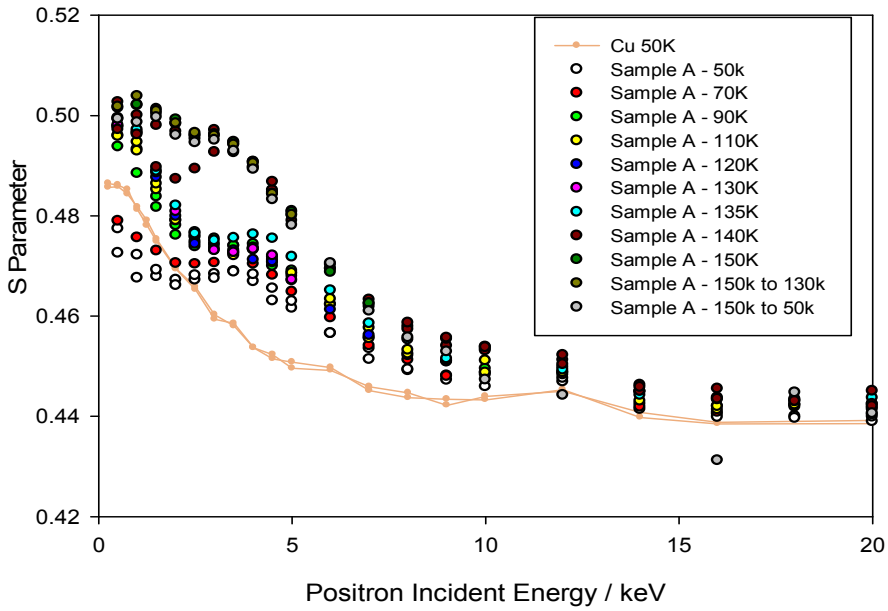

Figure 3: Evolution of *S(E)* for sample A on heating from 50 to 150K and cooling to 50K.

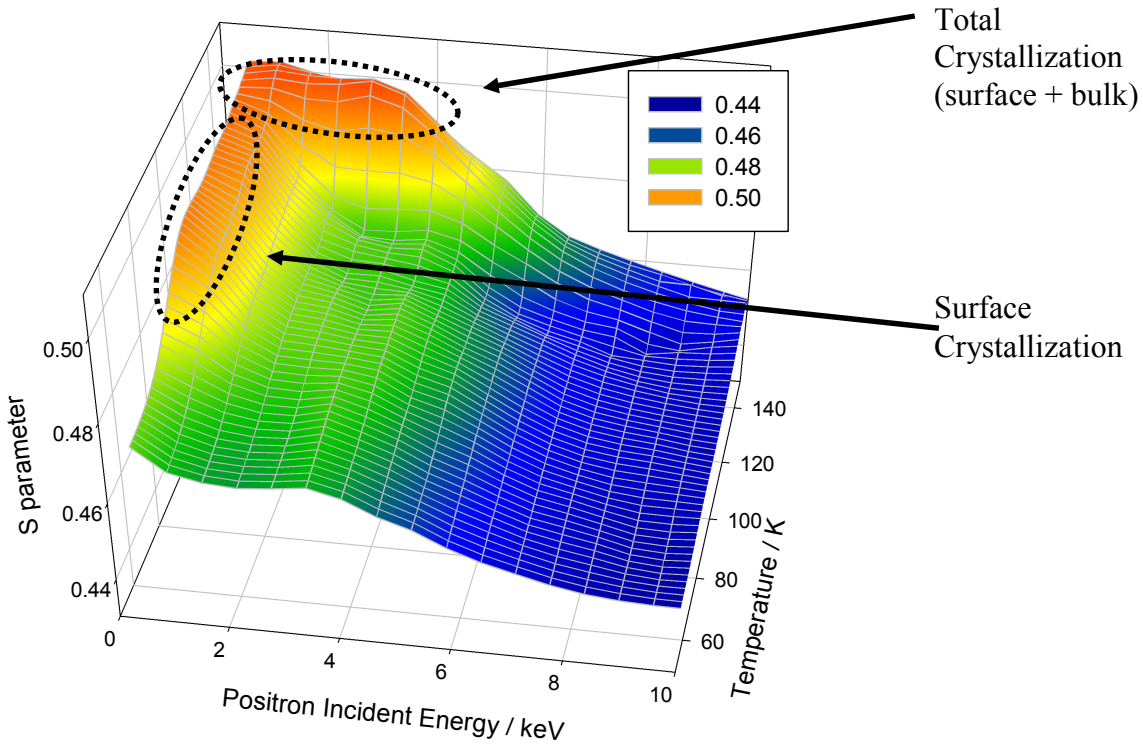

Figure 4: 3D representation of the *S* parameter for sample A as it changes with temperature. The blue end of the spectrum is the substrate (copper cold finger), green is the amorphous solid water and on the red end of the spectrum a crystalline state of solid water.

From Figures 3 and 4 we can see an early surface state change of the sample at a temperature less than that commonly accepted for crystallization (~135K). This is perceived as a near-surface crystallization of the sample most likely because of the higher mobility of the molecules near the surface. The temperature at which this occurs is around 90K.

The *P:V* ratio of the sample is shown in Figure 5 for all temperatures along with a copper reference. The plots are showing some consistent features throughout all the samples which appear to be systematic rather than real. These could be due to the change in count rate between different energies of the positron beam. To counter this, all data are normalised to copper, which should have no positronium in bulk (i.e. *P:V* ~16). The normalised results are shown in Figure 6.

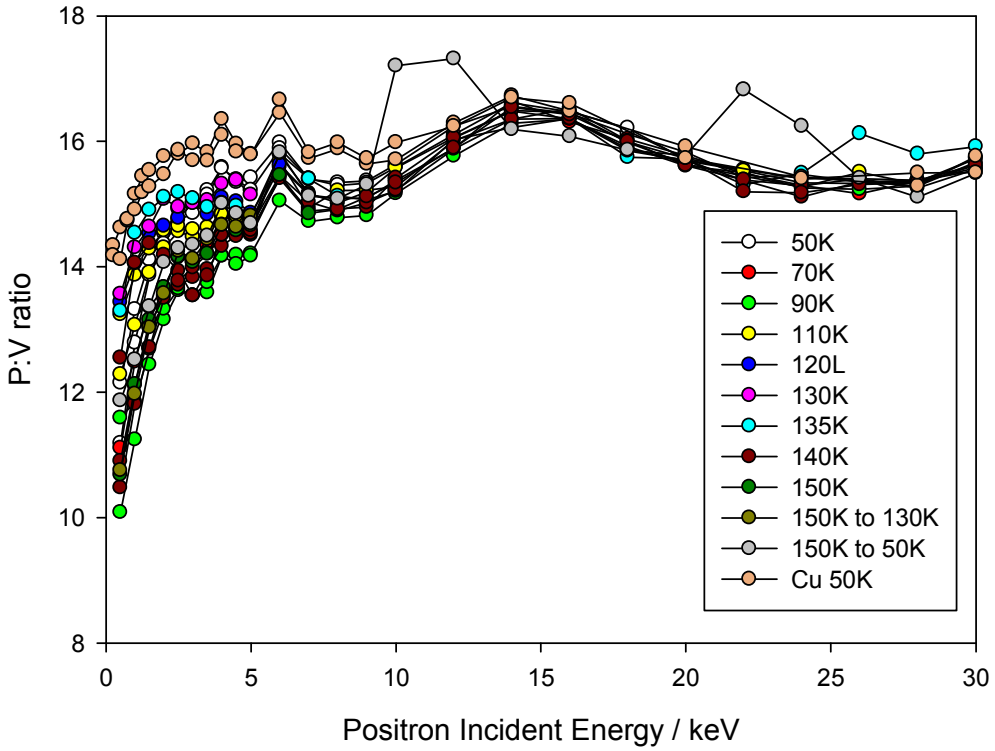

Figure 5 *P:V* ratio raw data for sample A, with systematic features visible

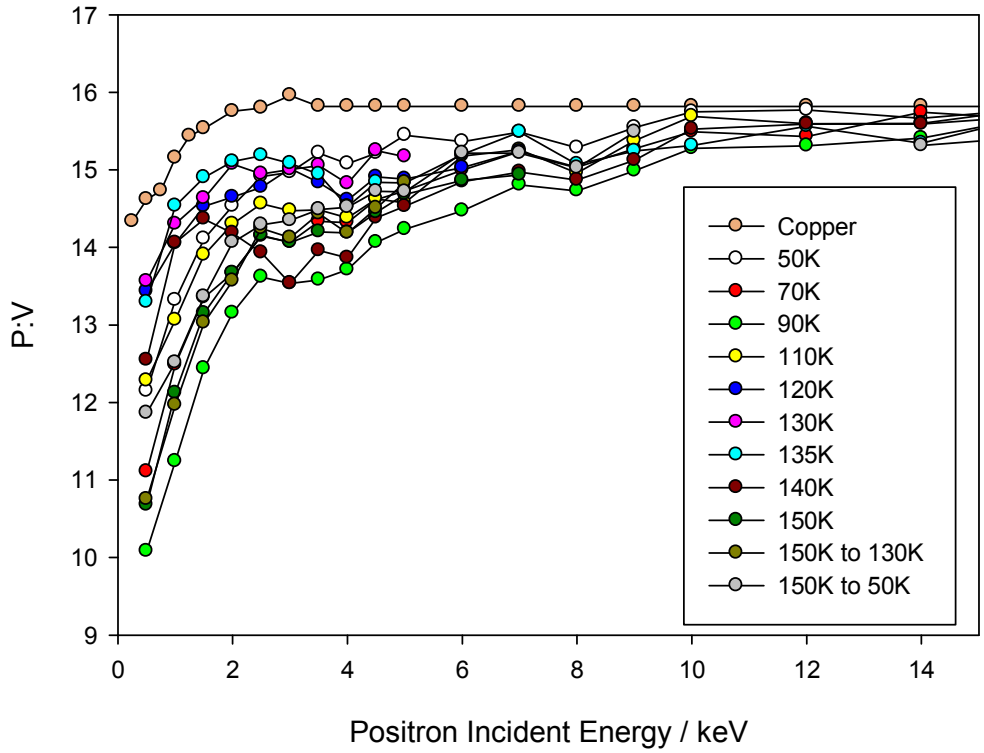

Figure 6: *P:V* for sample A normalised to copper *P:V* for positron incident energies >3.5keV to eliminate any systematic features (copper *P:V* at >3.5keV should theoretically be flat).

From the *P: V* plots above we can see a number of features associated with the evolution of the pore and vacancy structure of the sample. The higher the *P:V*, the smaller the amount of positronium annihilations in the sample, therefore a low *P:V* can indicate the existence of large pores allowing positronium annihilation at that depth and/or interconnected pores allowing diffusion of positrons to the surface to form positronium there. The plateau seen at the bulk of the sample (~3keV) means a saturation of positronium annihilation signal there. The change seen at energies <2keV is a result of the diffusion of positrons to the surface. Following the change with temperature, we can see a drop of *P:V* up to 90K and an increase in diffusion, probably caused by agglomeration of smaller vacancies into larger pores in the bulk and an increase in pore interconnection length towards the surface. For temperatures greater than 90K the *P:V* ratio increases and the diffusion decreases. This can be explained by breaking down of the long interconnected pores and/or sealing them at the surface due to the early crystallization occurring there plus an annealing of pores and vacancies in the bulk of the sample.

Another parameter measured during these runs was the *W* parameter; this parameter is plotted against the *S* parameter (or sometimes the other way round) in what is usually termed an *S-W* plot. This allows us to identify states of the sample when points are clustered together. For sample A the *S-W* plot is shown below in Figure 7 with three states marked. Points between the states indicate fractional annihilation of the positrons between those states; the closer the point to one state, a larger fraction of positrons annihilates there.

The *S-W* plot confirms what is seen in the *S* parameter plot. It shows an early near surface state change, which is the same as the crystallization state of bulk at 135K.This is commonly accepted as the crystallization temperature for solid water [10]. This suggests that the surface state change is consistent with crystallization.

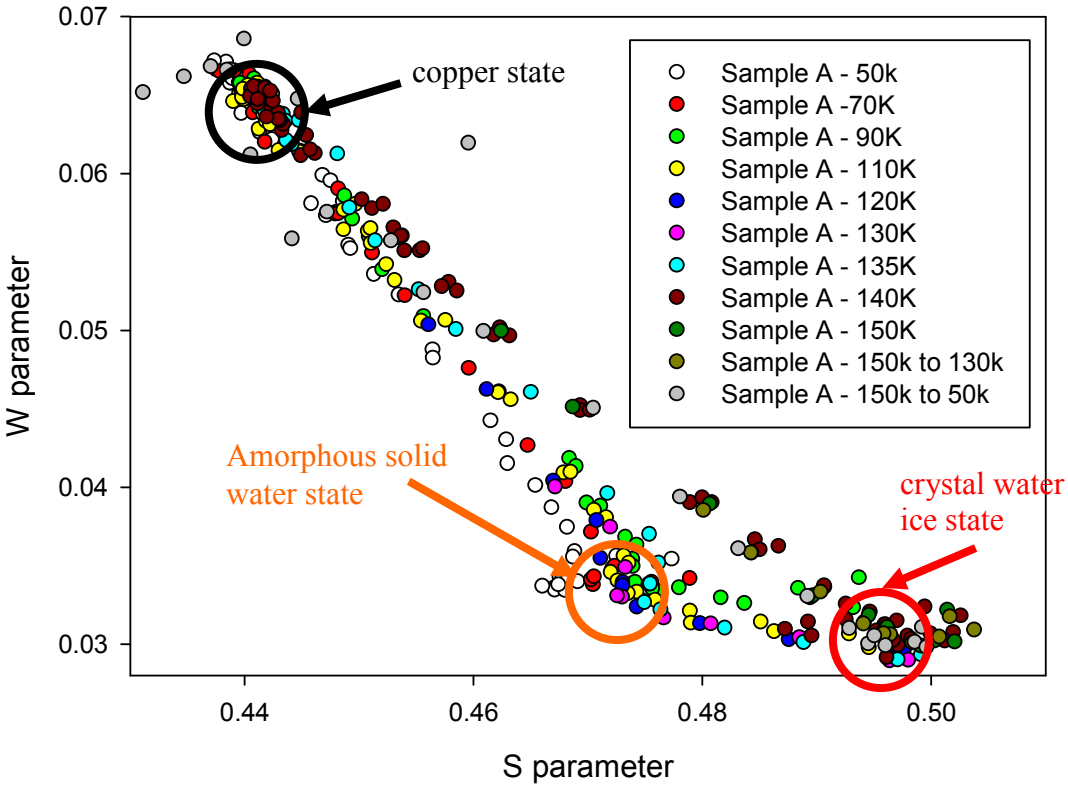

Figure 7: *S-W* plot for sample A, showing 3 distinct states. (Copper state – black circle, Amorphous Solid Water – orange circle, Crystal water ice – red circle). Points on a line between 2 states mean that a fraction of positrons annihilate in one state and some in the other.

Sample B

This sample was grown similarly to sample A but at a higher water vapour base pressure. Although it has been grown for a fraction of the time, it is significantly thicker than sample A. It is expected to have a similar response although with more pores and vacancies present. The *S* parameter and the normalised *P:V* at different temperatures for sample B are shown below in figures 8 and 9 respectively.

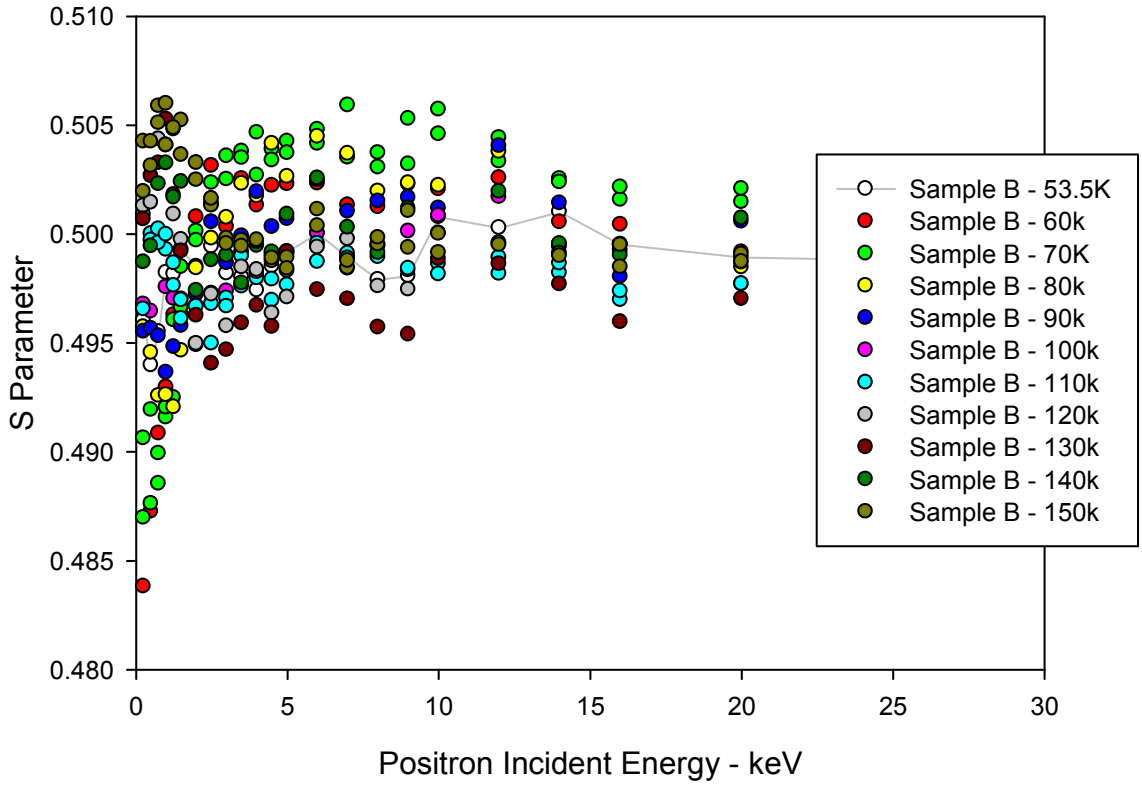

Figure 8: The *S* parameter for sample B for different temperatures

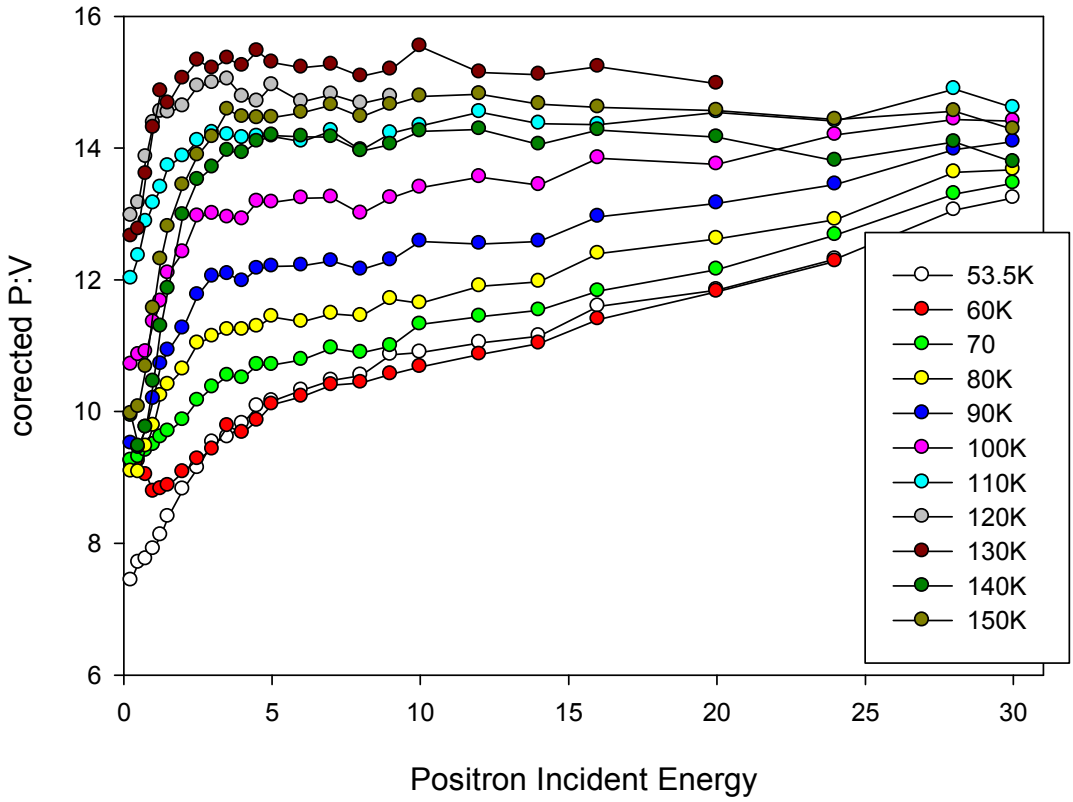

Figure 9: The *P:V* for sample B for different temperatures

Although not so clearly seen, sample B behaves in the same manner as sample A, with an early near surface crystallization. Due to the initial bulk value of the *S* parameter being higher and the initial near surface *S* being lower, the crystallization is harder to see but still observable. The early near-surface crystallization seems to occur at slightly lower temperatures (~ 80K). The different initial *S* parameter can be explained by the different growth of the sample; more pores and vacancies would alter the *S* parameter, in this case increase it. *P:V* shows a much longer diffusion length than sample A - of the order of microns - but decreases as the sample heats up; it also increases with temperature, both explained by a breaking up of long interconnected pores also seen in sample A. The absolute values of the *S* parameter can not be confidently compared for different temperatures as the sample is too thick and no clear copper value is seen for reference (so the data is not normalised). A near-surface "bump" is seen in the *S* parameter at a temperature of 150K; sublimation could account for this.

Furthermore, the sample was held at 150K and observed while it was subliming at positron incident energies of 1, 10 and 30keV. The results are shown in Figures 10 (*S* parameter) and 11 (*P:V* ratio).

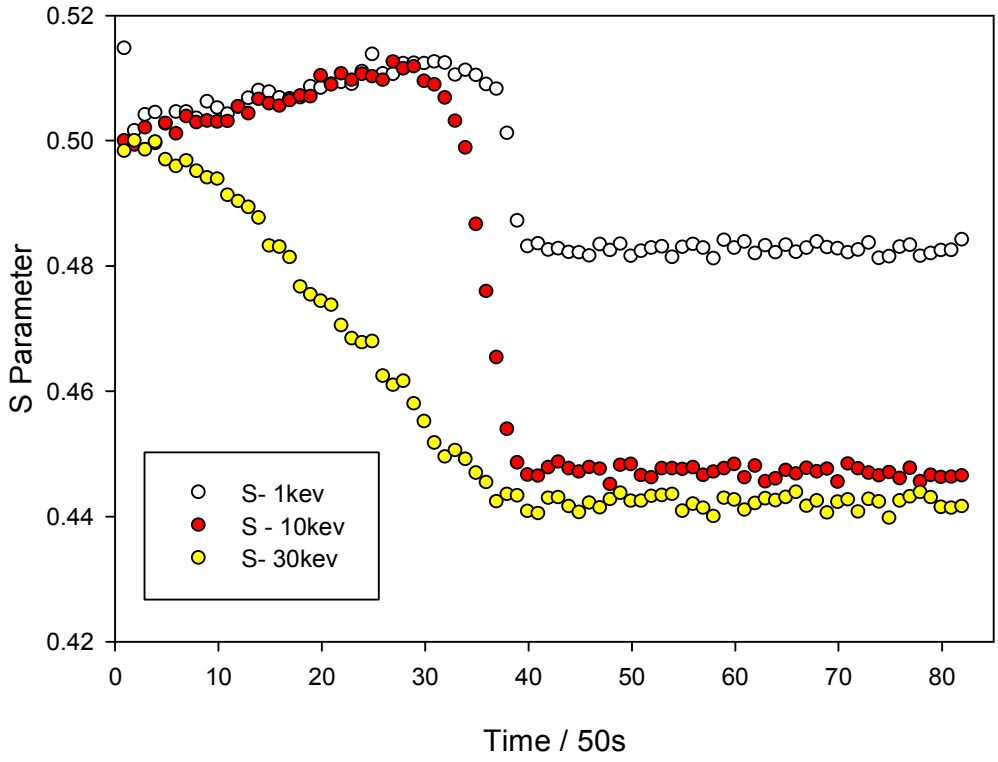

Figure 10: *S* parameter for sample B as it sublimes at 150K for energies of 1, 10 and 30 keV.

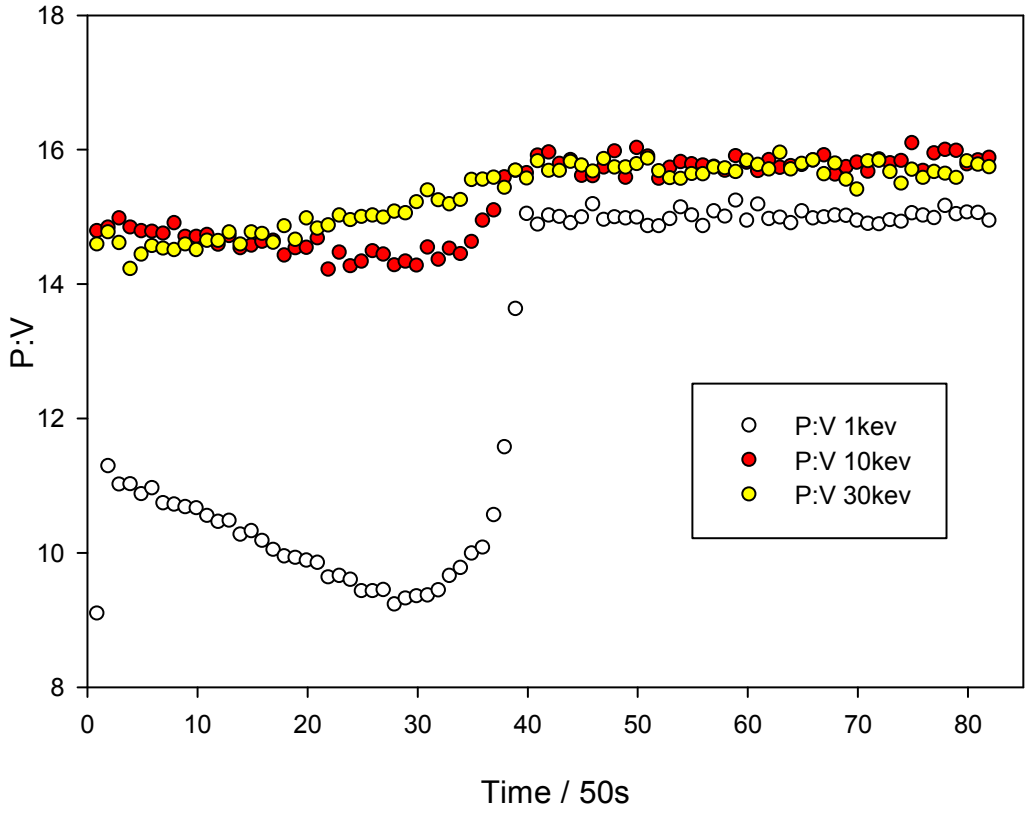

Figure 11: *P:V* for sample B as it sublimes at 150K for energies of 1, 10 and 30keV.

Interestingly, while subliming, *S* increases at both 1 and 10keV (at 30keV *S* decreases with time since more copper is "seen" by the positrons as the ice film gets thinner). *S* then quickly drops to the copper *S* parameter as the sample completely sublimes. Similarly *P:V* decreases as the sample sublimes and then sharply increases to the *P:V* value of copper. The *P:V* change is greater for 1keV than for 10keV suggesting it is due to a change near the surface of the sample. Sublimation occurring throughout the sample would cause little "bubbles" of water vapour being trapped in solid water. These bubbles would mobilise as soon as they reach near surface, coagulating and popping. As a result, the *S* parameter affected by little vacancies (in this case small bubbles) would be the same throughout the sample, changing at the same rate, whereas the positronium would change throughout the sample but at a greater rate near the surface due to the coagulation of these pores and their opening to the vacuum.

Sample C

Sample C is grown similarly to samples A and B but at a much lower water vapour base pressure and instead of being grown straight onto the copper cold finger, it is grown on a previous ice film sample that has been crystallised and cooled down. The growth rate was very slow and required hours to give a significantly thick sample. It is expected to have a more ordered structure than both samples A and B with fewer pores and vacancies. Its *S* parameter and *P:V* ratio are shown below in figures 12 and 13 respectively.

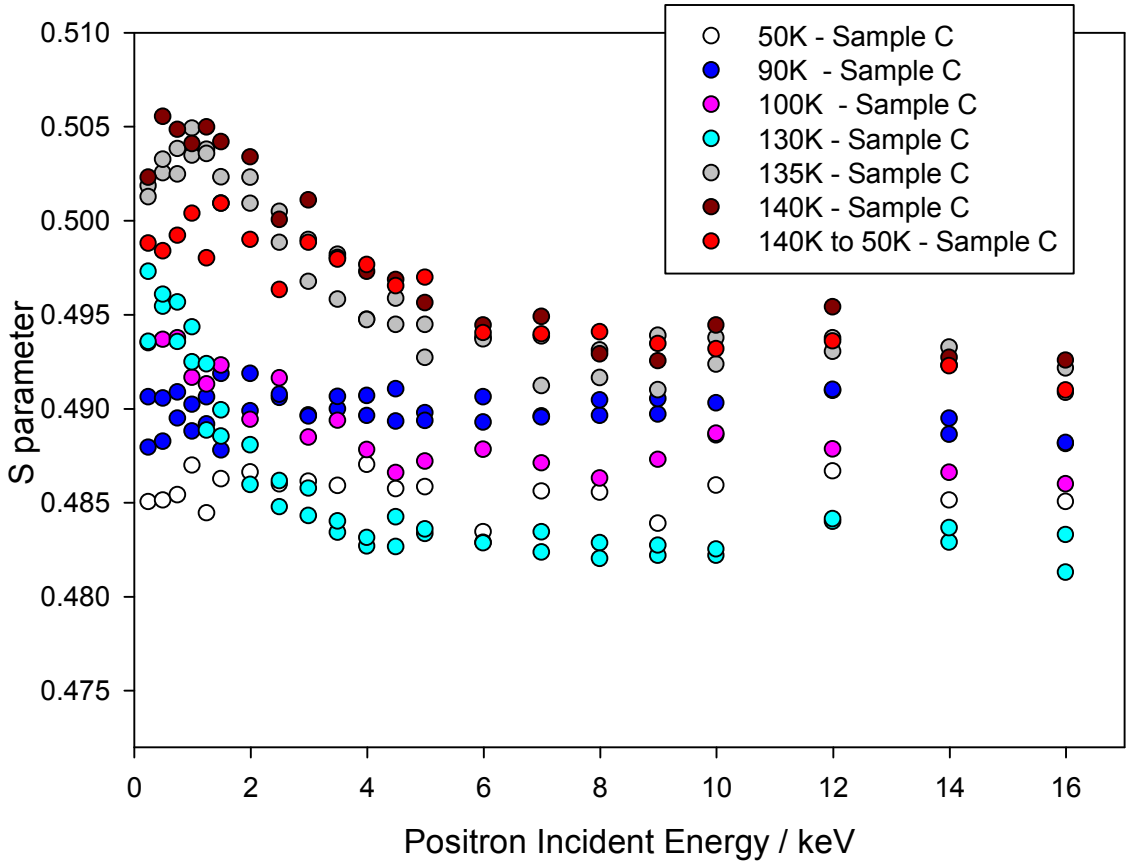

Figure 12: *S* parameter for sample C at different temperatures.

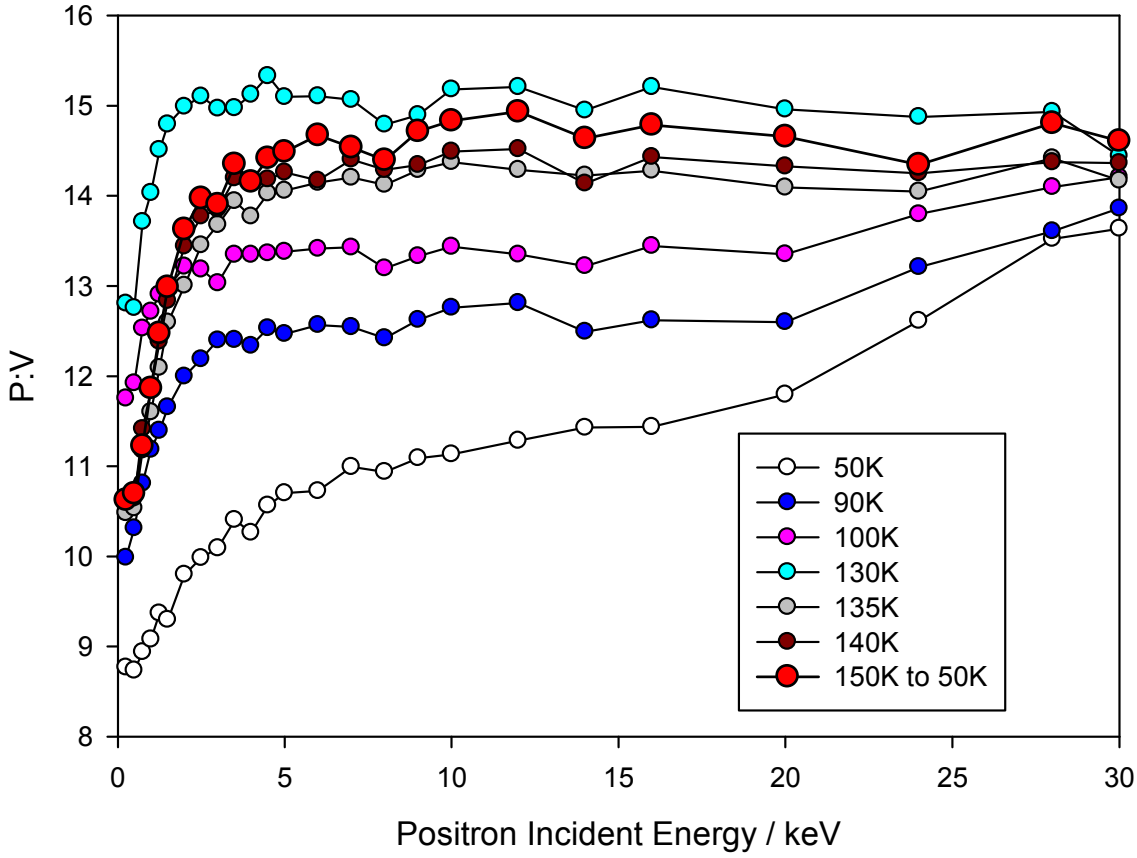

Figure 13: *P:V* for sample C at different temperatures.

As in sample B, sample C is quite thick, and therefore no reference value of copper is seen directly. This means that all the data are not normalised and cannot be confidently compared in absolute terms. Despite that, the shape of the *S* parameter holds some information.

Being grown on a different substrate does not seem to have any particular effect. The *S* parameter remains flat up to a temperature of 100K where a slight increase is seen near the surface (pink points, figure12). This increases further at 130K, suggesting a crystallization near the surface before it occurs in the bulk, consistent with samples A and B. It also strengthens the idea of the near-surface crystallization temperature being dependent on the initial growth conditions - the faster a sample is grown, the lower the temperature at which it crystallises. The reason why there is a near-surface increase in *S* after the sample is thought to have completely crystallised (135K) is not fully understood (but see sample E, later).

At the same time, *P:V* increases and shows a decrease in diffusion length as the sample temperature increases to 130K. Above 135K, i.e. where the sample is expected to crystallise, *P:V* drops to a value where it remains unaffected by further temperature changes.

It is also seen that any changes occurring when the sample is heated up are completely irreversible. When it is cooled down both the *S* parameter and *P:V* remain the same (red points on figure 12and figure 13).

Sample D

In order to investigate whether the growth temperature has an effect on the response of the sample, sample D was grown at 120K at 10^{-7} Torr. The *S* parameter and *P:V* were measured as the sample was being deposited, as shown in figures 14 and 15 respectively.

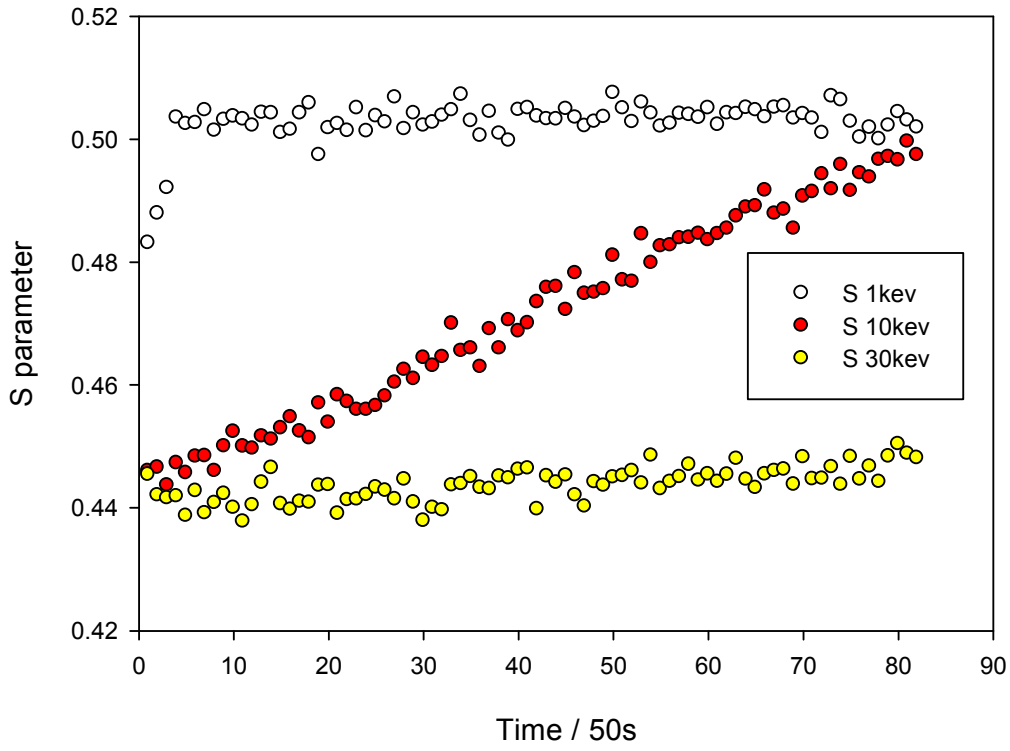

Figure 14: *S* parameter for sample D as it grows, measured at incident positron energies of 1keV (white) 10keV (red) and 30keV(yellow)

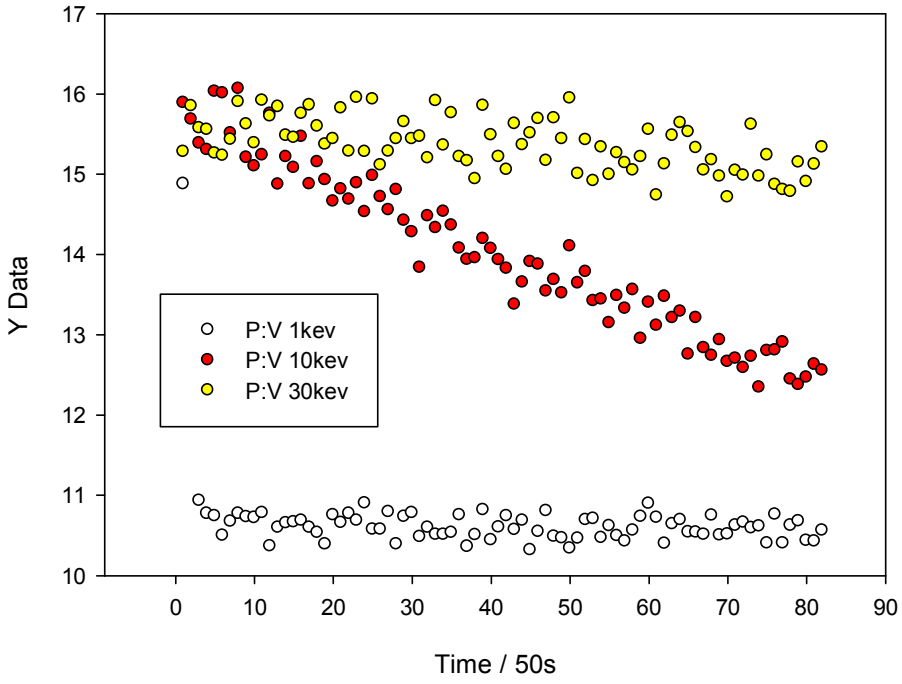

Figure 15: *P:V* for sample D as it grows, measured at incident positron energies of 1keV (white) 10keV (red) and 30keV(yellow)

As expected, the sample was grown at a crystalline state and is stable; no change occurs over time.

3.3.2 Discussion of samples A, B and C

The collective data of Samples A, B and C were put side by side to be compared. Figure 16 shows the S parameter for bulk and figure 17 for surface for all 3 samples. Figure 18 and 1 show the P:V ratios.

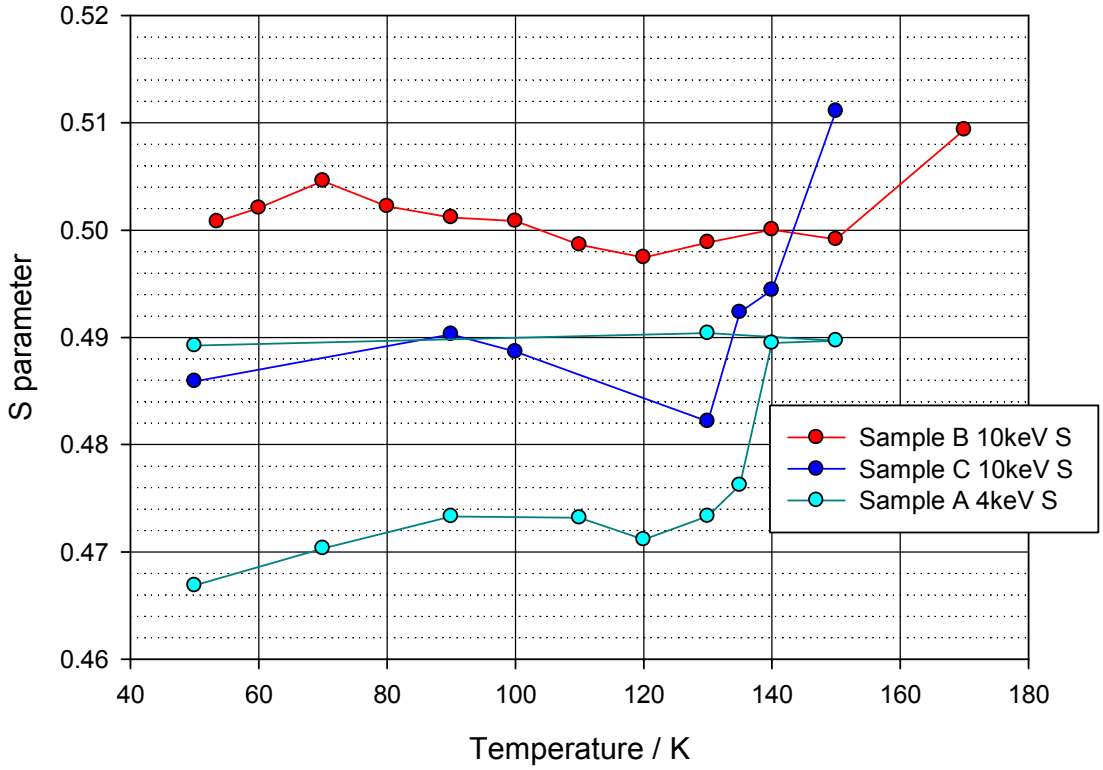

Figure 16: Collected data for bulk *S* parameters for samples A, B and C.

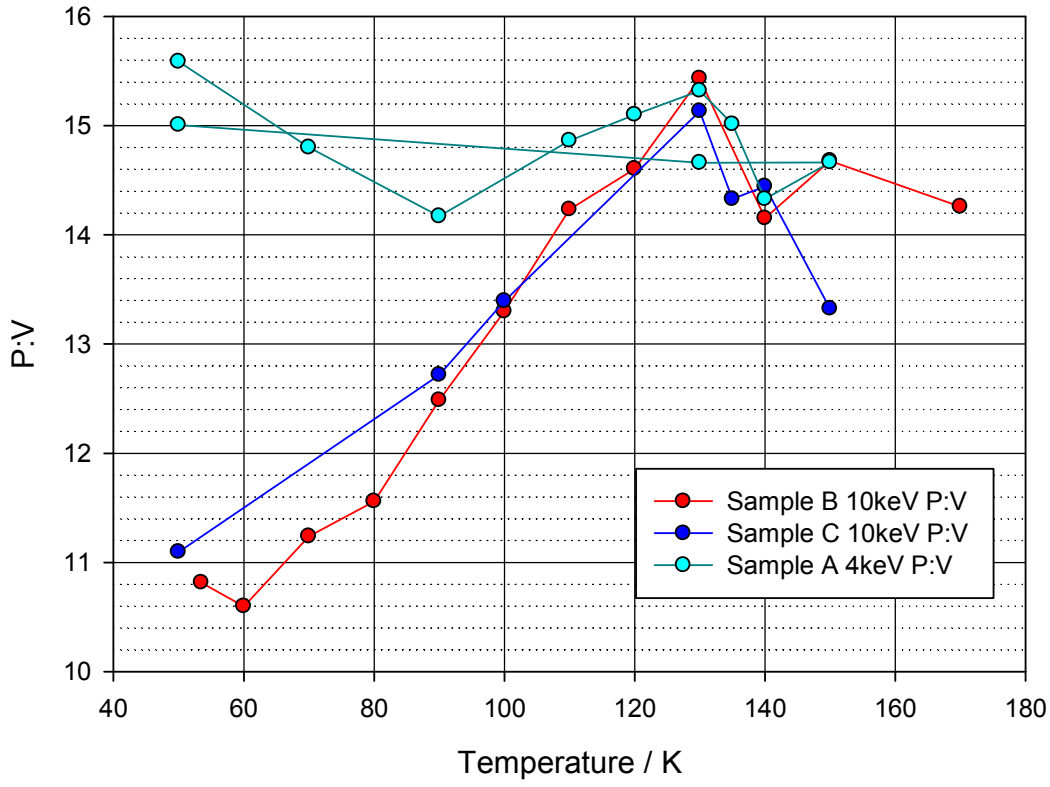

Figure 17: Collected data for bulk *P:V* for samples A, B and C.

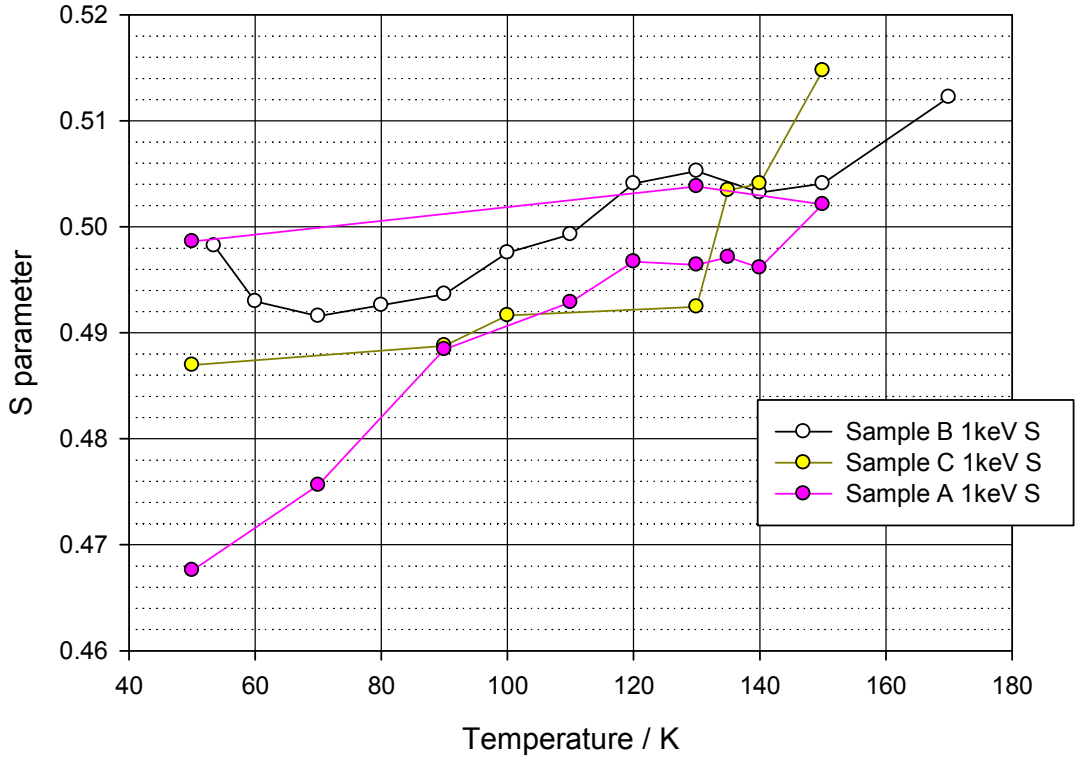

Figure 18: Collected data for near-surface *S* parameters for samples A, B and C.

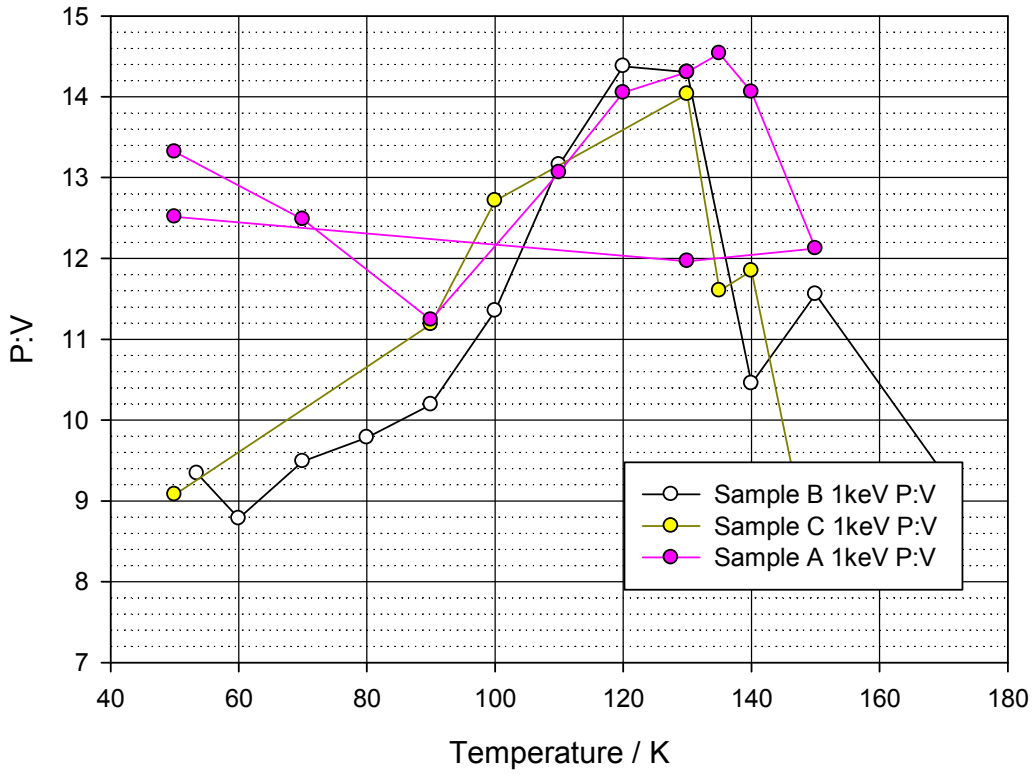

Figure 19: Collected data near-surface *P:V* for samples A, B and C.

The bulk of all three samples behave similarly. The *S* parameter increases and *P:V* decreases up to the point of crystallization which is at 135K for all three samples. Sample A's *P:V* is slightly different at low temperatures which could be explained by an odd initial state when grown, but then follows the other two samples.

For the surface, samples A and B seem to exhibit a constant increase in *S* but with a larger step at around 90K. Sample C's surface crystallisation seems to occur at 130K. *P:V* at the surface of the samples is similar to that in the bulk, with sample A having again an unusual *P:V* at very low temperatures.

P:V at temperatures above 140K is lower due to the sublimation taking place, creating a localised increase in pressure right above the surface of the samples. It is also noticeable from sample A that changes that occur are irreversible when the sample is cooled.

3.3.3 Post crystallization, Crystalline Solid Water: Results for samples E, F and G

Sample E

The sample has been grown at a high temperature (170K) meaning that it has been subliming and growing at the same time. The growth rate has been set to be greater (by the ambient water vapour pressure). This is estimated to have an effect on the structure of the sample, expecting numerous "bubbles" to exist throughout it. Measurements taken on the sample are without it growing and only subliming.

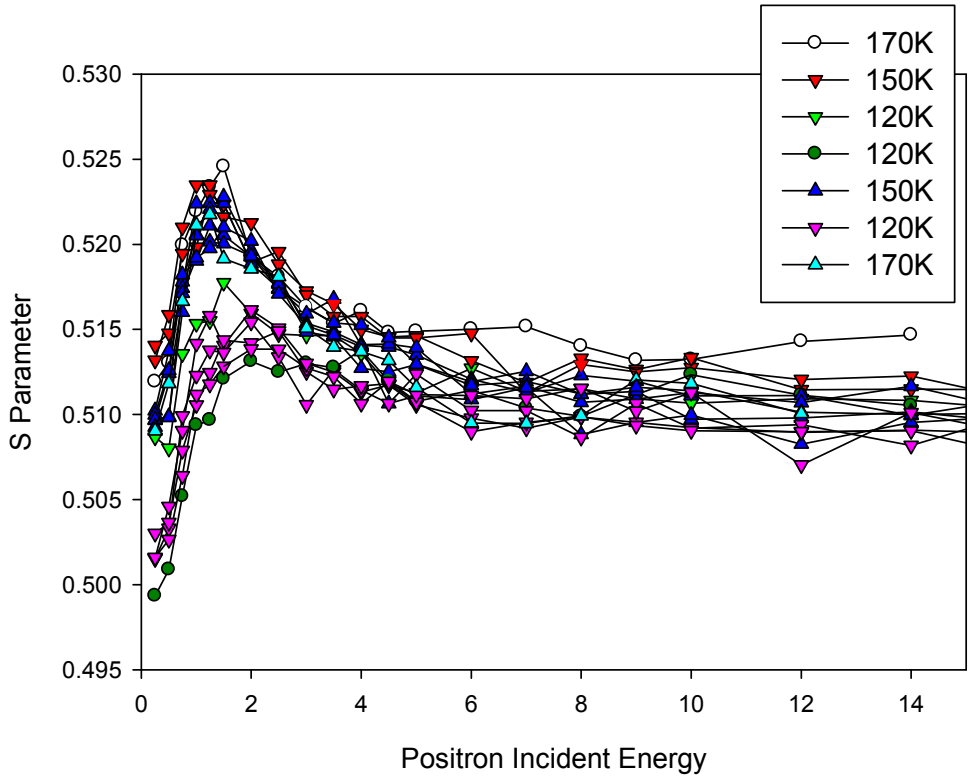

Figure 20: *S* parameter for sample E at different temperatures. Triangles - heating, inverted triangles - cooling to the temperatures indicated. Circles mean that the sample has been left to that temperature for a long period of time.

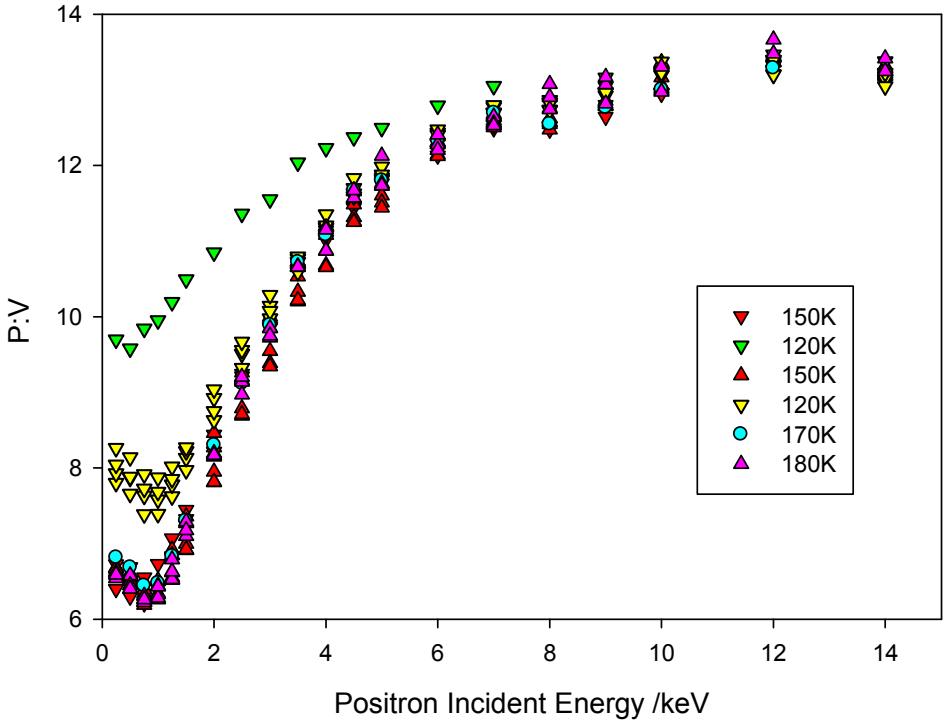

Figure 21: *P:V* for sample E at different temperatures. Triangles - heating, inverted triangles - cooling to the temperatures indicated. Circles mean that the sample has been left to that temperature for a long period of time.

From Figures 20 and 21 we can see a change that occurs between 150K and 120K. This change is slow and completely reversible and only seen near the surface of the sample. It can also be said that the positronium fraction in the bulk is not zero and that it has a very long diffusion length towards the surface. The large "bubbles" expected to exist in the bulk could justify the appearance of positronium there and a vigorous 'popping' effect near the surface at temperatures ≥150K causing these bubbles to interconnect could explain the long diffusion and the changes occurring. In essence, when the sample is subliming (temperatures greater than 150K) its surface "fizzes", creating tunnels and pathways for positrons and positronium to diffuse in from inside the bulk. As the sample disappears into the vacuum from the surface, new layers are revealed with more little bubbles that become more mobile as they approach the surface (evidence supported by the near surface ability to change easier than the bulk – as seen for low temperature solid ice) [11][12]. When it is cooled down to 120K sublimation ends and it undergoes a slow process (yellow triangles in figure 21 show a slow transition) where these tunnels seal up near the surface creating a thin "shell" around the sample and the number of positronium atoms that can diffuse to the surface decreases, increasing *P:V* (green triangles, figure 21). When the sample is heated up again to sublimation temperatures, the thin shell sublimes away, giving rise to exactly the same process described above.

This mechanism can also explain the near-surface rise in *S* parameter seen in sample C at 140K, which we were unable to explain earlier.

Sample F

Sample F is identical to sample E, except that it was grown at a higher water vapour pressure (10^{-4} Torr). Measurements were taken as it cooled from 170 to 150 to 120K, each temperature being maintained while repeating the measurements, and then heating up to 150 and 170K. It was allowed to grow very thick (~ tens microns) in order to have enough time for these measurements before complete sublimation. The *S* parameter is shown in figure 22 and *P:V* in figure 23.

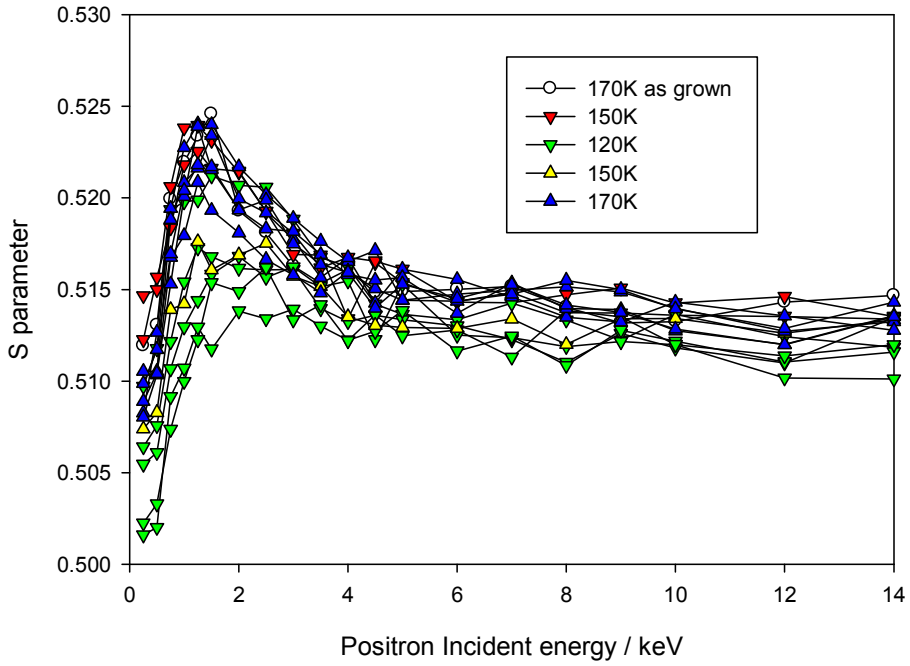

Figure 22: *S* parameter for sample F at different temperatures. Triangles - heating, inverted triangles - cooling to the temperatures indicated. Green Triangles indicate the change over time (not instant change) at 120K

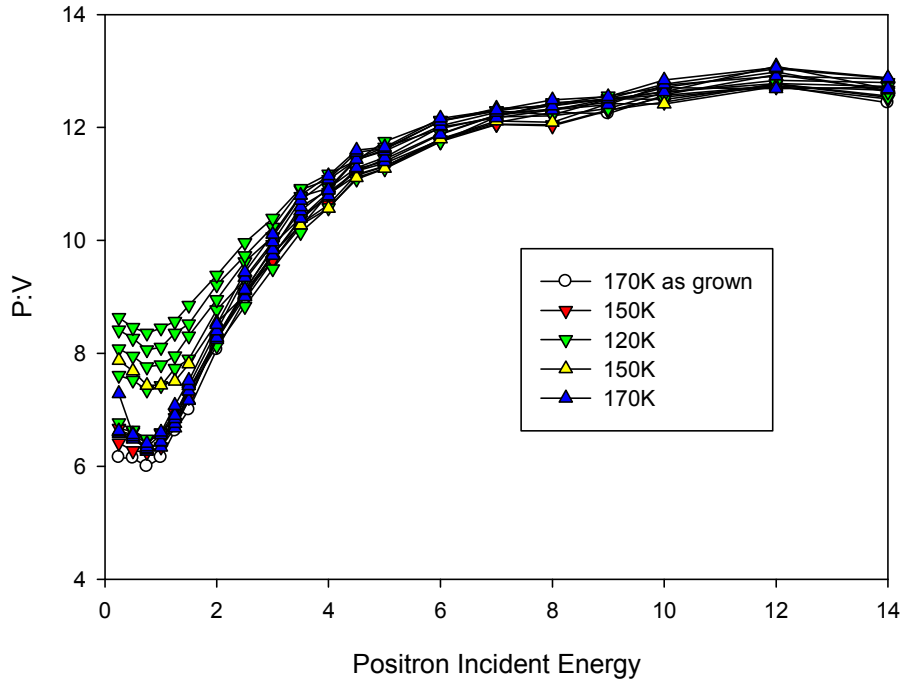

Figure 23: $P:V$ for sample F at different temperatures. Triangles - heating, inverted triangles - cooling to the temperatures indicated. Green Triangles indicate the change over time (not instant change) at 120K

This sample has an identical response to sample E. It confirms a surface structural change that affects both the S parameter and the P:V between 120K and 150K, which is completely reversible. It also shows that this change is not instant and it takes time to transit between the two states (cooling down green triangles, heating up yellow triangles – figures 22, 23).

Investigating if any changes occur at even higher temperatures proved to be rather difficult. The maximum temperature was limited to 180K, since the ice sublimation rate was so high that the water vapour pressure above the sample became high enough to measurably attenuate the incident positron beam.

Sample G

This sample was grown at 180K at 10^{-4} Torr, the limit of the experimental setup. The results are shown in Figures 24 for *S* and 25 for *P:V*.

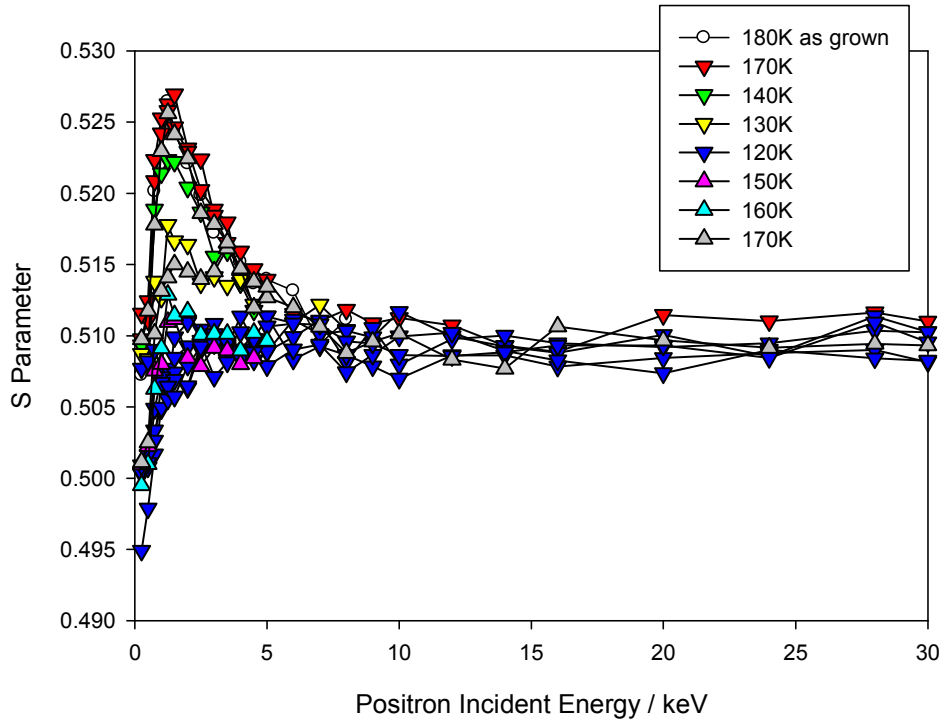

Figure 24: *S* Parameter for sample G at different temperatures. Triangles - heating, inverted triangles - cooling to the temperatures indicated. At 180K (brown triangles) the observations continued until the sample was completely sublimed.

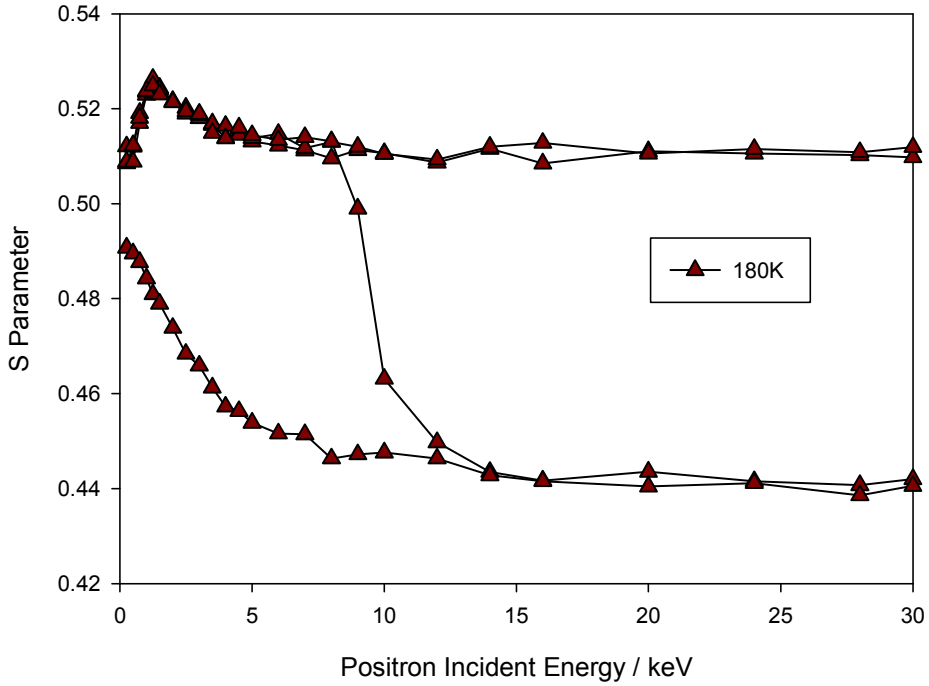

Figure 25: S parameter at 180K with repetitive measurements as the sample was subliming.

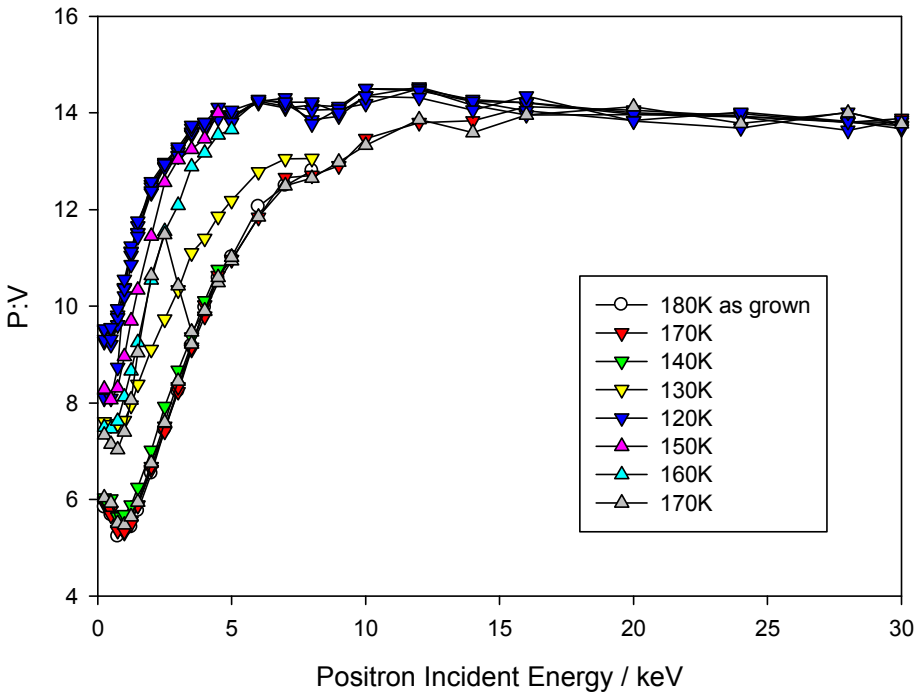

Figure 26: P:V for sample G at different temperatures. Triangles - heating, inverted triangles - cooling to the temperatures indicated.

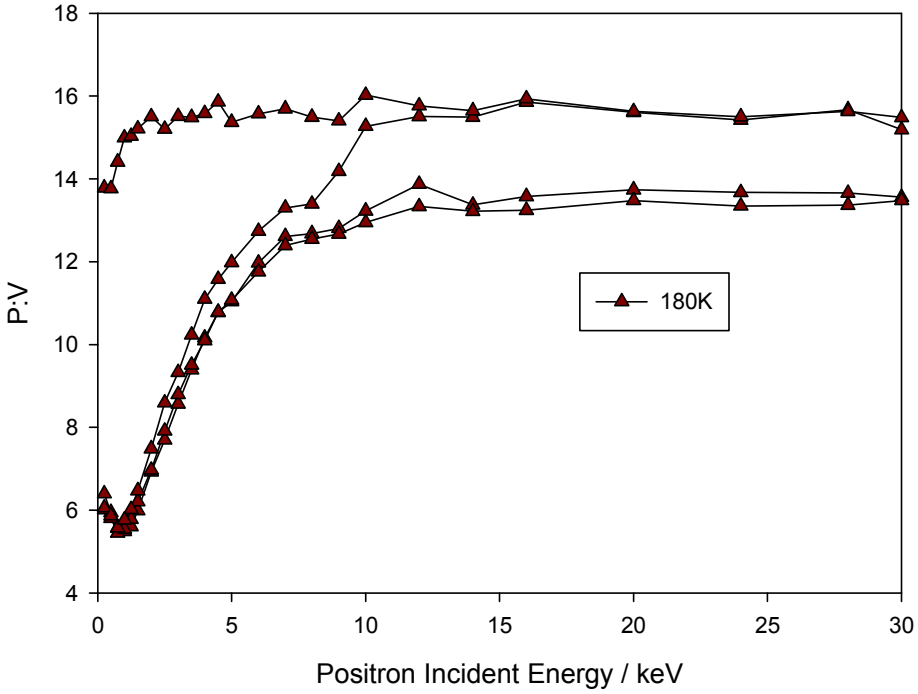

Figure 27: P:V ratio at 180K with repetitive measurements as the sample was subliming.

3.3.4. Discussion on samples E, F and G

These data do not offer any significant new information. At 180K the sample behaves exactly the same as 170K. Samples have also been grown at 140K at 10^{-4} Torr, 150K 10^{-4} Torr and 160K 10^{-4} Torr without showing any significant differences. They all behaved in a similar manner to samples E, F and G.

The preliminary data on sublimation offer hope that extended measurements of sublimation times vs sample temperature might yield information on the kinetics of sublimation.

3.4 Conclusions

VEPAS has proven to be a powerful non-destructive tool, with significant advantages over other techniques, when studying ice films at the low pressure – low temperature end of their phase diagram. It has demonstrated sensitivity to already-known phenomena such as the crystallisation of amorphous ice at ~135K, but also to discover new ones, such as the early surface crystallisation of amorphous ice at temperatures <135K, depending on the structure of the sample. The evolution of the

structure of both amorphous and crystalline ice has been successfully observed up to the limits of the technique. At high temperatures ice is subliming too fast to be studied, where at low temperatures background gases/vapours solidify on the surface of the samples. The low temperature limitation can be pushed further by using ultra high vacuum systems with pressures that are orders of magnitude lower.

Sparked by the success of these measurements, future experiments could study the phase transitions of other solidified gases or liquids such as oxygen, with interesting alpha and beta phases.

CHAPTER 3 REFERENCES

[1] There are many online summaries of basic water properties – for example http://www.lsbu.ac.uk/water/phase.html.

[2] O. Mishima and LD Calvert and E. Whalley *Nature* **310,** 393(1984).

[3] P. Jenniskens, D.F. Blake, M.A. Wilson and A. Pohorille, "High-Density Amorphous Ice, the Frost on Interstellar Grains", Astrophysical J. **455**, 389 (1994).

[4] O. Mishima, "Relationship between melting and amorphization of ice", Nature **384**, 546 (1996).

[5] S. J. Tao, "Positronium Annihilation in Molecular Substances", J. Chem. Phys. **56**, 5499 (1972).

[6] O.E. Mogensen, F.M. Jacobsen, "Positronium yields in liquids determined by lifetime and angular correlation measurements", Chem. Phys. **73**, 1 (2001).

[7] P. G. Coleman (ed), "Positron Beams and their applications" (World Scientific: 2000).

[8] K.P. Stevenson *et al*, "Controlling the Morphology of Solid Amorphous Water", Science **283,** 1505 (1999).

[9] Giorgio Nebbia, Gabriella Nebbia Menozzi, "Early experiments on water desalination by freezing", Desalination **5**, 49 (1968).

[10] Peter H. Poole, Ulirch Essmann, Francesco Sciorthino, H. Eugene Stanley, "Phase diagram for amorphous solid water", Phys Rev E**48**, 4605 (1993).

[11] Ming-Taun Leu *et al*, "Morphology and Surface Areas of Thin Ice films", J. Phys. Chem. B **101** 6259 (1997).

[12] George E. Ewing, "Thin Film Water", J. Phys. Chem. B, **108** 15953 (2004).

CHAPTER 4: POSITRON ANNIHILATION STUDIES OF THIN FILMS, VACANCIES AND MATERIAL STRUCTURES

4.1 INTRODUCTION

All positron annihilation techniques, when coupled to a positron beam, are very powerful for studying thin films and depth profiling vacancies of various materials. They are highly sensitive to open volume point defects (i.e. down to 1 missing atom in 10^7 [1]) and can provide information about the size of these volumes and the defect concentration. Every technique, as described in previous sections, has its own advantages and disadvantages. The positron annihilation method used for this project, VEPAS, is very useful in giving semi-quantitative measurements of the number of vacancies in the material [2], a relative measurement of the vacancy or pore sizes and the atomic structure of the material. It offers non-destructive, straightforward and relatively quick measurements. Other techniques that can offer competitive or complementary information to that provided by VEPAS include the following:

DLTS (*Deep Level Transient Spectroscopy*), developed in 1974 by D. V. Lang [3], studies space charge defects in the depletion regions of electronic devices. It does so with the use of voltage pulses in reverse bias. This decreases the size of the depletion region and allows free carriers to flow in the newly uncovered electric field free areas, recharging defects. The device then returns to equilibrium at the end of the pulse. The useful data comes from the direct measurement of the capacitance caused by these defects. DLTS has a higher sensitivity than almost any other semiconductor diagnostic technique - e.g. in Si it can detect impurities and defects at a concentration of one part in 10^{12} of the material host atoms [4]. Its extreme sensitivity along with the experimental simplicity make this an attractive process but it is very limited to the defects and materials it can study.

E*lectron spin resonance (ESR)* [5] was observed by Yevgeny Zavoisky in 1944. It excels in studying chemical species with unpaired electrons. The basis for this technique is similar to that of nuclear magnetic resonance (NMR), but instead of exciting spins of nuclei, it excites spins of electrons. It is limited to certain defects and

bulk materials with appropriate magnetic properties, but has been widely used, sometimes in conjunction with other techniques, to provide information on a wide variety of defects (e.g. the work of Watkins and collaborators over many years [6]).

High Resolution TEM [7] creates an atomic scale image of the crystal structure of materials. It has a high resolution, of the order of 0.08nm, making it a powerful technique when studying materials at the nanoscale, e.g. semiconductors. Unfortunately it is a destructive process that requires delicate sample treating and preparation. Thin slices of the samples are taken, making it impossible to study the same sample as it evolves, i.e. through annealing temperatures.

X ray diffraction [8,9] is a technique that utilises x-rays to study the crystalline structure of materials. It is non-destructive. It directly measures the intensity of x-rays being scattered by a sample at different angles (incident to scattered angle) and can create three dimensional electron density diagram. From this diagram, the mean atomic positions can be found as well as atomic disorder. However, its use in the study of thin films required glancing-angle geometry.

Neutron Scattering [9] describes a number of techniques where samples are subjected to neutron radiation and the deflection of neutrons is measured. Neutrons interact with the nuclei of materials and their deflection can relate to the material structure and magnetic order. There are two main categories of neutron scattering - elastic and inelastic. The first is when a neutron interacts with a nucleus but does excite it, i.e. the neutron does not lose any of its injected energy or gain any. The latter processes involves an energetic excitation or relaxation by the neutron, i.e. the injected neutron's energy contributes in creating an excitation or the neutron by absorbs the excess energy from a relaxation. They can study almost all forms of condensed matter and they can be produced readily (but expensively) at a nuclear reactor. This technique is, like X-ray diffraction, usually applied to bulk measurements, and is more commonly used to study the arrangements of atoms rather than vacancies.

Scanning Probe Microscopy [10] techniques are numerous, measuring different aspects of surface properties. They all incorporate a probe which is scanned across the surface of a sample which can vibrate at near resonance frequencies or hover steadily but differ in what they measure. Most popular ones are; AFM [10] which measures the atomic forces between the scanning probe (tip) and the surface atoms, STM [10] which measures the current of electrons tunnelling from the sample surface into the scanning probe, MFM which measures the magnetic forces between the scanning probe and the surface and other. All these techniques are very powerful and can provide information at an atomic level and at the same time be used as engineering tools in manipulating atoms. Nevertheless they are very limited to the type of samples they can study, each with its own specialisation, and cannot provide any information past the first (or sometimes second) atomic layer.

Despite the plethora of other techniques and their numerous advantages, Positron Annihilation Spectroscopy has features which makes it an appropriate technique for the experiments described in the following section. It is a non-destructive technique that can provide depth profiles of structure imperfections, vacancies, and impurities. It is easy to run (given a working experimental setup) and relatively quick. It is also found to be very useful for studying the same sample as it evolves, e.g. with annealing temperature.

4.2 POSITRON STUDIES OF SILICON RICH SILICA FOR OPTICAL AMPLIFICATION

4.2.1 Erbium-doped silicon-rich silica: Introduction

Photonic materials are, in general, materials that have useful optical properties for both fundamental research and applications. There are almost no silicon based photonic materials due to some of silicon's basic properties [11]. Firstly, silicon emits photons at wavelengths of no interest (i.e. wavelengths widely used by telecommunications) due to its wide band gap. It also makes photon emitting very hard due to its indirect band gap, i.e. a band gap in which the minimum energy transition gap between the valance band and the conduction band is shifted by a k-vector. This k-vector shift corresponds to a difference in momentum. Silicon has

always been a semiconductor that would be preferred for optical applications if it did not have these limiting properties. Silicon is cheap and widely used in electronics (would making photonic – electronic integrations easy) and methods and techniques for processing are quite advanced. A promising silicon-based material to serve as an optical source and/or amplifier is erbium (Er) doped silica (SiO_2) with silicon (Si) nano-clusters. [11]

Light emitting devices are required to emit light efficiently in a controlled way at a useful wavelength. They use electron transitions in different energy levels in order to create photons or to power up the system. These transitions fall into 3 main categories [12]:

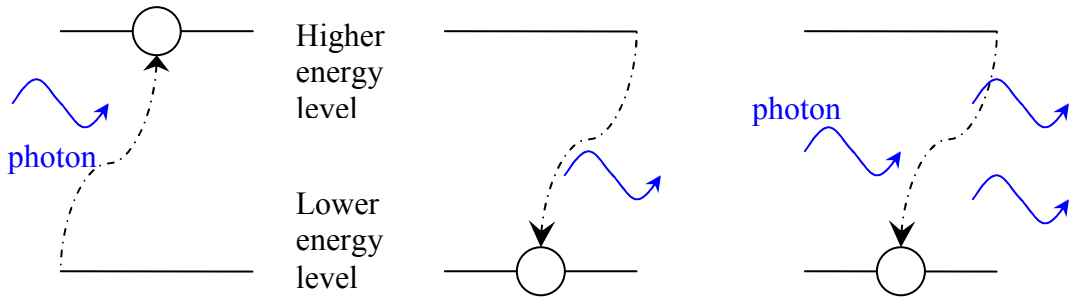

a) Absorption b) Spontaneous emission c) Stimulated emission

Figure 1: The three basic electron transition mechanisms considered in photonics.

a) Absorption: When an incoming photon has an energy exactly matching the gap of two energy levels of an atom and there is an available electron in the lower level and an available hole in the higher, the photon gets absorbed and the electron is then excited to the higher energy level.
b) Spontaneous emission: Excited electrons have a relative lifetime of de-excitation to a lower energy level (assuming there is a state available). This de-excitation is a probabilistic effect and when it happens it emits a photon of energy exactly the same as the energy difference of the two energy levels.
c) Stimulated emission: Excited electrons can be stimulated into de-exciting by an incoming photon whose energy is matching that of the de-excitation (i.e. the energy difference of the two energy levels). The result is two coherent photons.

For a photon travelling through a medium, absorption and stimulated emission are the transitions of interest. Their probability of occurring is solely affected by the

population of electrons available in the two energy states involved so in order to have a good amplifier or light source, there has to be a way of exciting electrons completely independent of the communication signal (photons travelling through the medium) i.e. achieving population inversion. This is usually achieved by using different wavelength photons (pumping light) to excite electrons to an even higher energy state from which they de-excite relatively fast to the energy state of interest, also known as a three state system. Four state systems can also be used.

Erbium-doped silica with silicon nano-clusters is based on the three level system but utilises the property of silicon nano-clusters to transfer energy of their excited electrons to nearby erbium atoms figure 2. Erbium, a rare earth material, emits light at 1550nm, a wavelength widely used by communication networks, and silicon is a broad band absorber but completely transparent to the 1550nm. Therefore a cheap LED can be used to pump high energy light in the system (usually in the visible range) and excite electrons from the valence band to the conduction band. Then the electrons drop to a lower energy within the conduction band at which a transition is available to the valence band with energy matching a transition in the erbium. The silicon electron de-excites and simultaneously the erbium electron excites to a higher energy state (E3), quickly de-excites to E2 from which stimulated or spontaneous emission would occur (see Figure 2).

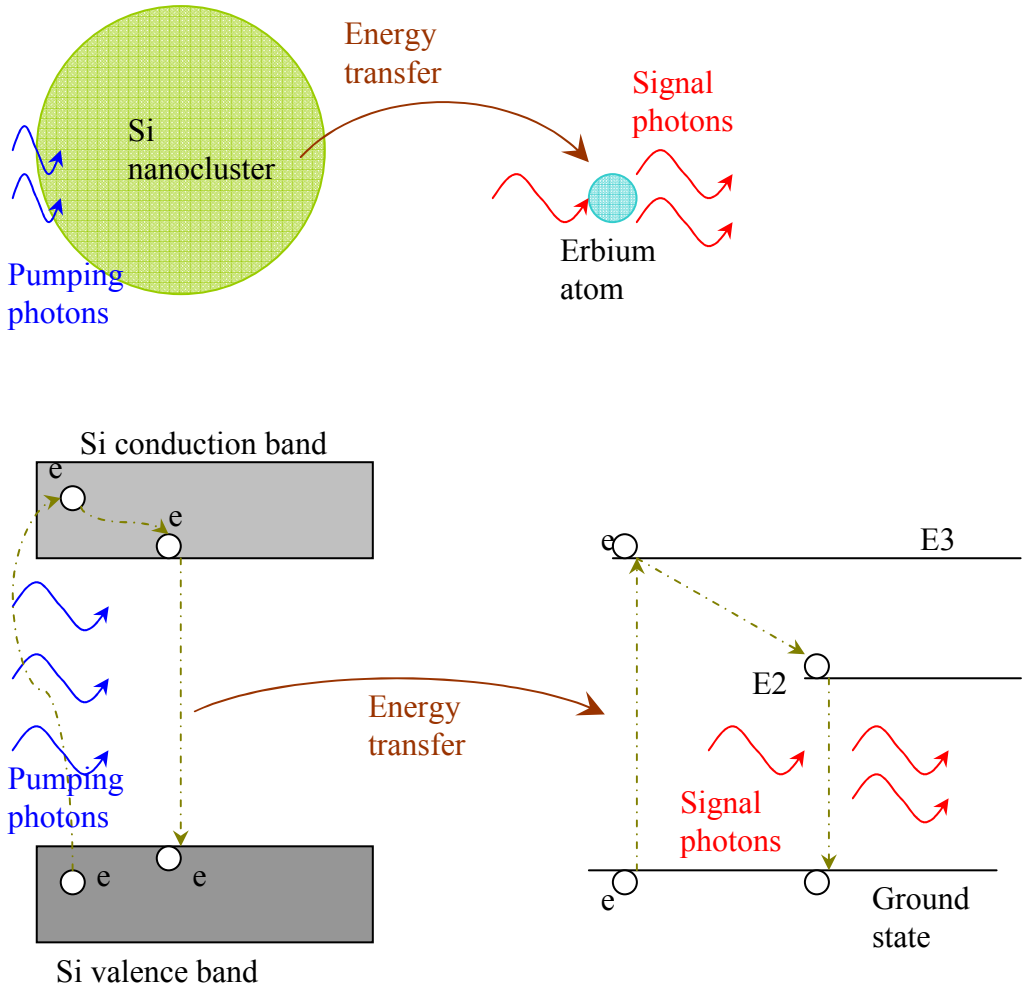

Figure 2: A simplified representation of the erbium doped silica with silicon nano-cluster amplifying operation.

The mechanics of the energy transfer from the nano-cluster to the erbium ions is unknown, and it is debated whether it is done by the interface of the nanocluster or its bulk. VEPAS can be potentially used to provide more information on the state of the interface [13].

Positrons are also a powerful tool in studying the evolution of the formation of these nanoclusters at different annealing temperatures and correlate them with their optical activity.

4.2.2. VEPAS measurements of Er doped silicon rich silica.

The first samples received [14] had been prepared using a variation of doping techniques, doping levels (i.e. erbium concentrations), and different preparation steps, as shown in Table 1.

Sample number	Er concentration (cm^{-2})	Er Doping technique	Si implanted + annealed?	Anneal in forming gas (N_2:H_2, 95%:5%) ?
11	$8x10^{14}$	Diffusion	Yes	No
12	$8x10^{14}$	Implant	Yes	No
14	$8x10^{14}$	Diffusion	No	No
15	$8x10^{14}$	Implant	No	No
11H	$8x10^{14}$	Diffusion	Yes	Yes
12H	$8x10^{14}$	Implant	Yes	Yes
16	$3x10^{14}$	Diffusion	Yes	No
17	$3x10^{14}$	Implant	Yes	No
19	$3x10^{14}$	Diffusion	No	No
20	$3x10^{14}$	Implant	No	No
16H	$3x10^{14}$	Diffusion	Yes	Yes
17H	$3x10^{14}$	Implant	Yes	Yes

Table 1: Initial batch of samples investigated to evaluate factors affecting the sensitivity of positrons to material features.

Initially measurements were taken to investigate whether positrons are sensitive to any of the material features in the samples listed in Table 1 and, if so, what information they can provide about them. *S* parameter measurements were thus taken for all these samples and plotted and compared.

The results seen in Figures 3 and 4 suggest that positrons are not directly sensitive to the Er ions, but can see the vacancies associated with their implantation. It is also seen that the effect of the nanoclusters as seen by positrons is greater than the effect of Er. Hydrogenation of samples also seems interesting as it eliminates the trapping sites for positrons and increases the positron diffusivity in the material.

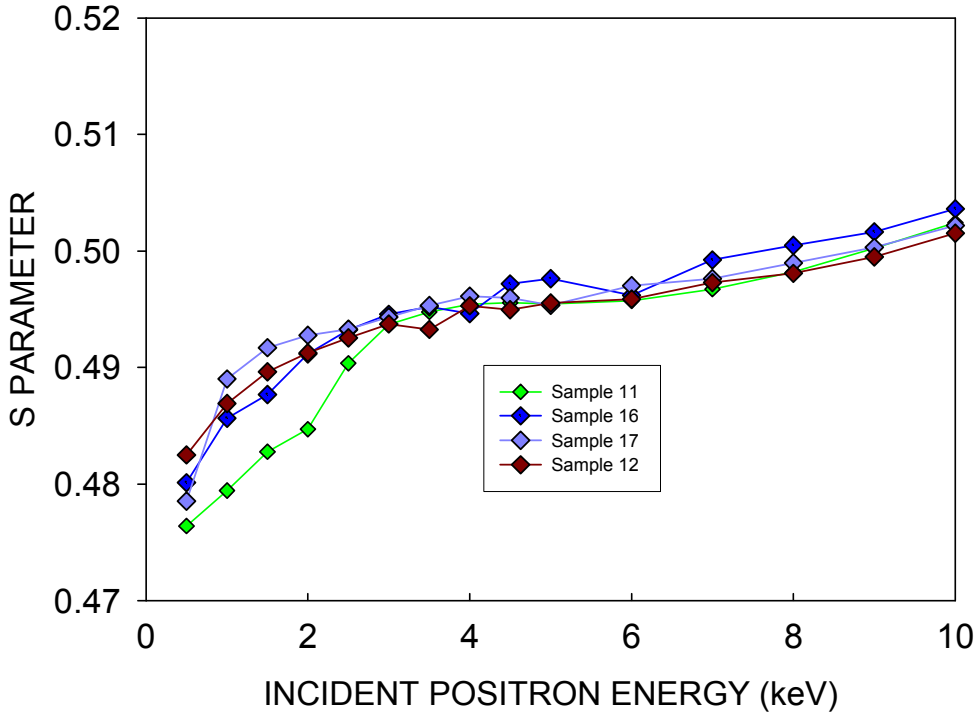

Figure 3: *S* parameter measurements for samples with Si nanocrystals. Samples 11, 12 (Er implanted/diffused), and 16, 17 (same, lower Er dose), directly comparing the effect of the doping techniques and doping levels

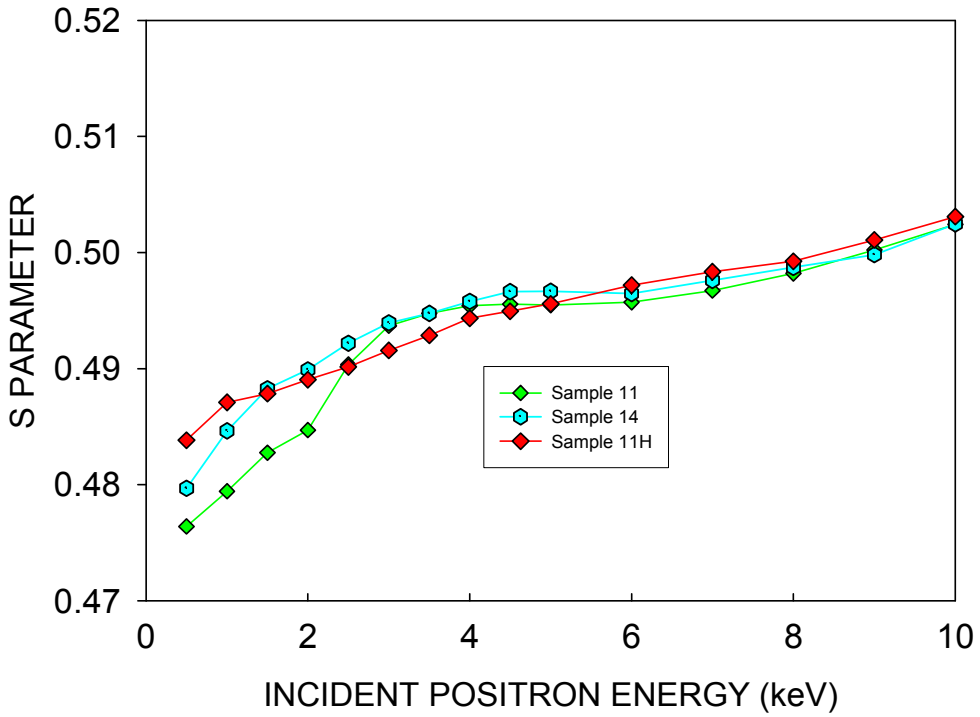

Figure 4: *S* parameter measurements for samples 11, 11H (with nanocrystals, with and without H), and 14 (same as 11 but no nanocrystals), directly comparing the effect of the hydrogenation and nano clusters.

4.2.3 Evolution of Si nanoclusters

Further samples (Table 2) were fabricated [14] in order to investigate the effect of annealing time and temperature on the material and specifically on the nano clusters, ideally forming a timeline for their formation and nature. *S* parameter measurements are shown in Figure 5.

Sample number	Annealing temperature	Annealing time	Si implantation energy
nSi 1	1100^0C	1 second	80 keV
nSi 2	1100^0C	5 seconds	80 keV
nSi 3	1100^0C	10 seconds	80 keV
nSi 4	1100^0C	100 seconds	80 keV
nSi 5	1100^0C	1 hour	80 keV
nSi 6	900^0C	1 hour	80 keV

Table 2: Second batch of samples for the investigation of the evolution of the nanoclusters.

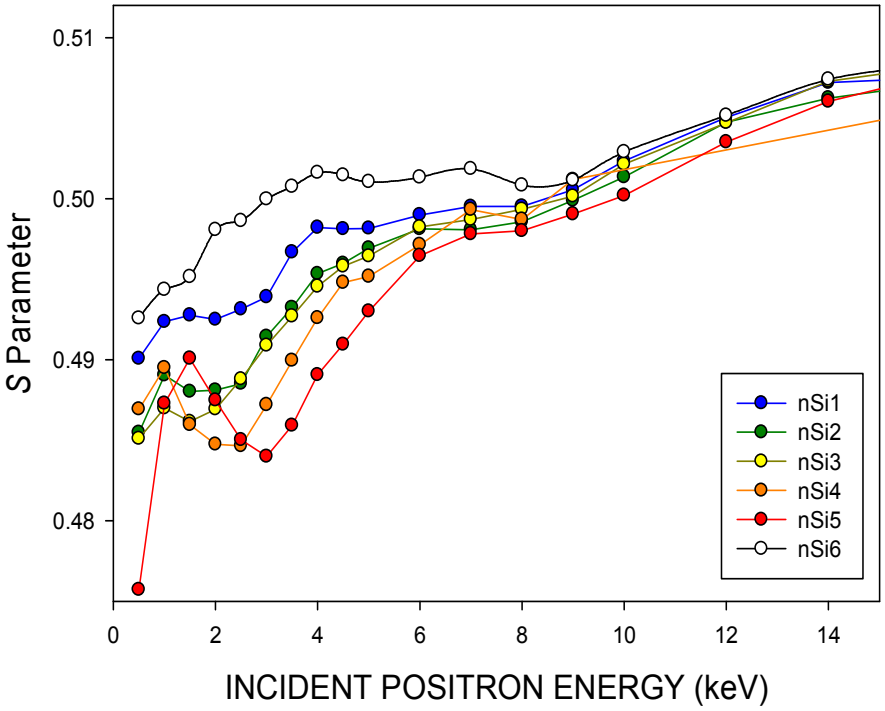

Figure 5: $S(E)$ for the family of samples of SiO_2 with Si nano clusters on Si bulk annealed for different times and at different temperatures (see Table 2).

Two models may be applied to explain the measurements shown in figure 5. Before describing these models, we consider first the simulation of the distribution of vacancies created and of the implanted Si atoms using software called SRIM [15] (Figure 6). This simulation does not model any post-implantation ion or vacancy movement, calculating only their distribution at the moment of implantation.

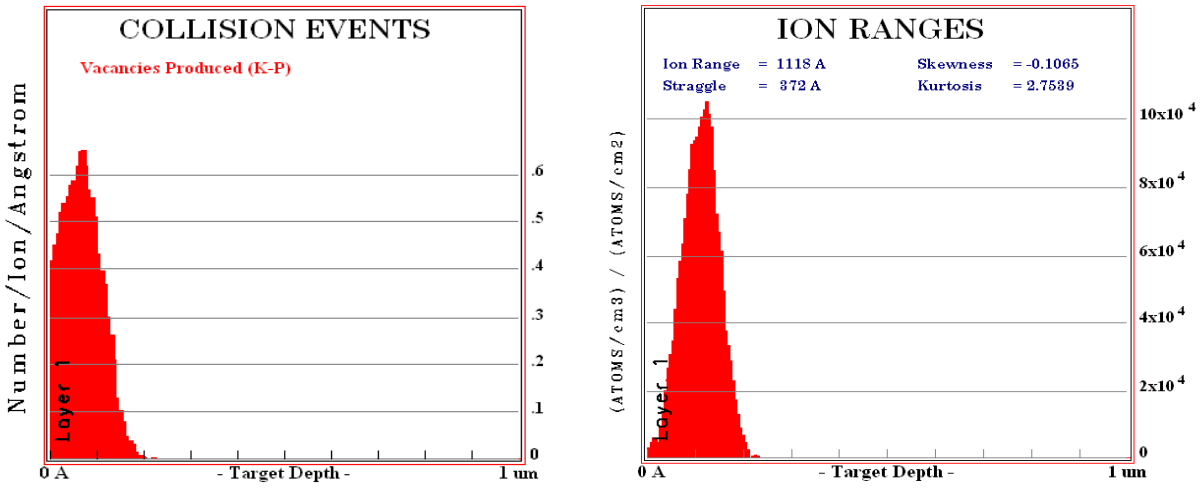

Figure 6: (Left) Vacancies created in SiO_2: (Right) Si ion distribution for the implantation of Si atoms at 80keV.

The first of the two possible fitting models applied to the data was a three-layer model:

1st layer: Heavily damaged silicon-rich silica. As the sample gets annealed at 1100ºC the excess silicon starts to form nanoclusters which grow in size with time. The *S* parameter decreases with increased cluster size and the nanoclusters move deeper in the sample. The *S* parameter associated with the nano clusters dominates that due to the vacancies.

2nd layer: SiO_2 – a constant characteristic *S* parameter.

3rd layer: Si bulk - a constant characteristic *S* parameter.

The second possible fitting model involves four layers, separating the vacancies from the nano clusters and not requiring any cluster movement in silica:

1st layer: A very thin layer near the surface (~50-100nm) heavily populated by vacancies (see figure 6). The *S* parameter of this layer remains constant

throughout the annealing steps as 1 second would be enough to form small, stable multi-vacancy clusters.

2nd layer: A layer extending from ~ 80-150nm consisting of vacancies and silicon atoms. During the annealing steps vacancies would not change by much, whilst the Si atoms move around clustering together; the longer the annealing, the bigger the clusters. For sample nSi1 the clusters would be too small to be seen by positrons but their affinity will increase with their size, and eventually their *S* parameter dominates that of the vacancies.

3rd layer: SiO_2 - a constant characteristic *S* parameter.

4th layer: Si bulk - a constant characteristic *S* parameter.

Both models are very similar, but the latter seems more realistic. Nanoclusters are relatively big and would not be very mobile in silica. Furthermore, the second model takes into account the difference in depth in the distribution of vacancies and implanted Si as demonstrated by SRIM. Therefore, even though the first model is mathematically possible, it does not seem to reflect the physical aspects of the material as well.

4.2.4 Positron measurements of optically active silicon rich silica

An interesting question in the area of light emission from Si nanocluster systems is whether the interface of a nanocluster is involved in the energy transfer from the nano cluster itself to nearby Er ions. It is argued by some that the energy transfer happens from the bulk and by others from the surface of the nano clusters [16,17]. In attempt to answer this question the positron response was recorded when the samples were illuminated by light of wavelength ~ 470nm, thereby exciting electrons in the nanoclusters. To illuminate the samples while taking positron measurements; LEDs were mounted on the sample holder (Figure 7). The light used in all the measurements is of wavelength 470nm (blue) and the LEDs [18] had a narrow illumination angle (30º). The power input range was 0-4W but the exact LED output is unknown as the diodes heat up significantly in vacuum, lowering their efficiency.

The results of *S* parameter measurements for sample nSi 5 with and without illumination are shown in Figure 8.

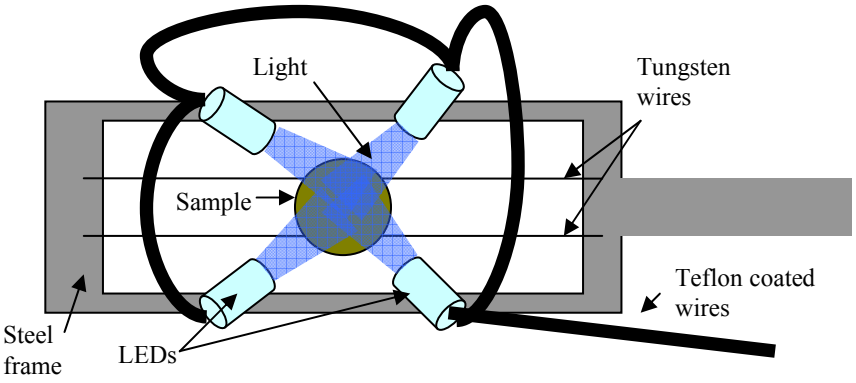

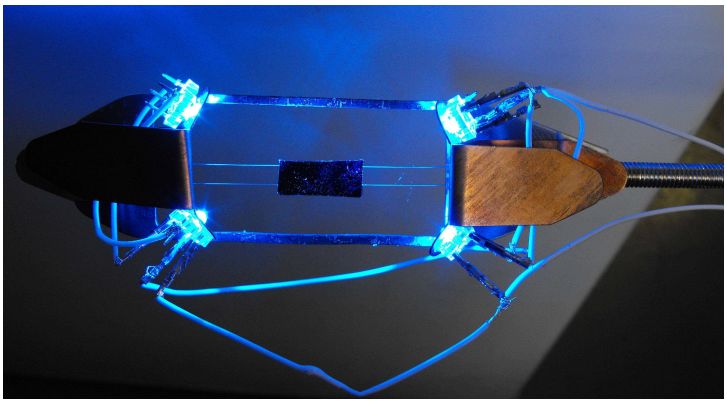

Figure 7: LED arrangement on the sample holder, illuminating the sample with blue light (470nm).

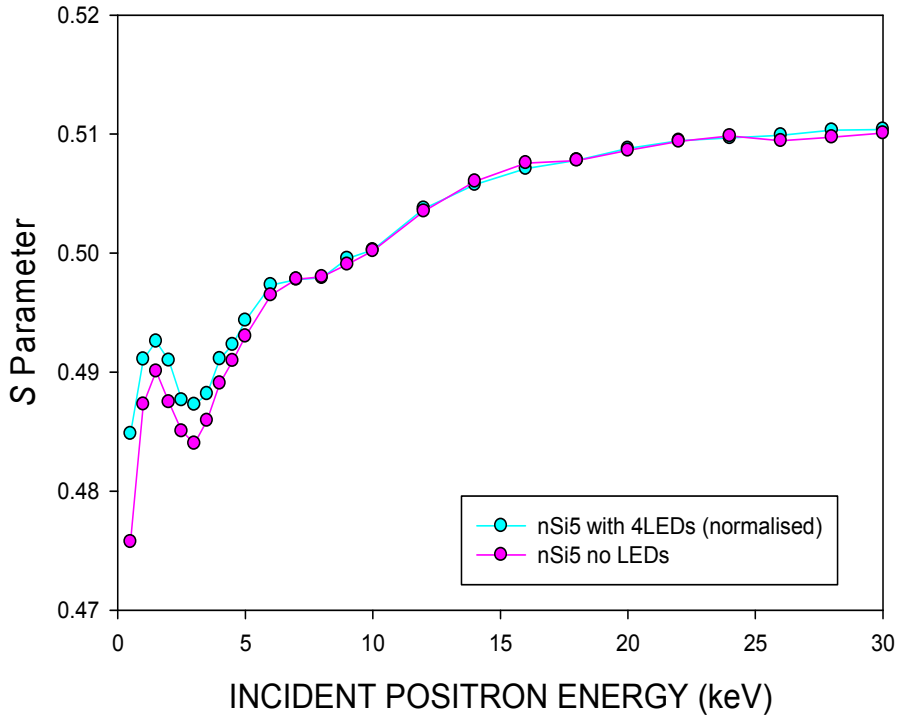

Figure 8: Sample nSi 5 unilluminated (pink symbols) and illuminated with blue light (470nm) (cyan symbols).

The effect of changing LED power on *S* values at positron energies of 1.5 and 3 keV (corresponding to mean depths of 33 and 100 nm, respectively) is shown in Figure 9.

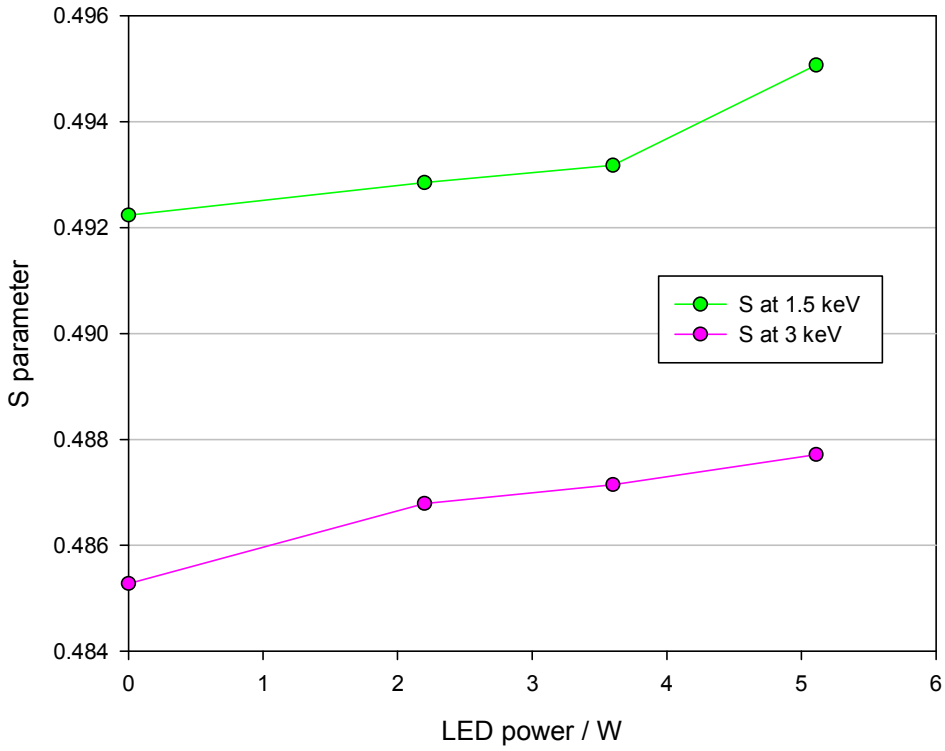

Figure 9: The effect of light at different LED input power on *S* parameters at positron energies of 1.5keV and 3keV, corresponding to mean depths of 33 and 100 nm.

In order to probe whether any change seen was due to the nano clusters specifically or if it could be seen in any Si-SiO_2 interface, simple SiO2-Si samples were fabricated, with the interface at the same depth as the nanoclusters in the previous samples. All the data were fitted by VEPFIT and the difference between fits was examined with and without illumination. No significant difference was observed.

In order to illuminate with light of higher intensity a different arrangement of the LEDs was constructed, as shown below. The arrangement had 24 LEDs of similar specifications as before.

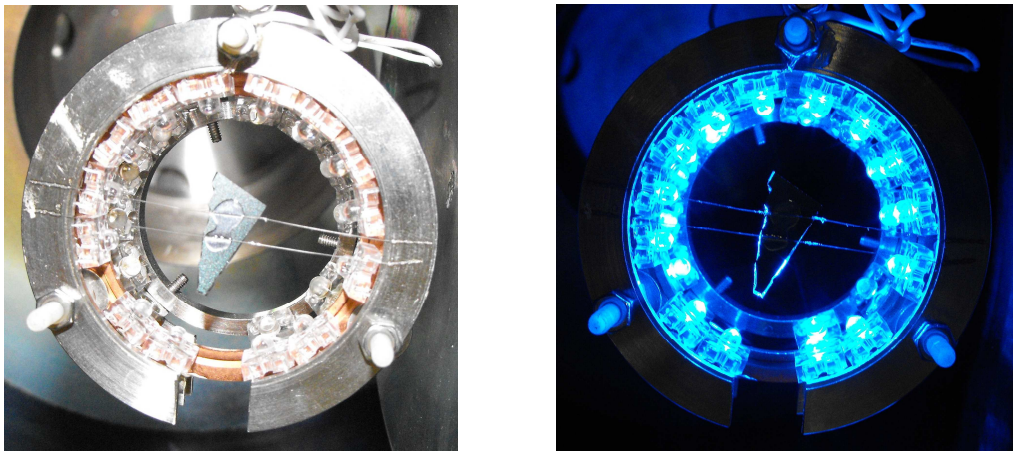

Figure 10: 24 LED arrangement for more intense sample illumination, off(left) and on(right).

The 24- LED setup was used with sample nSi5 in order to induce a larger change in positron response on illumination (Figure 11).

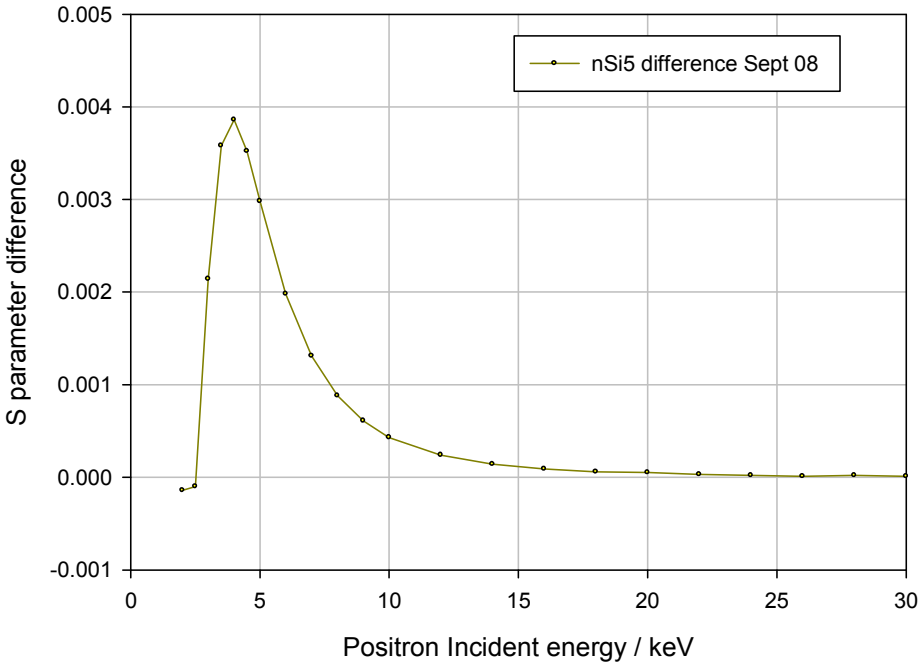

Figure 11: The effect of light on sample nSi5 studied with the 24 LED setup. The *S* parameter difference is the difference between fitted *S*(*E*) plots with and without illumination at maximum power.

Sample nSi5 was studied again after eight months, but the effect of illumination was considerably smaller than had originally been observed in Figure 11. This could be explained by an ageing of the sample – e.g., the out-diffusion of hydrogen atoms at room temperature. If this is true, then hydrogen has a significant role in the optical activity of the nano clusters or it greatly affects the response of positrons to it. To investigate and check this argument, it was attempted to re-introduce hydrogen in the sample by annealing in forming gas (5% H 95%N) at 475ºC for 15 minutes. This resulted in an increase in the effect of the light on the sample (see Figure 12), although not to the level originally seen.

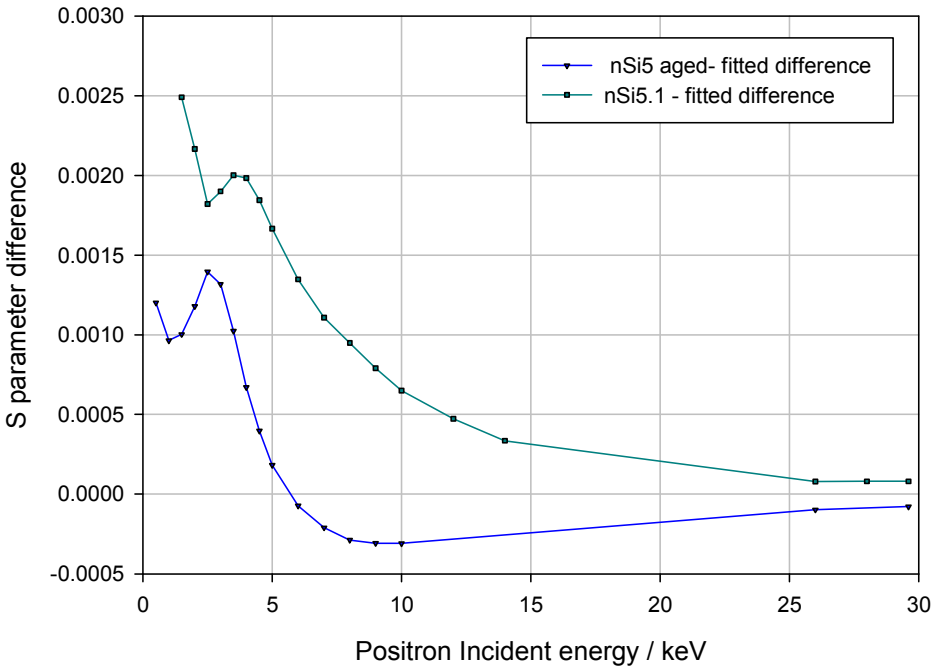

Figure 12: Effect of light on the nSi5.1 sample after 8 months (blue) and after re-annealed in forming gas (cyan).

In order to confirm the results above, sample nSi6 (having no pre-formed nanoclusters) was annealed on site at 1100ºC in forming gas for 30 minutes in order to create nano clusters and to introduce H. The sample was relabelled nSi7. This sample was then illuminated by the 24 blue LEDs (Figure 13).

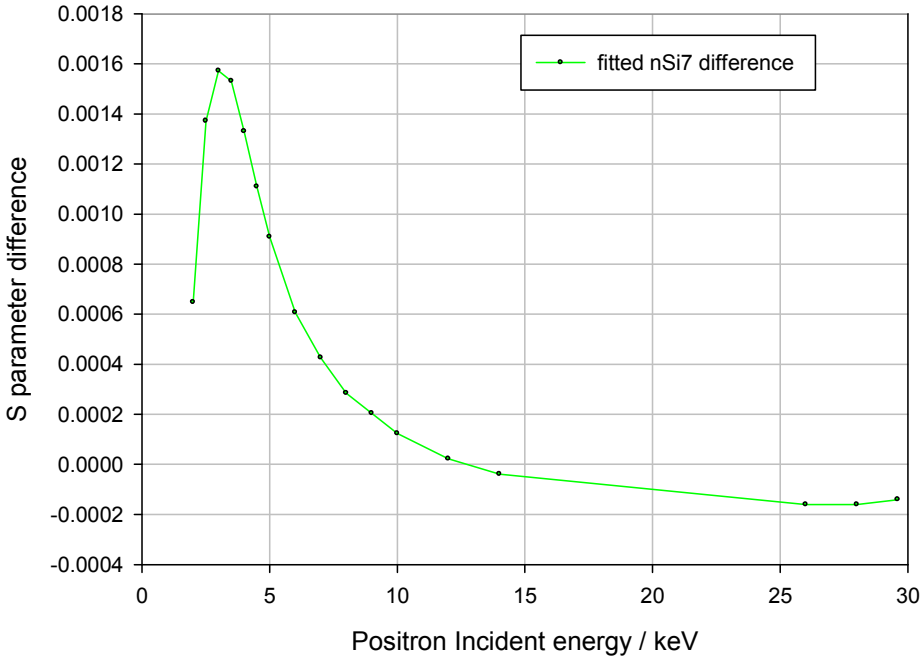

Figure 13: Difference between fitted *S* values with and without 24 LED illumination of sample nSi7.

The response of nSi7 has features similar to the results for nSi5 - i.e., an increase in *S* in the region where nano clusters are present when illuminated. The magnitude of this change is relatively small, but significant enough to allow us to verify that positrons can measure the response of the nano clusters to light.

All the samples investigated so far did not have Er implanted. Er in these samples "activates" when the sample is annealed, i.e. becomes Er^{3+} [19]. The localised charge of Er^{3+} would be expected to repel positrons, not allowing them to annihilate in their immediate surroundings. To investigate this, sample 12H was studied but at a later time - i.e., the sample was aged. To try to compensate for the ageing process, the sample was then re-annealed at 475 ºC in forming gas for 15 minutes, now labelled as 12H.1. The effect of light for both cases is shown in Figures 14 and 15 below.

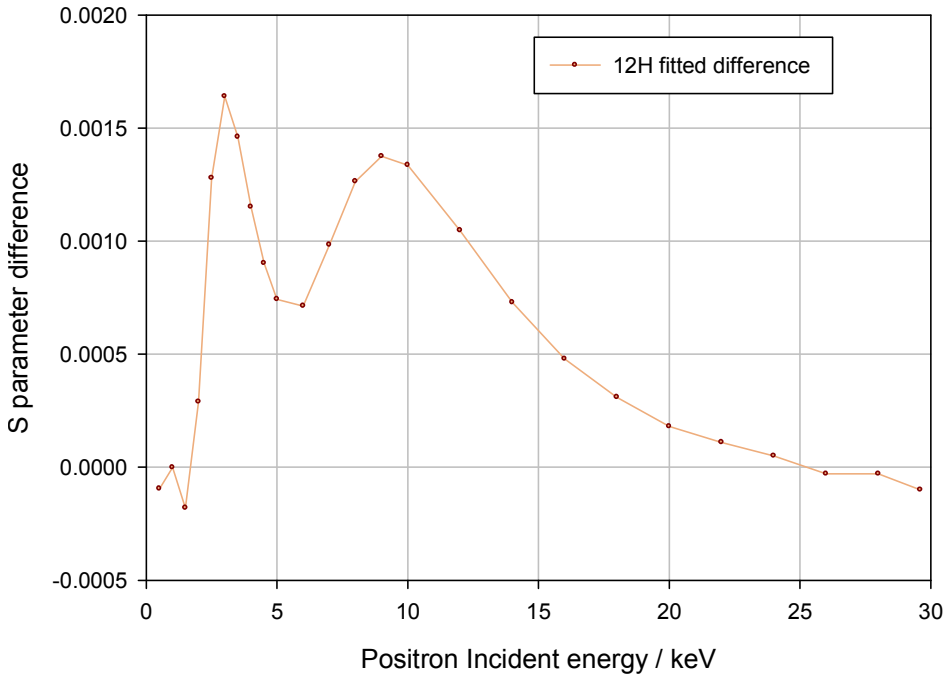

Figure 14: effect of light on sample 12H, a hydrogenated sample with Er3+ ions. This sample was also aged.

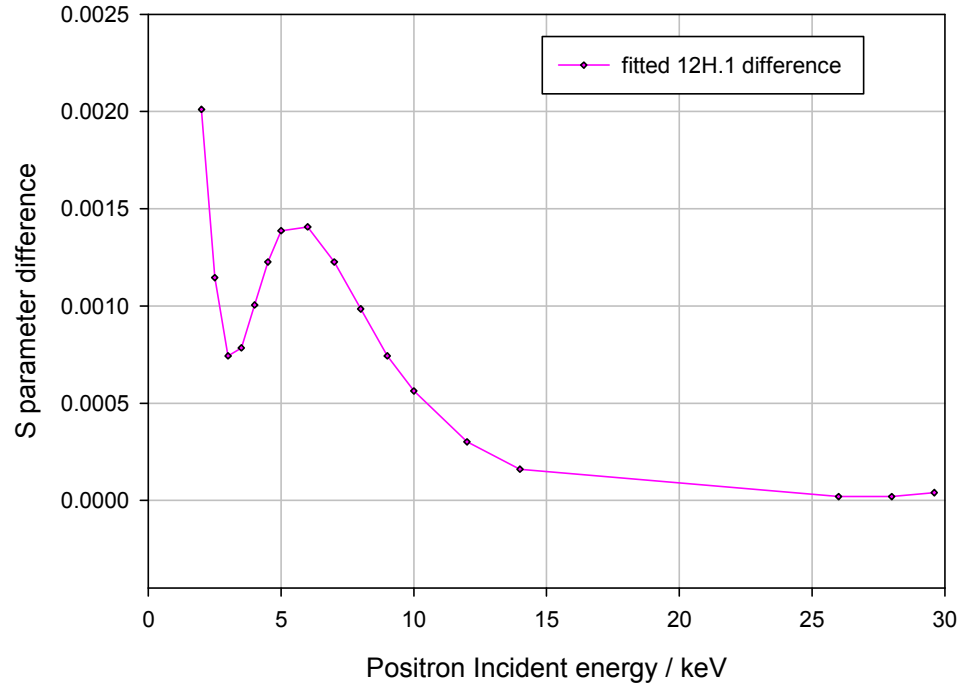

Figure 15: effect of light on sample 12H.1, a hydrogenated sample with Er^{3+} ions. This sample was aged but annealed in forming gas at 475 ºC for 15 minutes to re-introduce hydrogen.

The responses seen in figures 14and 15 above can be explained by:

- either the Er^{3+} ions shielding the nano-cluster interface from positrons creating an artificial dip in the S parameter increase when illuminated

- or by a quenching of the light effect by the Er^{3+} ions due to the energy transfer to them from the nano clusters.

In both cases, the Er^{3+} ions seem to have migrated towards the surface when the sample was annealed (12H.1).

4.2.5 Conclusions

VEPAS has here provided useful information about the evolution of silicon nanoclusters during the annealing of Si-rich silica. Although the detailed interpretation of the raw data may take more than one form - further experimentation may shed more light on the most likely model – it is clear that positrons are sensitive to the growth and defect structure of the nanocrystals.

The results for the experiments performed under constant illumination are encouraging. These show the ability of positrons to monitor the activity of electrons during the absorption of light. It also helps to elucidate the answer to the question as to whether the optical activity of silicon nanoclusters, and also the energy transfer from those nanoclusters to nearby Er ions, is done from the surface of the nanoclusters or its bulk. This can be proven to be very useful in the early days of silicon photonics and, maybe one day, photonic computers.

This section highlights the capabilities of VEPAS in studying the structure of semiconductors down to an atomic level. It also shows the versatility of the technique in studying minute changes in the electronic energy states induced by controlled variables such as the illumination of the samples.

4.3 VEPAS STUDIES OF Ar PLASMA TREATED TIO_2

4.3.1. Ar plasma treated TiO_2: Introduction

The State Key Laboratory of Silicon Materials and Department of Materials Science and Engineering, Zhejiang University provided samples to study with a slow positron beam. These samples had oxygen vacancies created in them in order to enhance their electroluminescence. [20]

Both thin (~ 100nm) and thick (~ 900 nm) TiO_2 films were prepared. The films were formed by thermal oxidation of Ti sputtered on to silicon at 500ºC in oxygen ambient for 5h. The samples were then treated by Ar plasma in PECVD. It has been reported that oxygen vacancies can be introduced by Ar plasma [21].

It is thought that the region affected by Ar plasma treatment may be within ~ 40 nm from the surface [20]. There were six samples:

Thin TiO_2 films (~ 100nm):

TiO2 1: non-treated

TiO2 2: Ar plasma: 30sccm, 300ºC, 50W, 1h

TiO2 3: Ar plasma: 100sccm, 300ºC, 50W, 1h

Thick TiO_2 films (~ 900nm):

TiO2 4: non-treated

TiO2 5: Ar plasma: 30sccm, 300ºC, 50W, 1h

TiO2 6: Ar plasma: 30sccm, 300ºC, 50W, 3h

[Note: sccm = standard cubic centimetres per minute (Ar flow rate).]

4.3.2. Experimental procedure and results

A pure bulk TiO_2 sample was obtained (from Goodfellow) [22] as a reference standard. The positron parameters *S* and *W* were measured as a function of incident positron energy. The data were all normalised to the parameter values for bulk Si, and selected data sets were fitted using the standard code VEPFIT.

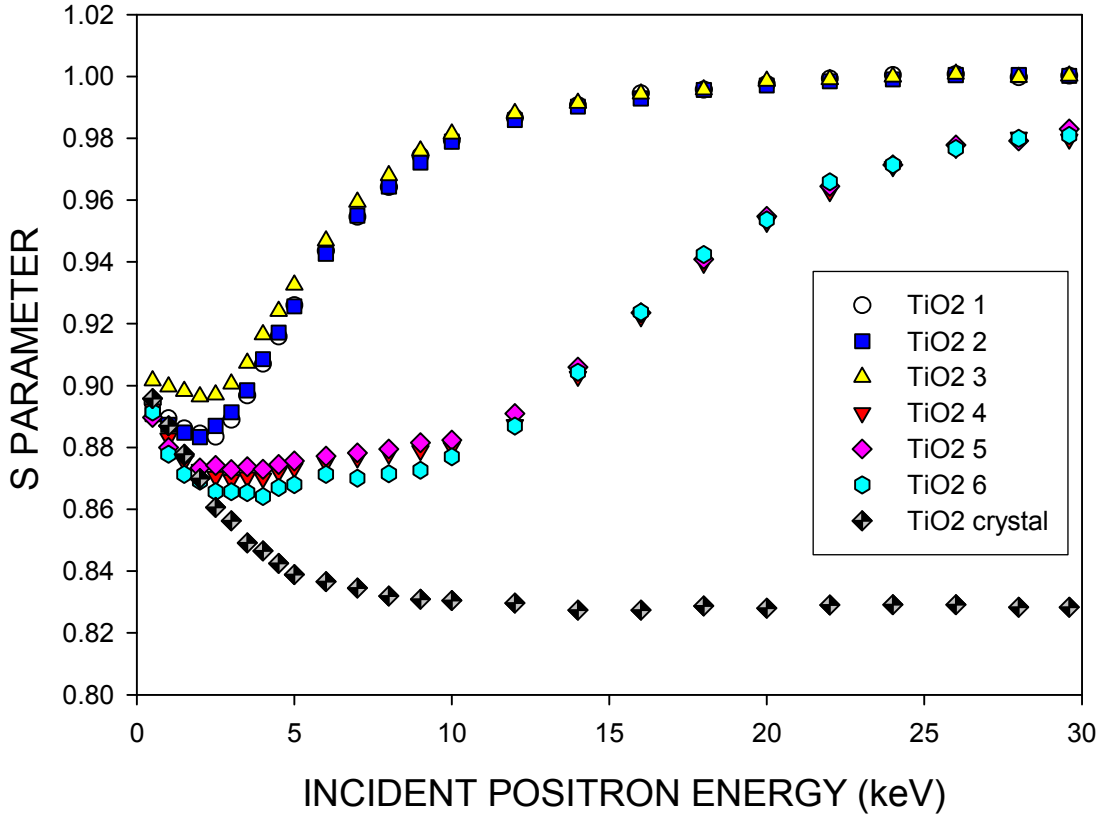

Figure 1: S parameter measurement of TiO_2 samples treated in Ar plasma

The difference between samples 1 and 3 seems real (data were reproducible). There is no convincing difference between data for samples 1 and 2, and for samples 4,5 and 6. It does appear that the 'film *S*' for sample 6 is a little lower than for samples 4 and 5, but across the whole film (ie not just the plasma-affected region), so this is either not real (and perhaps due to a normalisation problem – we do not measure directly the bulk substrate *S* value for samples 4,5 and 6) or the original film was slightly different before plasma treatment. It could be that the higher Ar flow rate was the significant variable for the treated samples – samples with the lower flow rate (30 sccm) showed similar data.

The fits are all acceptable, with the bulk Si positron diffusion length *L* fixed at 200nm, but the film thickness, layer *S* and *L* values were freely fitted. Fit results for samples 1, 3 and 4 are as follows (uncertainties shown are in last significant digits):

Sample		Layer thickness (nm)	Layer S	Layer L (nm)
1		78 (1)	0.8795 (2)	14 (1)
3		83 (2)	0.8950 (2)	12 (1)
4	layer 1:	150 (35)	0.8680 (2)	11(0.5)
	layer 2:	740 (25)	0.8790 (2)	Small – with large uncertainty
Bulk TiO2 crystal		n/a	0.8285 (2)	45 (2)

Table 1: Fitted values of S, layer thickness and diffusion length for samples 1, 3 and 4.

The data for samples 4,5 & 6 had to be fitted with two film layers (total thickness ~ 900nm), the first layer having a lower *S* value.

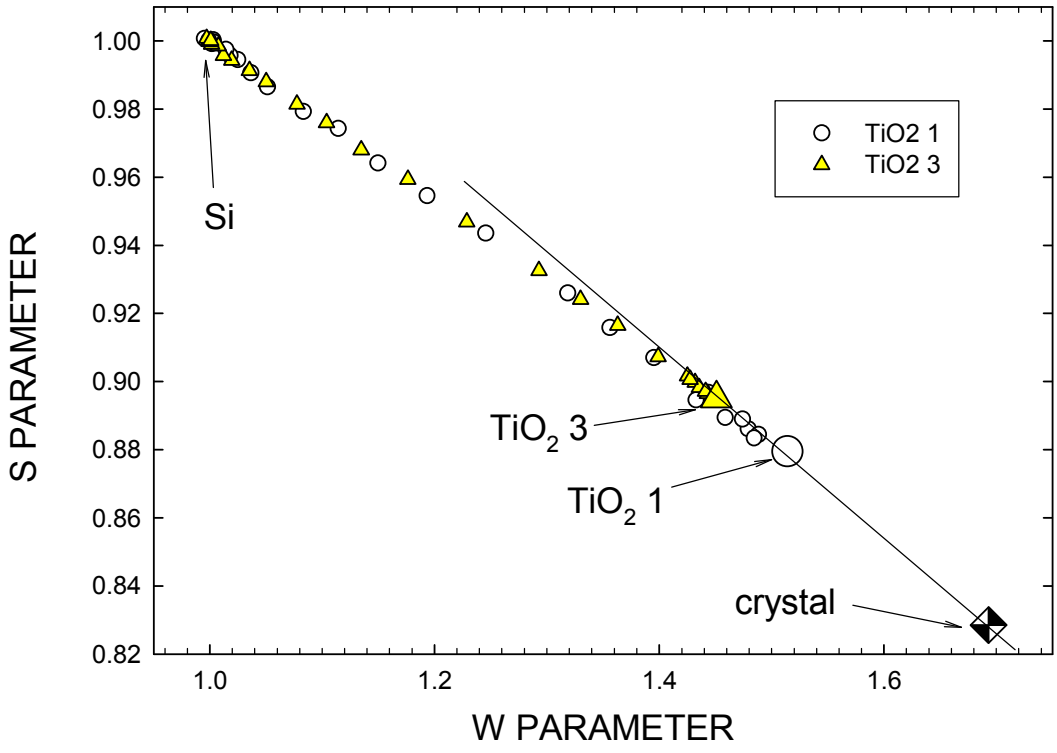

Figure 2: *S* parameter vs *W* parameter plot for samples 1 and 3, identifying different states.

The (*S,W*) points for the two films and for the bulk crystal are roughly on a line (see Figure 2). This suggests that both the as-grown film (sample 1) and the Ar-treated film (sample 3) contain defects of a similar type, at different concentrations. It is difficult to estimate any defect concentrations reliably, as we do not know the *S* (or *W*) values characteristic of the defects present in the films. Analysis based on diffusion length values is unreliable, especially as VEPFIT can yield a range of *S* and *L* values for a thin film. It also appears from the data that changes in the positron response are only seen for Ar plasma treatment at the higher flow rate (100 sccm) – very little which is conclusive is seen if the rate is 30 sccm.

4.3.3. Discussion and conclusions

The nature of any defects introduced by Ar plasma treatment is difficult to determine from VEPAS alone. However, it can be seen that the number of defects increases. It is found that oxygen vacancies are generated within a certain depth of TiO_2 films by the Ar-ion bombardment.

Usually when one introduces defects in an oxide, the *S* parameter decreases [23,24] (because of the oxygen electrons). However, if oxygen vacancies are introduced then perhaps the *S* can increase [25]. There is a small decrease in film *S* between samples 4 and 6, as opposed to the definite increase seen between samples 1 and 3. It is unclear why there appears to be two film qualities (ie two values of *S*) for the thicker films – i.e. between about 0-150nm and 150-900nm). It would therefore be useful to try to introduce even more damage so that saturation trapping is reached in the film.

VEPAS results have shown a correlation between the defects present and the electroluminescence measured with other techniques, and it is thought that the increase in the concentration of oxygen vacancies in TiO_2 films is responsible for the enhanced EL from the TiO_2/p^+-Si heterostructure-based devices.

4.4 POSITRON BEAM STUDIES OF HE IMPLANTED N-SI WAFERS

4.4.1. Very low energy He ion implantation: Introduction

Three samples were prepared (Table 1) by Varian Semiconductor Equipment Associates Inc [26], and have been studied by VEPAS in a short series of pilot measurements to evaluate the potential usefulness of the technique in characterising

the structure of such samples. The samples were expected to have very near-surface amorphised regions .

Sample	He implantation energy	Implantation dose
V1	1keV	10^{17} cm^{-2}
V2	2.5keV	10^{17} cm^{-2}
V3	7.5keV	10^{17} cm^{-2}

Table 1: He ion energies and doses for the three samples provided by Varian.

Varian provided TEM images of three similar samples, which are shown below. Also shown below in Figure 3 are the VEPAS measurements for the three samples.

The TEM image of sample V1 shows an amorphous layer with He bubbles extending from surface to depth of ~ 37nm, a transition layer which contains both amorphous and crystalline regions ~6nm thick, and a damaged but crystalline end-of-range region that extends ~10nm below the transition layer

The corresponding depths and thicknesses for samples V2 and V3 deduced from the TEM images are, respectively: 73, 20, 20nm, and 83, 73, 40 nm.

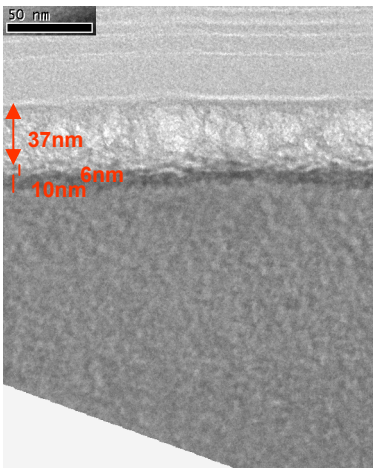

Image 1 a): TEM image of sample V1

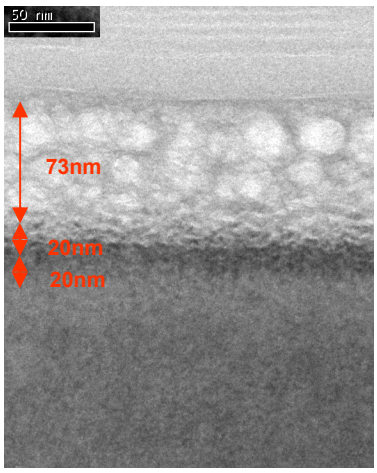

Image 1 b): TEM image of sample V2

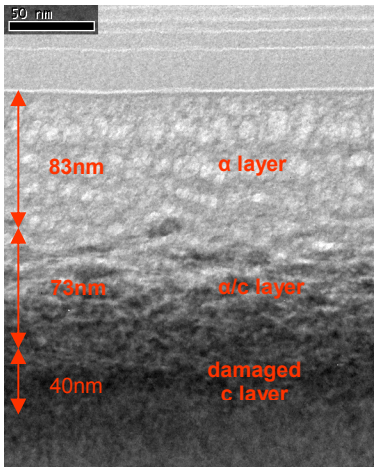

Image 1 c): TEM image of sample V3

4.4.2. Results, analysis and discussion

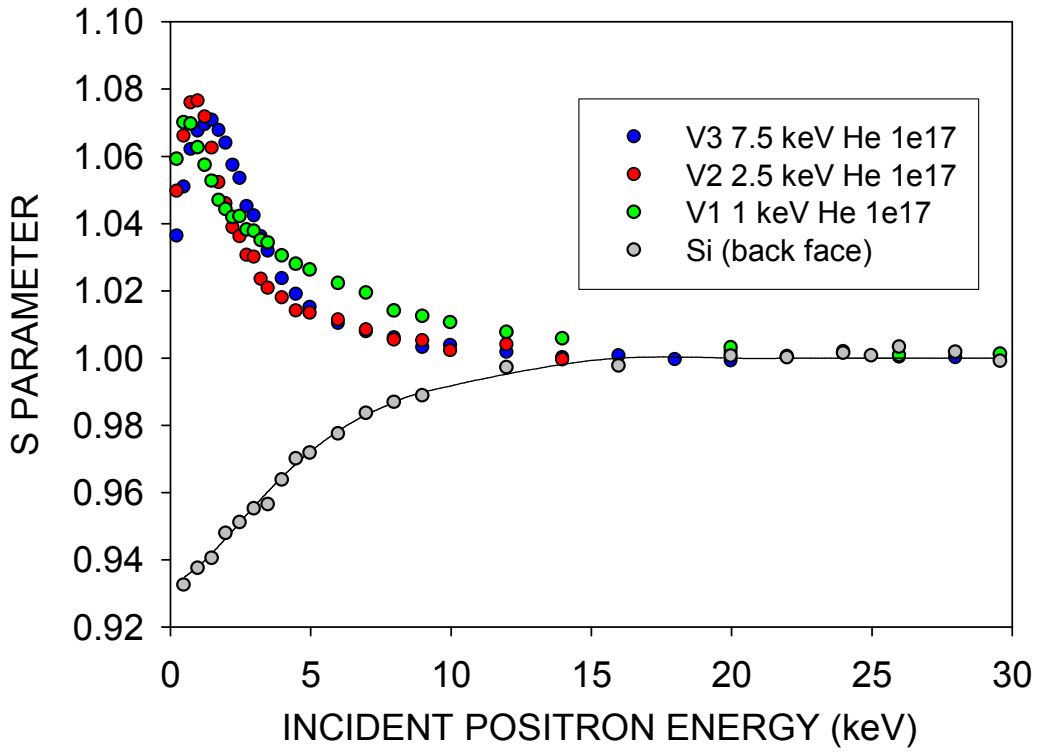

Figure 3: The *S* parameter of samples V1, V2 and V3 and a reference measurement of Si from the back side of the samples.

The TEM image of sample V1 shows an amorphous layer with He bubbles extending from surface to depth of ~ 37nm, a transition layer which contains both amorphous and crystalline regions ~6nm thick, and a damaged but crystalline end-of-range region that extends ~10nm below the transition layer

The corresponding depths and thicknesses for samples V2 and V3 deduced from the TEM images are, respectively: 73, 20, 20nm, and 83, 73, 40 nm.

The raw data (Fig. 3) has been fitted assuming the samples to have a layered structure using the standard code VEPFIT described in previous sections. It was found that none of the raw data could be fitted with a simple two-layer model (ie, amorphised layer with high *S* and underlying bulk Si with $S = 1$). Instead we have to have a thin highly-damaged layer, with $S \sim 1.07$, followed either by (a) a second damaged layer with $S \sim 1.01 - 1.03$, (b) a thin interface state (positron sink) with $S \sim$ 1.01-1.04, or (c), for the 1keV sample only, a second damaged layer with $S \sim 1.04$. The differences between positron responses for the three samples are clear from the raw data above; data points for the 1keV sample are higher than for the other two

samples in the 3-20keV region, even though the primary damage is in a thinner layer. This means that positrons are diffusing from the bulk Si to a region of higher *S* than is the case in the other two samples.

The results of fits were only deemed acceptable if *S* parameters and positron diffusion lengths in the layers were physically realistic, as well as requiring good χ^2.

1 keV He – sample V1

Three equally acceptable fits – A, B and C below - were obtained:

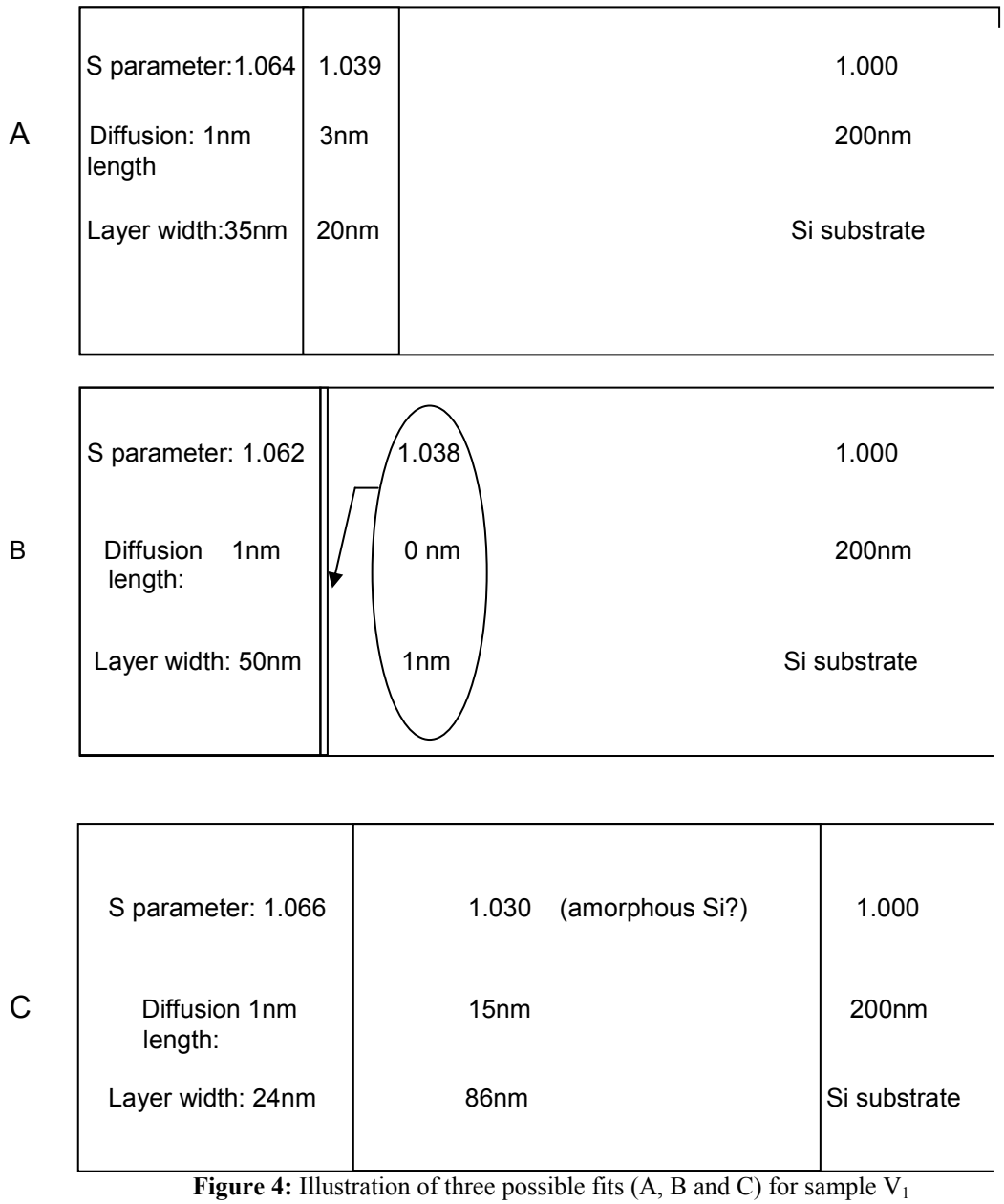

Figure 4: Illustration of three possible fits (A, B and C) for sample V_1

The high *S* values for the topmost layers are consistent with saturation trapping in vacancy clusters the size of hexavacancies. However, it is thought that large cavities of diameter ~ 10^1nm may look like silicon to positrons, as they are likely to be trapped on the internal 'clean' surfaces of such nanovoids. Therefore, this *S* value may be the result of a mixture of trapping in cavities (with $S \sim 1$) and smaller clusters (with *S* ranging from 1.04 to 1.13).

The second layer in fit A is consistent with saturation trapping in divacancies, or a mixture such as described above: in fit B a thin positron sink exists, and in fit C a thicker layer exists with an *S* value consistent with earlier measurements on amorphous Si.

2.5 keV He – sample V2

Two equally acceptable fits were obtained:

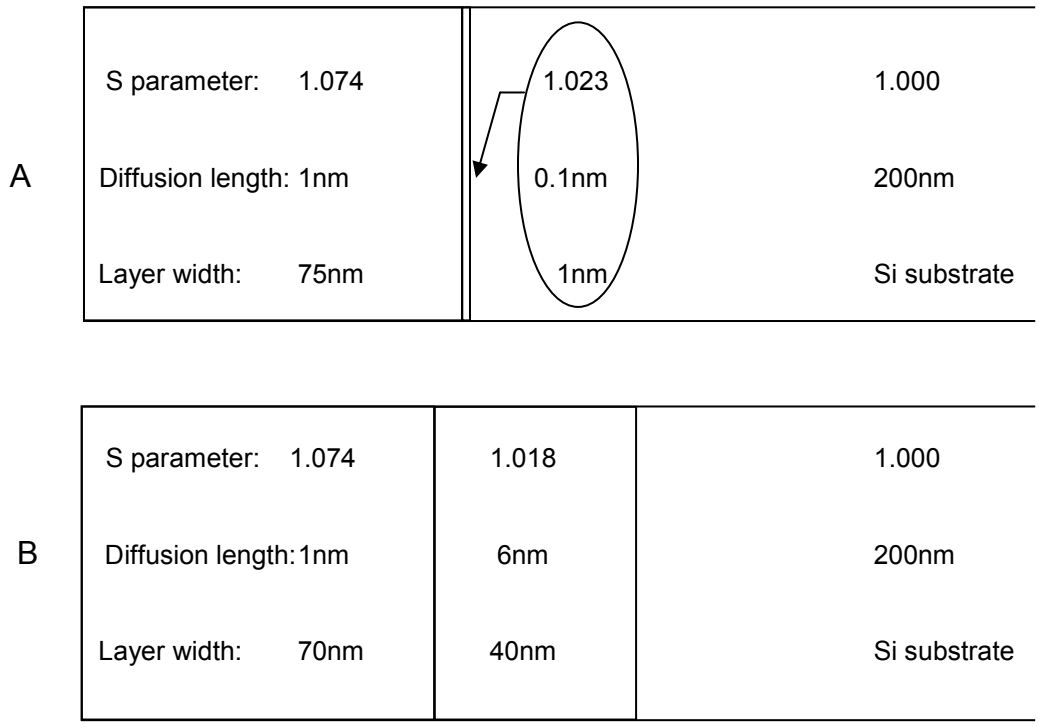

Figure 5: Illustration of 2 possible fits for sample V2

The high *S* values for the topmost layers indicate trapping in vacancy clusters and possibly cavities, as discussed for the 1keV sample.

The second layer in fit A is consistent with a thin positron sink, and in fit B a thicker layer with an *S* value which is not readily recognisable – if real, this must be due to a mixture of trapping as in the topmost layer, but in smaller clusters/cavities.

7.5 keV He – sample V3

Two equally acceptable fits were obtained:

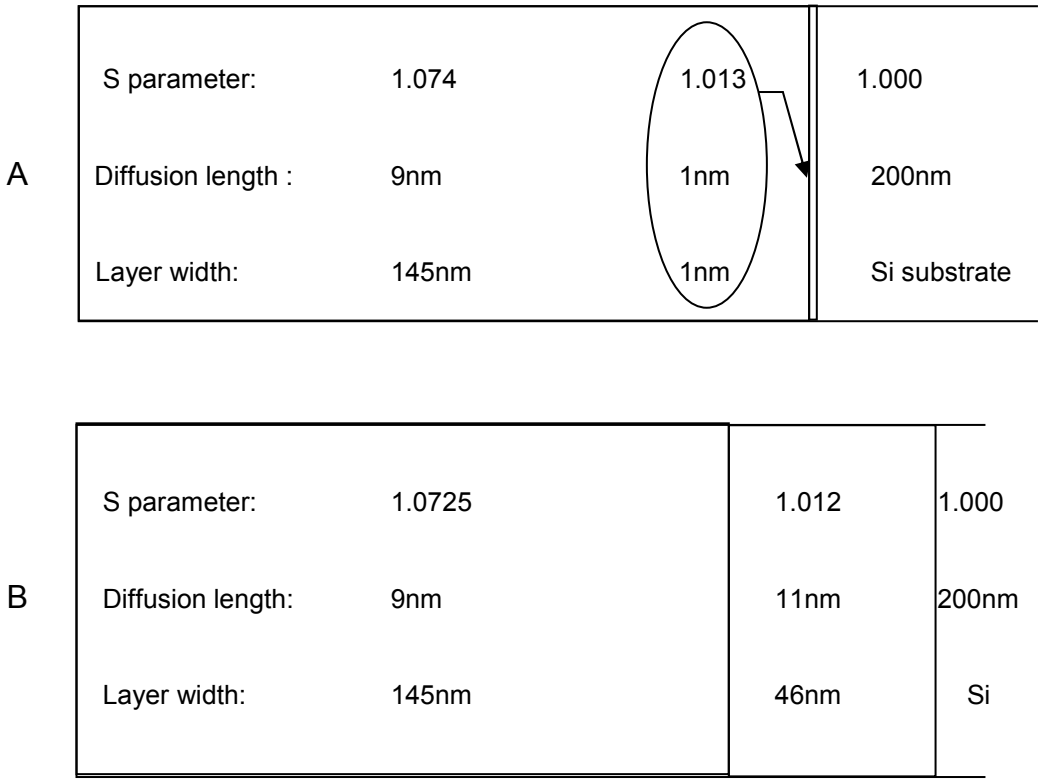

Figure 6: Illustration of two possible fits for sample V3

The high *S* values for the topmost layers indicate trapping in vacancy clusters and possibly cavities, as discussed for the 1keV sample. Remarks on the fit results for the second layers in fits A and B are as for the 2.5keV sample.

The layer thicknesses obtained from the fitting procedure should be taken as indications rather than absolute accurate values. The most appropriate positron implantation profiles have been used. Data for all three samples can be fitted with a thin interface which is a perfect positron sink. However, the *S* parameter characteristic of these interfaces is different in each case – which is not very convincing. The data can also be fitted using a 20-40nm-thick second layer – but, as for the thin interface, the *S* parameters for these layers have to be different for each

sample. In this case, however, this could be explained by a different mix of cluster sizes (going from larger to smaller from 1 to 7.5keV implants). The 1keV sample is the only one for which a good fit could be obtained with a substantial second layer with characteristics consistent with previous measurements of amorphous silicon. Nevertheless it seems that neither of the VEPFIT fittings agrees with the TEM studies of the samples. A possible explanation for this is that VEPAS is sensitive to different sample features than TEM, i.e. different sized pores and vacancies.

4.4.3. Very high energy He ion implantation –samples from McMaster University

High-energy (3 and 10 MeV) He-implanted Si samples were provided by McMaster University, Hamilton, Canada [27], to be investigated by VEPAS. The aim was to see if positrons can observe an effect on the damage distribution in Si due to the spatial separation of interstitials and vacancies (i.e., the existence of vacancy-rich and interstitial-rich regions).

4.4.4. Results

The results were again fitted using VEPFIT and are plotted on figure 7.

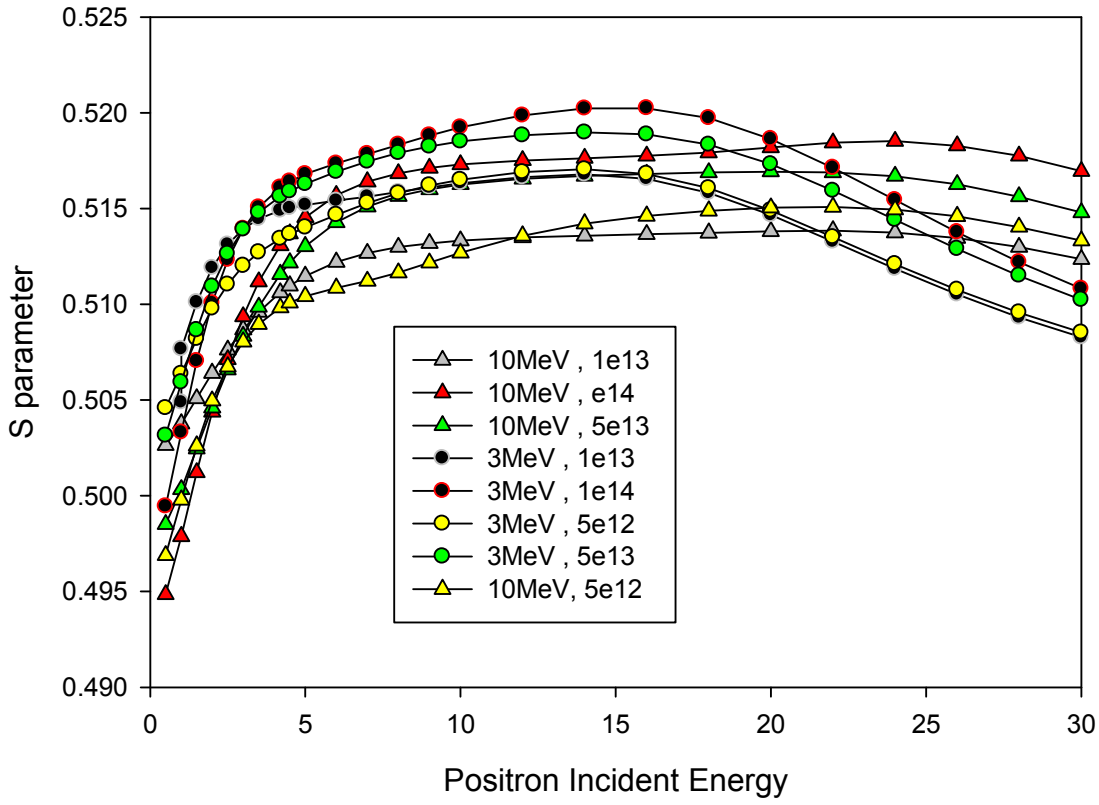

Figure 7: *S* parameter plot for He implanted Si samples at different energies and different implantation doses.

The numerical values of the fits are shown in table 2 below.

He ion dose (cm^{-2})	Energy (MeV)	Layer 2			Layer 3		
		S	*L*(nm)	Layer Width(nm)	*S*	*L*(nm)	Layer Width (nm)
5e12	3	0.515	58	500	0.518	40	3000
	10	0.511	50	3500	0.515	40	6000
1e13	3	0.516	36	700	0.517	30	3000
	10	0.514	106	3500	0.515	40	6000
5e13	3	0.517	50	500	0.519	30	3300
	10	0.516	111	3500	0.517	41	6000
1e14	3	0.518	36	700	0.521	30	3300
	10	0.517	80	3500	0.521	50	6000

Table 2: Parameter values from VEPFIT for the He implanted Si samples: He ion dose and energy and given in the first two columns

The results of these fits listed in table 2 above can be summarised as follows:

1) The deeper boundaries are more or less the same, affected only slightly by the ion dose at 3MeV (the higher the dose the deeper the boundary is, 3000 to 3300nm). The first layer boundaries range between 500nm and 700nm for 3MeV ions.

2) The *S* parameter increases with ion dose and decreases with ion energy in both layers, and it is always higher in the second layer.

3) The positron diffusion length *L* is a less reliable VEPFIT parameter since at near saturation trapping it can be given a wide range of values without changing the goodness of fit measurably. However, note that the second layer has always a lower diffusion than the first one.

4.4.5. Conclusions

Conclusions from the MeV He data fitting are that:

1) The range of depths over which the damage is observed is consistent for all samples:
2) The *S* parameter increases with ion dose as the vacancy-type damage concentration increases, and it reaches saturation at about 0.521 (4%

higher than silicon) – characteristic of the di-vacancy. It is lower for 10MeV He ions since the damage is spread further and the defect concentration is lower.

3) The peak in vacancy damage concentration at deeper depths was represented by the higher *S* value in the second layer, which reached saturation trapping values of 1.04 only for the two samples implanted with 10^{14} ions cm^{-2}.

4.5. SILICON NANOCLUSTERS IN SILICON NITRIDE LAYERS: THE EFFECT OF SILICON CONCENTRATION

4.5.1. Si rich SiN: Introduction

This section describes the structural evolution of Si rich SiN samples at different annealing temperatures. The purpose of this is to find a correlation, if any, between the structure of the samples and their optical properties, e.g. photoluminescence. Sample specifications are shown in Table 1; T016 and T018 represent silicon rich silicon nitride (SRSN) films with low and high excess silicon concentrations respectively, while T023 has an intermediate composition. Likewise, TFNH3-14 and SRSN5 have low excess Si concentrations while TFNH3-12 and SRSN4 have high excess Si concentrations. Annealing was performed for 60 min in a quartz tube furnace or in a Rapid Thermal Annealer for 30s.

Optical measurements performed at McMaster University [27] show that the emissions from all SRSN films follow the general trend of red-shifting with higher Si content, which is an expected result of the average silicon nanocluster diameter increasing [28]. The most intense emissions are usually from films annealed at low temperatures, peaking at ~600ºC in high excess Si samples and ~800ºC in low excess Si samples. The reason for the decay in intensity at higher temperatures is uncertain, so analysis of defects as a function annealing temperature could provide some important insight.

TFNH3-07 is an interesting sample since RBS [29] suggests it is a slightly nitrogen-rich silicon nitride film and its PL properties do not follow the trends observed in the

SRSN samples. Instead, it has no PL until ~1000ºC when it abruptly becomes highly intense around 510nm and then decays at higher temperatures. It is believed that this emission is through a defect level and its x-ray absorption spectra show a large peak at the N K-edge.

VEPAS measurements were made on all the samples, and VEPFIT fits to the normalised raw data are presented in Figs. 5-11 below.

Sample	Film Type	Ann. Temps (ºC)	Growth Technique	Thickness (Å)
TFNH3-07	NRSN	700 - 1100 (N_2)	PECVD	~2500
TFNH3-12	SRSN	600 – 1100 (NH) 700 (N_2) 700 (N_2) RTA	PECVD	2222
TFNH3-14	SRSN	600 – 1000 (NH)	PECVD	2573
T016	SRSN	700 – 1100 (NH)	ICP CVD	3004
T018	SRSN	700 – 1100 (NH)	ICP CVD	2487
T023	SRSN	N/A	ICP CVD	2503
T025	SRSN	N/A	ICP CVD	20001
T026	SRSN	N/A	ICP CVD	20021
T031	SRSN	N/A	ICP CVD	20048
SRSN4	SRSN	N/A	ECR PECVD	1195
SRSN5	SRSN	N/A	ECR PECVD	792
Tb012	Tb doped SRSO	1200	unknown	~1000
Tb016	Tb doped ORSO	700	unknown	~1000

Table 4.1. List of Si-rich SiN samples (with two SiO_2 samples) grown by CVD (chemical vapour deposition) and subjected to different annealing regimes. SRSN = Si-rich SiN: SRSO = Si-rich SiO_2: NRSN = N-rich SiN: ORSO = O-rich SiO_2. NH = forming gas (95% N2, 5% H_2). RTA = rapid thermal annealing. PE = plasma-enhanced: ICP = inductively-coupled: ECR = electron cyclotron resonance.

4.5.2. Results and discussion

PECVD-grown samples

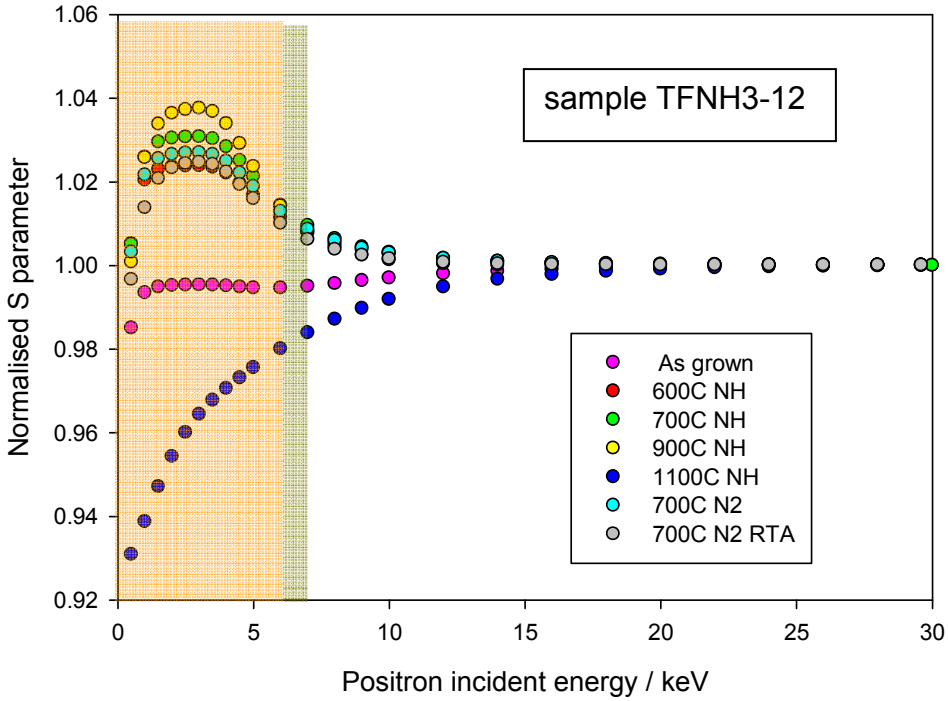

Figure 8: Sample TFNH3-12 after annealing at different temperatures in different gases. The orange band represents the SiN film (mean positron depth at 6keV = film thickness) and the green band an interface state between film and substrate (see text).

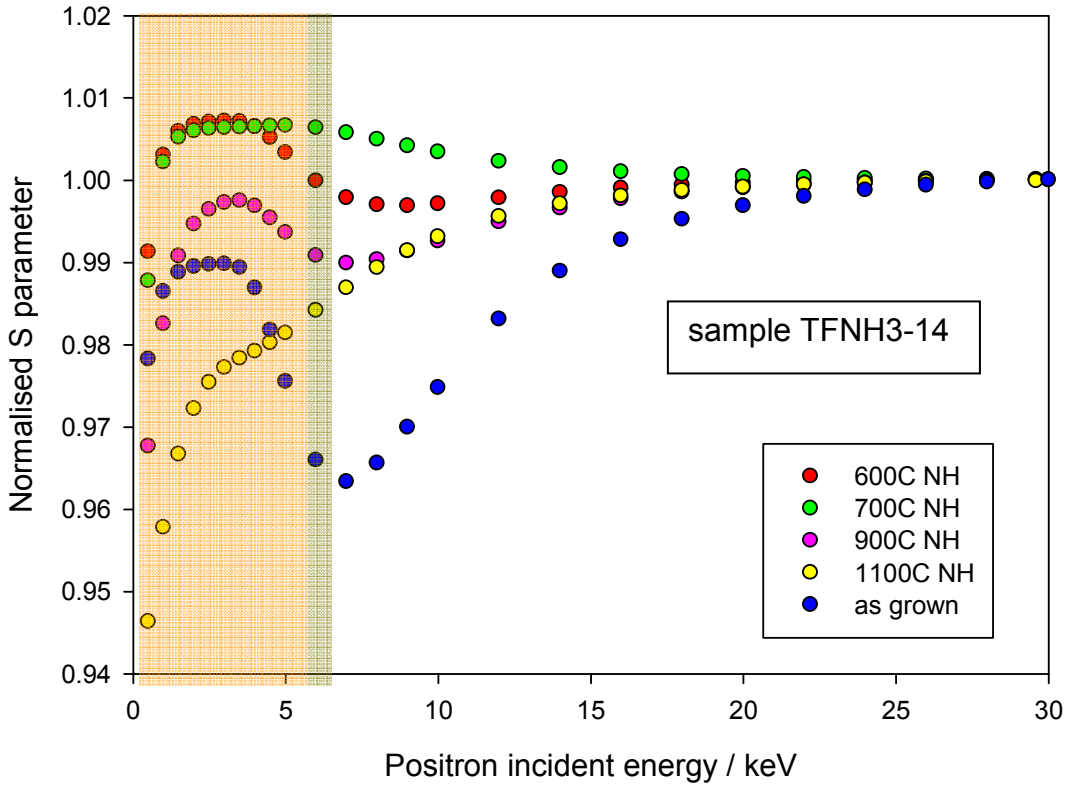

Figure 9: Sample TFNH3-14 after annealing at different temperatures: coloured bands – as for Fig. 1.

The families of samples shown in Figures 8 and 9 are grown similarly with different concentrations of excess silicon. They consist of a near surface Si rich SiN film (SRSN) on a SiN substrate.

- Si rich SiN film (~220nm-250nm): This layer has a small response to positrons in its "as grown" state, and the strength of the response is directly correlated to the concentration of excess silicon. The positron response changes with annealing temperature (as excess silicon agglomerates), increasing the *S* parameter for up to 900ºC for high Si concentration and 700ºC for low concentration. At 1100ºC the layer seems to undergo a significant structural change, probably associated with the interface around the agglomerated Si nanoclusters. The nanocluster interface-related vacancies are believed to be annealed away. The time of annealing seems to have little effect, as evidenced by the data for the rapid-thermally-annealed (RTA) sample at 700ºC.

- SiN-Si bulk interface state: This is a thin interface state (~5nm-10nm) most probably with oxygen present. The positron response to the interface appears to diminish with annealing and becomes overshadowed by the increase of the *S* parameter in the first layer. When the *S* parameter for the SRSN layer falls at high annealing temperatures, remnants of the interface response can still be seen.

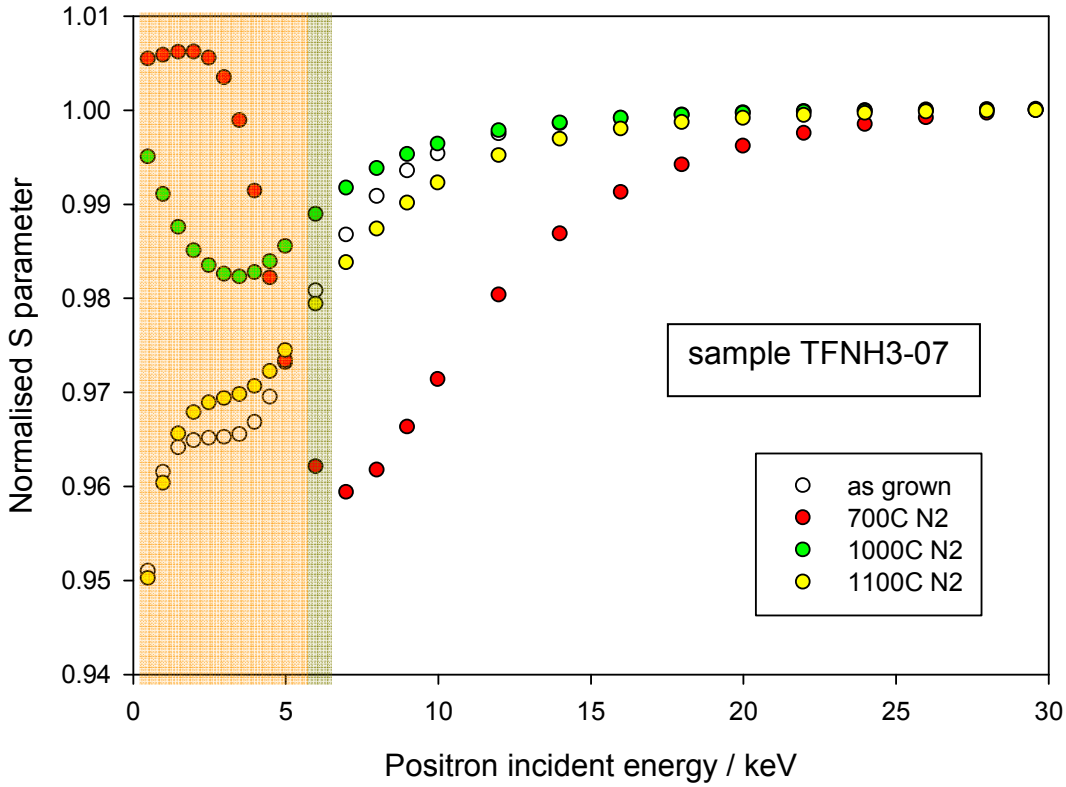

Figure 10: Sample TFNH3-07 at different annealing temperatures

The family of samples represented in Figure 10 has a nitrogen rich layer at the surface. For the as-grown sample the layer *S* is low. When annealed at 700ºC, the samples' layer *S* parameter increases, suggesting an agglomeration of silicon atoms even in a nitrogen-rich environment. There is also the appearance of an interface state probably created by the movement of the Si atoms, revealing a coarser interface. At 1000ºC the decrease in the layer *S* parameter can be explained by the slight evaporation of near-surface nitrogen (also seen as spots on the sample surface) and the interface state begins to go away. The 1100ºC annealed sample has more and bigger spots on the surface suggesting more severe nitrogen evaporation. Oxidization of the pores left behind by evaporated nitrogen is also considered since the surface *S* parameter drops. Nitrogen evaporation could also explain the appearance of photoluminescence after 1000ºC.

ICP CVD-grown samples

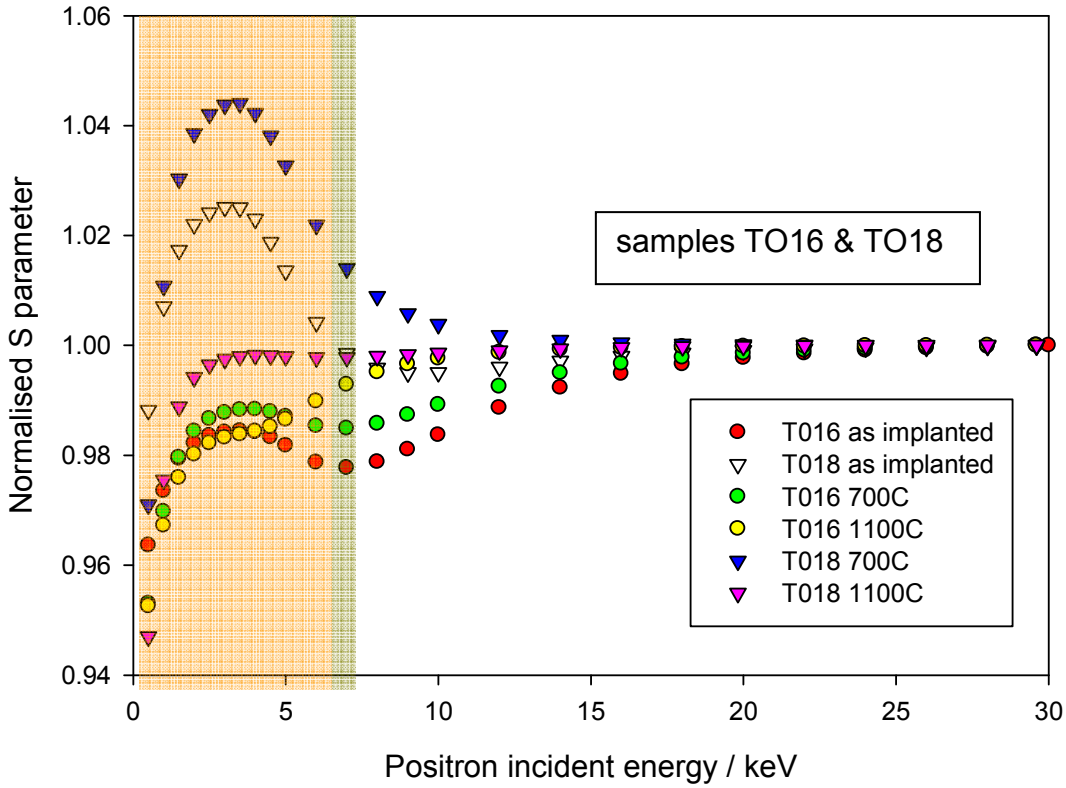

Figure 11: Samples T016 and T018 after annealing at different temperatures in NH. Coloured bands – SiN and interface layers (see text).

Si rich SiN layer: Here we can clearly see the direct effect of excess Si concentration on the *S* parameter as well as the effect of annealing. At higher concentrations there is more damage in the layer. For the as- grown samples the damaged layer can be clearly seen via the increased S at 700ºC, as excess silicon agglomerates and more vacancies surround the nanoclusters. At 1100ºC the *S* parameter drops significantly, depending on the initial Si concentration. The response is similar to the one of TFNH3 samples.

SiN – Si bulk interface layer: The layer is not obvious in the high concentration samples (due to the high *S* in the damaged layer) but it is there when the data are fitted. The positron response to the interface partially diminishes at 700ºC and almost completely disappears at 1100ºC. The growth technique (ICP CVD) does not seem to affect the structure of the samples in a way positrons can detect.

ICP CVD as-grown samples

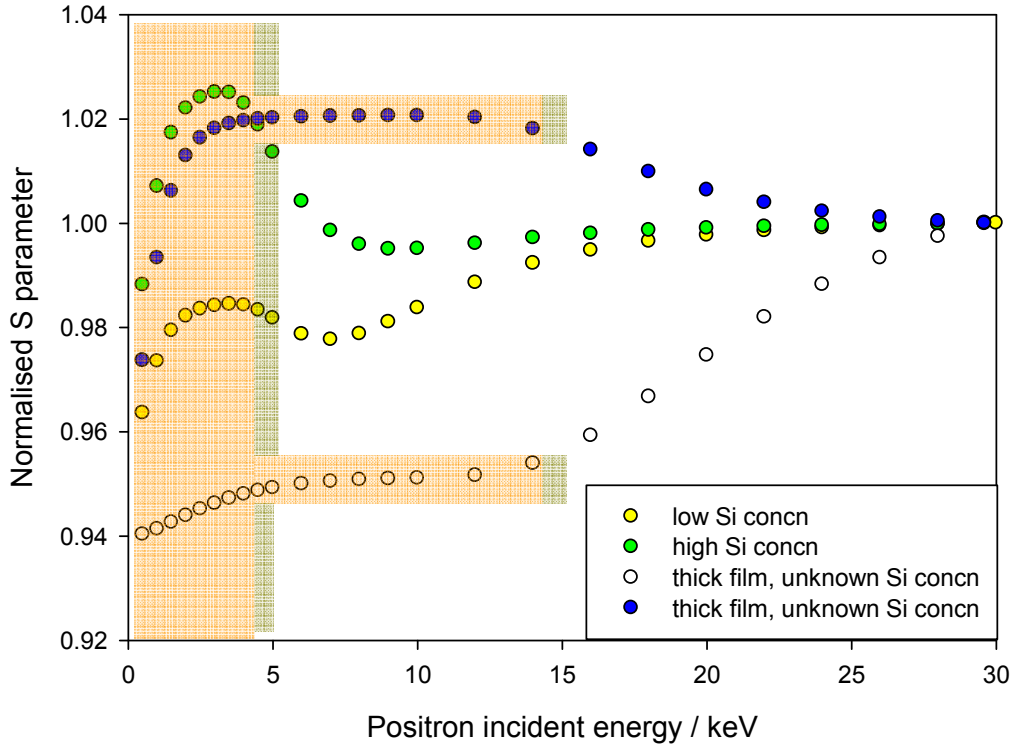

Figure 12: As-grown samples TO16,18,26 & 31 (yellow, green, blue & white symbols).

Si rich SiN film (~250nm-300nm / 2 μm). Similarly to previous sample families the *S* parameter seems to be correlated to the concentration of excess silicon. The higher the Si concentration, the more vacancies hence, the S parameter is higher. The thicker film samples with unknown Si concentration reveal nothing significant, but it may be assumed that sample TO31 has a significantly lower excess Si concentration than TO26.

The (5nm) SiN- Si bulk interface state seems to be present in all samples even though it is not clearly seen in the thicker ones, mainly due to the very broad implantation profile of the positrons at those depths (leading to reduced sensitivity).

Si- and O-rich Tb-doped SiO_2 samples

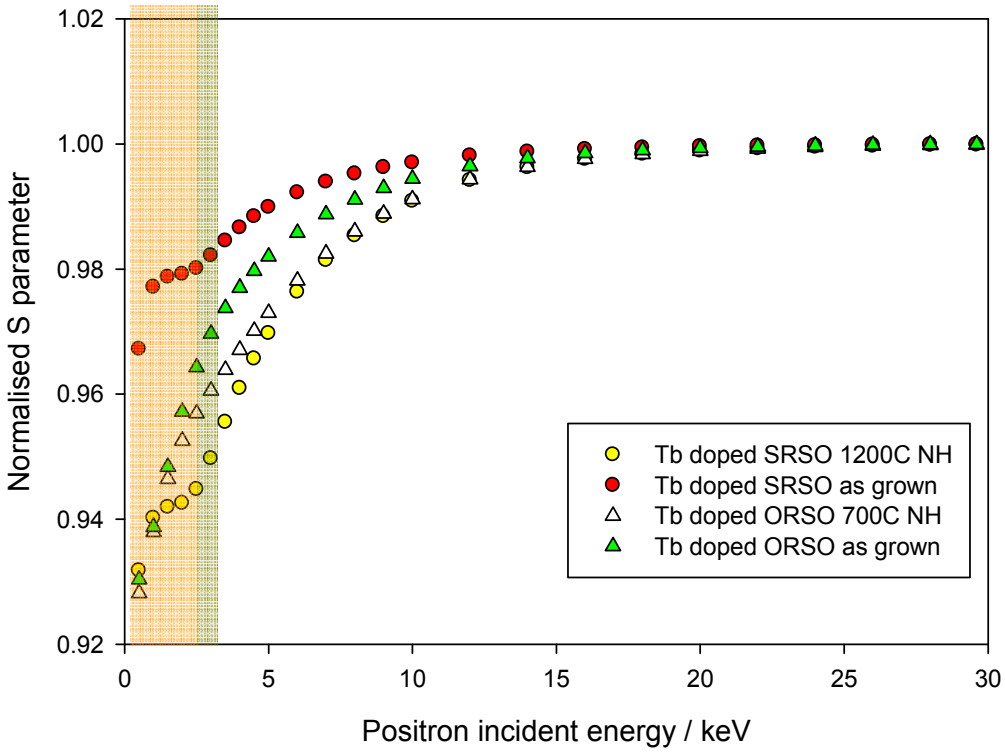

Figure 13: Samples Tb012 (SRSO) and Tb016 (ORSO) before and after annealing.

Si/O rich SiO_2 layer (~100nm): In the case of excess Si there is response of positrons to the damage around the excess Si. The *S* parameter decreases after annealing in forming gas (95% N_2-5% H_2), suggesting vacancy passivation by H, allowing a more SiO_2-like positron response. O-rich layers only seem to have an effect on the diffusion of the positrons; the diffusion length increases after annealing the sample in forming gas. Vacancy passivation by H could again explain this.

Si_xO_y – interface state (5nm): there is not a very strong positron response from this layer, a narrow interface with an *S* parameter similar to Si and an effective diffusion length of almost 0 nm.

ECR PECVD samples

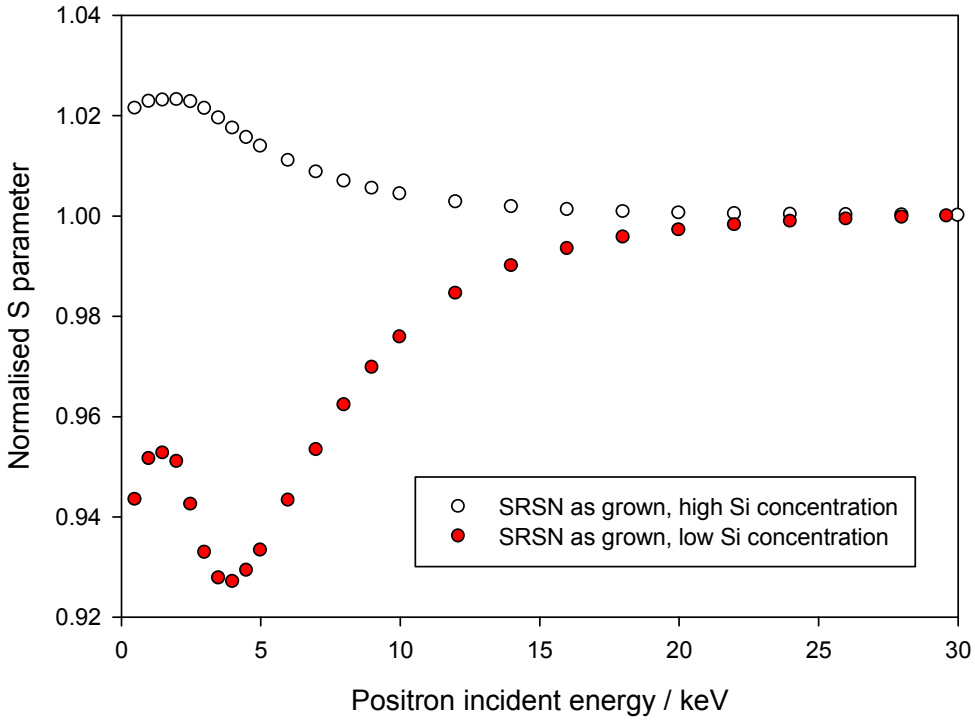

Figure 14: Samples SRSN 4 and 5, as-grown.

The fitted data for these two samples do not reveal anything significant other than verifying that the positron response to the film is again related to the excess Si concentration. The different growth technique does not appear to lead to any measurable differences to the structure of the sample.

4.5.3. Si-rich SiN layers: Conclusions

In general, the number of defects seems to be correlated to the concentration of excess silicon. More silicon means more nanoclusters, therefore more open volume area around them. All samples see an increase in S parameter when annealed to up to ~700ºC (900ºC for TFNH3-12), explained by the agglomeration of excess silicon into larger clusters creating more defects (damaged SiN has a higher *S* parameter). When annealed at 1100ºC there is an uncertainty as to the nature of the structural change, but the drop in *S* parameter would indicate a drop in the defect concentration - i.e., they are annealed away. Therefore the peak of PL seen at annealing at ~600ºC for high concentration and ~800ºC for low would not be linked to the number of defects as much as the size of the nanoclusters (smaller concentration would need a higher annealing temperature to reach the same size of nanoclusters).

In the nitrogen rich samples it is believed that Si atoms still agglomerate but at into smaller structures, having excess nitrogen effectively capping the size of the nanoclusters. Photoluminescence occurs at the same temperature at which nitrogen is thought to be evaporated, allowing Si atoms to move more freely creating larger nanoclusters. If nitrogen is indeed being removed, the open volume surfaces could be oxidised when the sample is brought into air, explaining the *S* parameter behaviour.

A growth technique comparison shows no significant differences. All techniques have similar outcomes and the samples evolve in an analogous manner.

The appearance of the interface can be explained by Landheer *et al* [30,31]. It is a thin damaged oxide layer that can be annealed away. Collaborators in McMaster University [27] believe that the formation of open volumes and their increase with annealing temperature is explained by hydrogen escaping the samples during annealing. This would also explain the decrease in photoluminescence they [27] have observed. It has also been suggested that ECR PECVD, ICP CVD and TFNH3-07 samples behave differently as they are not silicon rich films and do not form open volumes in the same way since they have a more stoichiometric composition.

4.6 VACANCY AND INTERSTITIAL SEPARATION IN SILICON ON INSULATOR (SOI) SAMPLES

4.6.1 Introduction to Vacancy and Interstitial separation in SOI samples

SOI samples were investigated in collaboration with the Department of Engineering Physics, McMaster University, Canada (Dr. A. P. Knights): Surrey Ion Beam Centre, University of Surrey, UK (Si implantation): and the School of Electrical and Electronic Engineering, The University of Manchester, UK (optical measurements).

The samples were created using the Smartcut® [32] process, in which a twin oxide-covered Si layer is removed from the substrate, inverted and bonded to a clean Si surface. This creates a buried oxide layer. The samples were then implanted with high energy Si ions, damaging the first silicon layer and the oxide layer and then being buried into the bulk. This would create lattice vacancies in the top layer and interstitials in the bulk, unable to recombine do to the oxide layer between them. Annealing the samples at different temperatures would allow the vacancies to cluster,

forming larger multi-vacancies that would then be studied with positrons. The list of samples is given below:

	Annealing temperature
SOI as_imp	N/A
SOI 300	300 ^{0}C
SOI 400	400 ^{0}C
SOI 500	500 ^{0}C
SOI 600	600 ^{0}C
SOI 700	700 ^{0}C

Table 1: List of SOI samples

4.6.2 Results for SOI samples

Results of the raw data and the VEPFIT fit is shown below (Figure 15)

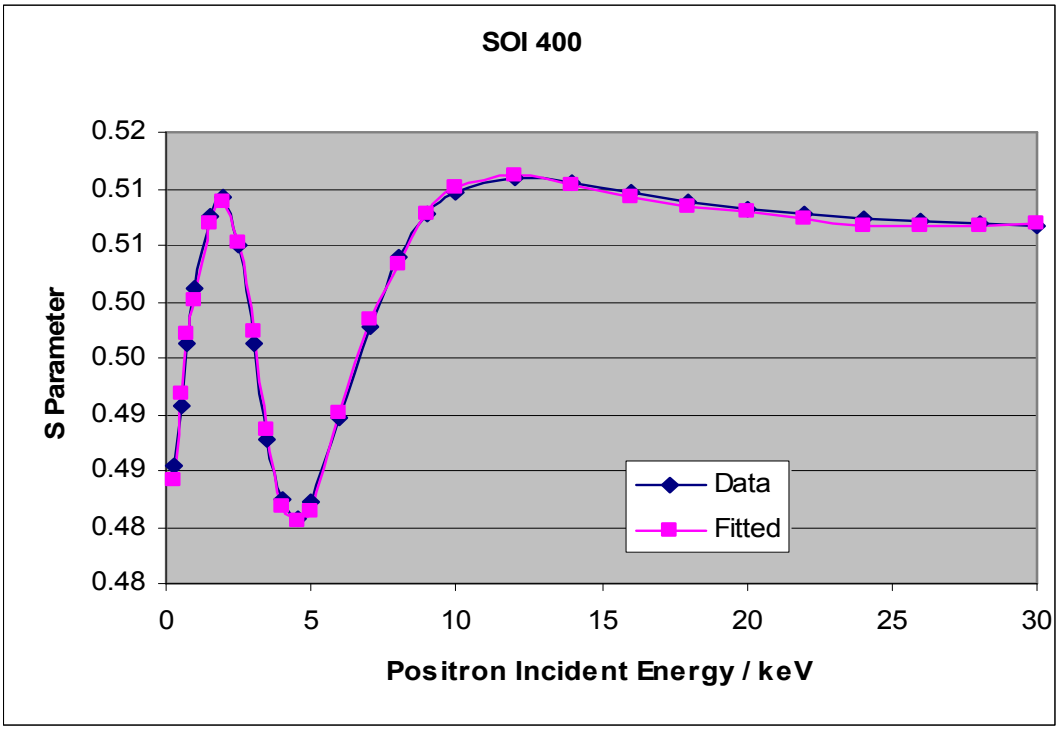

Figure 15: Sample SOI400 as measured and as fitted with VEPFIT

The fitting process was repeated for the entire family of the SOI samples and fitted parameters *S* and the diffusion length *L* for each layer are shown below.

	Layer 1 (140nm)		Layer 2 (280nm)		Layer 3 (783nm)		Layer 4 (bulk)	
	S	L(nm)	S	L(nm)	S	L(nm)	S	L(nm)
SOI as imp	0.520	17.9	0.448	3	0.528	72.5	0.506	280
SOI 300	0.517	20.2	0.453	3	0.528	85.2	0.506	280
SOI 400	0.516	19.1	0.457	3	0.528	84.5	0.506	280
SOI 500	0.517	25.8	0.464	3	0.527	101	0.506	280
SOI 600	0.516	32.7	0.482	3	0.526	112	0.506	280
SOI 700	0.513	34.5	0.493	3	0.520	76.1	0.506	280

Table 2: SOI samples as fitted by VEPFIT, highlighted numbers being the ones fitted.

4.6.3 Discussion on SOI samples

We can see a significant change of *S* occurring in Layer 3 after annealing above 600ºC, assuming that that is when di-vacancies start to move away. It is also interesting that this fitted family shows no saturation in Layer 1 (this can also be explained that VEPFIT prefers to fit *L* instead of *S*, decreasing the value of *L* where *S* could have been increased instead). The definite result from this is that with annealing *S* decreases and *L* increases with an inverse correlation. Good fits can occur over a range of values of the two variables, not allowing a very precise result. If the layers were thicker, making our measurements less susceptible to *L* changes, then *S* could have been more unambiguously determined.

4.7. SUMMARY

Although this chapter has covered a number of different types of samples, they all involved the study of the evolution and behaviour of vacancy-type defects. It has been shown successfully that VEPAS excels in revealing information that can be empirically interpreted in order to study vacancies, pores and the lattice structure of materials. The technique can be applied to almost any semiconducting material that has been grown and treated in a number of different ways from any CVD technique to plasma treated samples. The results of many of the experiments described in this chapter have either been published (see Appendix) or are in the process of being prepared for publication.

CHAPTER 4 REFERENCES

[1] A. P. Knights, P.G. Coleman, "Sensitivity of Positron Annihilation Spectroscopy to Energy Contamination in Low Energy Boron Ion Implantation", Mat. Sci. Forum **445 - 446**, 123 (2004).

[2] P.G. Coleman, "Defect profiles in semiconductor structures", Phys. Stat. Solidi, **4**, 3620 (2007).

[3] D.V. Lang, "Deep level transient spectroscopy: A new method to characterise traps in semiconductors", J. Appl. Phys. **45**, 3023 (1974).

[4] J.H. Evans-Freeman, P.Y.Y. Kan, N. Abdelgader, "High resolution deep level transient spectroscopy studies of the vacancy-oxygen and related defects in ion-implanted silicon", J. Appl. Phys. **92**, 3755 (2002).

[5] S.A. Al'Tshuler and B.M. Kozyrev, "Electron Paramagnetic Resonance" (Academic Press, 1964).

[6] G. D. Watkins and J. W. Corbett, "Defects in Irradiated Silicon. I. Electron Spin Resonance of the Si-*A* Center", Phys. Rev. **121**, 1001 (1961).

[7] S. Horiachi, "Fundamentals of High-Resolution Transmission ElectronMicroscopy", (North_Holland, Amsterdam 1994).

[8] B. E. Warren, "X ray Diffraction" (Addison-Wesley,1969).

[9] S.K. Sinha, E.B.Sirota, S Garoff, H.B. Stanley, "Xray and neutron scattering from rough surfaces", Phys Rev B **38**, 2297 (1988).

[10] Richard J Colton, David R Baselt, Yves F Dufrêne, John-Bruce D Green and Gil U Lee, "Scanning Probe Microscopy", Current Opinion in Chemical Biology **1**, 370 (1977).

[11] GT Reed, AP Knights, "Silicon Photonics: The State of the Art", Wiley Online Library (2008).

[12] F. T. Vasko, Alex V. Kuznetsov, "*Electronic states and optical transitions in semiconductor heterostructures*" (Springer-Verlag, 1999).

[13] K.G. Lynn, D.O. Welch, J. Throwe, B. Nielsen, "Interface studies using variable energy positron beams", Int. Mat. Rev. **36**, 1 (1991).

[14] Samples provided by Dr. A.P. Knights, Department of Engineering Physics, McMaster University, Canada L8S 4L7.

[15] J.F. Ziegler, M.D. Ziegler and J.P. Biersack, Nucl. Instrum. Methods B **268**, 1818 (2010).

[16] C. E. Chryssou, A. J. Kenyon, T. S. Iwayama, C. W. Pitt, and D. E. Hole, "Evidence of energy coupling between Si nanocrystals and Er^{3+} in ion-implanted silica thin films", Appl. Phys. Lett. **75**, 2011 (1999).
[17] Se-Young Seo and Jung H. Shin, "Exciton–erbium coupling and the excitation dynamics of Er^{3+} in erbium-doped silicon-rich silicon oxide", Appl. Phys. Lett. **78**, 2709 (2001).
[18] LED Manufacturer: Kingbright, LED Part-No: L-7677C2PBC-H.
[19] S. Coffa, F. Priolo, and G. Franz, "Optical activation and excitation mechanisms of Er implanted in Si", Phys. Rev. B **48**, 11782 (1993).
[20] YuanYuan Zhang et al, "Enhancement of electroluminescence from TiO_2/p^+-Si heterostructure-based devices through engineering of oxygen vacancies in TiO_2", Appl. Phys. Lett., **95,** 252102 **(**2009).
[21] Isao Nakamura, Nobuaki Negishi, *et al*, "Role of oxygen vacancy in the plasma-treated TiO_2 photocatalyst with visible light activity for NO removal", J. Molec. Catalysis A: Chem., **161**, 205 (2000).
[22] Goodfellow http://www.goodfellow.com/
[23] Akira Uedono, Kazuo Shimayama, Masahiro Kiyohara, Zhi Quan Chen, Kikuo Yamabe, "Study of oxygen vacancies in $SrTiO_3$ by positron annihilation", J. Appl. Phys., **92**, 2697 (2002).
[24] S. Dannefaer and D. Kerr, "Oxygen in Silicon: A positron annihilation investigation", J. Appl. Phys.,**60**, 1313 (2009).
[25] D. J. Keeble, B. Nielsen, A. Krishnan, K. G. Lynn, S. Madhukar, R. Ramesh, and C. F. Young, "Vacancy defects in (Pb,La)(Zr,Ti)O_3 capacitors observed by positron annihilation", Appl. Phys. Lett. **73**, 318 (1998).
[26] Varian Semiconductor Equipment Associates: http://www.vsea.com/.
[27] Samples provided by Dr A.P. Knights, McMaster University, Hamilton, Canada.
[28] P.F. Trwoga, A.J. Kenyon, C.W. Pitt, "Modeling the contribution of quantum confinement to luminescence from silicon nanoclusters", J. Appl. Phys. **83**, 3789 (1998).
[29] M. Mayer, "Ion beam analysis of rough thin films", Nucl. Instrum. Methods B **194,** 177 (2002).
[30] Eun-Cheol Lee, D. Landeer (ed), "Nitrogen-induced interface defects in Si oxynitride", Phys Rev B **77**,104 (2008).

[31] Landheer *et al*, “Positron study of plasma-enhanced chemical vapour deposited silicon nitride films”, J. Appl. Phys. **78**, 2568 (1995).
[32] Kris V. Srikrishnan, “Smart-cut process for the production of thin semiconductor material films”, United States Patent (1999).

CONCLUDING REMARKS

During the time spent on the research projects described in this report, a number of successful novel observations have been made. The most significant results have been:

(a) the observation of a small but meaningful response of spin-polarised positrons to spin-polarised electrons in iron:

(b) the monitoring of the evolution of silicon nanocrystals during the annealing of a silicon-rich silica film, and the elucidation of the role played by the nanocrystal interface in energy transfer and light emission:

(c) the observation of new phenomena in thin water ice films, particularly near-surface crystallisation at low temperatures and the evolution of pore structures.

A number of other useful studies of vacancy defect evolution in a variety of thin films and ion-implanted samples have also been performed.

Some of these results (e.g. (a) and (c)) have already been published and are listed in the Appendix following. Others (e.g. (b)) are being prepared for publication. This thesis shows the usefulness of positron beam techniques in a wide range of applications; they are versatile in that they can be adapted to fit specialised situations, e.g. by modifying the sample holder to illuminate samples, using a cold finger to grow ice samples in *situ*, or spin-polarising the beam for magnetic measurements. This also reflects the extent and type of work done during the research described in this thesis.

It is hoped that the work reported on here will provide the basis for further related studies, promote associated experiments and inspire research linked to what has been described.

APPENDIX

A. Kallis: List of publications

- A.J. Smith, R. M. Gwilliam, V. Stolojan, A.P. Knights, P. G. Coleman, A. Kallis and S.H. Yeong, "Enhancement of Phosphorus Activation in Vacancy Engineered thin Silicon-on-Insulator Substrates". J. Appl. Phys. **106**, 103514 (2009).

- Y. C Wu, A. Kallis, J. Jiang and P. G. Coleman, "Structural and Phase Changes in Amorphous Solid Water Films Revealed by Positron Beam Spectroscopy", Phys. Rev. Lett. **105**, 066103 (2010).

- P.G. Coleman and A. Kallis, "Development of a Spin-Polarised Positron Beam", J.Phys: Conf. Series (accepted for publication, 2010).

- A.P. Knights, J.D.B. Bradley, O. Hulko, D.V. Stevanovici, C.J. Edwardson, A. Kallis, P.G. Coleman, I.F. Crowe, M.P. Halsall and R.M. Gwilliam, "Probing the formation of Silicon nano-crystals (Si-ncs) using Variable Energy Positron Annihilation Spectroscopy", J.Phys: Conf. Series (accepted for publication, 2010).

- Y.C. Wu, P.H. Li, X.D. Xue, S.J. Wang, A. Kallis, P.G. Coleman and T. Zhai, "Corrosion of Pure Aluminium and Aluminium Alloy: a Comparative Study using a Slow Positron Beam", J.Phys: Conf. Series (accepted for publication, 2010).